FRONTIERS OF OPTICAL NETWORKING TECHNOLOGIES: MILLIMETER-WAVE RADIO-OVER-FIBER AND 100G TRANSPORT SYSTEM FOR NEXT-GENERATION HIGH-DATA-RATE APPLICATIONS

A Dissertation
Presented to
The Academic Faculty

by

Yu-Ting Hsueh

In Partial Fulfillment
of the Requirements for the Degree
Doctor of Philosophy in the
School of Electrical and Computer Engineering

Georgia Institute of Technology
May 2012

FRONTIERS OF OPTICAL NETWORKING TECHNOLOGIES: MILLIMETER-WAVE RADIO-OVER-FIBER AND 100G TRANSPORT SYSTEM FOR NEXT-GENERATION HIGH-DATA-RATE APPLICATIONS

Approved by:

Dr. Gee-Kung Chang, Advisor
School of Electrical and Computer Engineering
Georgia Institute of Technology

Dr. Emmanouil M. Tentzeris
School of Electrical and Computer Engineering
Georgia Institute of Technology

Dr. Stephen E. Ralph
School of Electrical and Computer Engineering
Georgia Institute of Technology

Dr. Sorin Tibuleac
School of Electrical and Computer Engineering
Georgia Institute of Technology

Dr. John R. Barry
School of Electrical and Computer Engineering
Georgia Institute of Technology

Dr. Ellen W. Zegura
School of Computer Science
Georgia Institute of Technology

Date Approved: 03 29, 2012

To my parents and my beloved husband, for all of their support and encouragement

ACKNOWLEDGEMENTS

It is a pleasure to express my sincere gratitude to the many people who made this dissertation possible.

Foremost, I am very grateful to my advisor, Professor Gee-Kung Chang, for his guidance, patience, and never ending support. The enthusiasm and perpetual energy he has for his research and life was contagious and motivational for me. I could not have imagined having a better advisor and mentor for my Ph.D study.

Another person I am also deeply indebted to is Prof. Stephen E. Ralph. I appreciate all his contributions of time, ideas, and immense knowledge to make my Ph.D. experience with another dimension. My sincere thanks also goes to Dr. Jianjun Yu for his insightful comments and inspiration of my research work. I would also like to thank Professor John R. Barry, Professor Manos M. Tentzeris, Professor Ellen W. Zegura, and Dr. Sorin Tibuleac for serving my committee and their many helpful suggestions for my dissertation.

I am certainly appreciative and thankful for all my colleagues from Optical Networking Research Group and 100G Consortium. Their advice and collaboration as well as friendship have supported my professional and personal life in the Ph.D. pursuit. Thanks to Hung-Chang Chien, Andy Stark, Zhensheng Jia, Shu-Hao Fan, Arshad Chowdhury, Chen Liu, Tom Detwiler, Patrick Caputo, Patrick Decker, Steven Searcy, Claudio Estevez, Ming-Fang Huang, and the numerous grad students who have come through the labs.

My time at Georgia Tech was enriched by the many friends. Special thanks go to Yung-Wen Lee, Szu-Yu Huang, Tsun-Yen Wu, and Chien-Chiang Chen. I am grateful for time spent with you, for our many Friday nights and memorable trips.

Lastly, I would like to thank my family for all their love and encouragement. For my parents, Chin-Yi Hsueh and Chin-Chu Chen, who raised me in a loving environment and always supported all my pursuits. For my older brother who took care of our family during my study in America. For my parents in law who have always been firmly supportive of my study. Saving the best for last, I have to thank my lovely husband, Yun Lee, whose constant support and patience were the most important driving force throughout my Ph.D. life. Thank you.

TABLE OF CONTENTS

LIST OF TABLES

LIST OF FIGURES

LIST OF SYMBOLS AND ABBREVIATIONS

AP	access point
ASE	amplified spontaneous emission
AWG	arrayed-waveguide grating
BTB/B2B	back-to-back
BER	bit error rate
BPF	band-pass filter
BS	base station
BWA	broadband wireless access
CB	carrier backscattering
CD	chromatic dispersion
CL	circulator
CO	central office
CP	cyclic prefix
CSR	carrier-suppression ratio
CW	continuous wave
DAS	distributed antenna system
DEMUX	demultiplexer
DI	delay interferometer
DL	downlink
DMD	digital micromirror device
DP	dual-polarization
DQPSK	differential quadrature phase shift keying
DS	downstream

DSCM	dispersion compensation module
DSF	dispersion shift fiber
DWDM	dense wavelength division multiplexing
EA	electrical amplifier
EDFA	Erbium doped fiber amplifier
EHF	extreme high frequency
EIRP	equivalent isotropic radiated power
EVM	error vector magnitude
E/O	electrical-to-optical
FBG	fiber Bragg grating
FCC	Federal Communications Commission
FWM	four-wave mixing
FM	frequency multiplier
HDTV	high-definition television
HSR	harmonics-suppression ratio
ICI	inter-channel interference
IL	interleaver
IM	intensity modulation/ Intensity modulator
ISI	intersymbol interference
ITU-T	International Telecommunication Union -Telecommunication Standardization Sector
LAN	local area network
LE	local exchange
LMS	least mean square
LNA	low-noise amplifier
LO	local oscillator

LPF	Low-pass filter
LTE	Long Term Evolution
MAC	medium access control
MI	modulation index
MIE-PM	modulation index enhanced-phase modulator
MmW	millimeter wave
MS	mobile subscriber
MUX	multiplexer
MW	microwave
MZM	Mach-Zehnder modulator
Mb/s	megabits per second
NLAN	nonlinear amplitude noise
NLPN	nonlinear phase noise
NRZ	non-return-to-zero
OCS	optical carrier-suppression
ODSB	optical double-sideband
OF	optical filter
OFDM	orthogonal frequency-division multiplexing
OOK	on-off keying
OSNR	optical signal-to-noise ratio
OSXR	optical signal-to-crosstalk ratio
OTN	optical transport network
O/E	optical to electrical
PA	power amplifier
PAL	phase adapation layer

PBS	polarization beam splitter
PC	polarization controller
PD	photodetector
PDM	polarization-division multiplexing
PG	parametric gain
PHY	physical layer
PMD	polarization-mode dispersion
PM	phase modulation/ Phase modulator
Pol	polarization
Pol-Mux	polarization-multiplexing
PRBS	pseudorandom bit sequence
Pre-comp	pre-compensation
PON	passive optical network
RAU	remote access unit
RB	Rayleigh backscattering
RBS	random bit sequence
RDPS	residual dispersion per span
RF	radio frequency
RN	remote node
ROADM	reconfigurable optical add/drop multiplexer
ROCS	remote optical-carrier suppression
RoF	radio-over-fiber
RZ	return-to-zero
SB	signal backscattering
SBS	stimulated Brillouin scattering

SCM	subcarrier multiplexing
SPM	single-phase modulation
SRS	simulated Raman scattering
OSSB+C	optical single-sideband-plus-carrier
O/E	optical-to-electrical
SSMF	standard single mode fiber
TDM	time-division multiplexing
TFBG	tunable fiber Bragg grating
Tx	transmitter
UL	uplink
US	upstream
UWB	Ultra-wideband
VOA	variable optical attenuator
VSB	vestigial sideband
WDM	wavelength-division multiplexing
WAN	wide area network
WiGig	Wireless Gigabit Alliance
WLAN	wireless local area network
WMAN	wireless metropolitan area networks
WPAN	wireless personal area network
WSS	wavelength selective switch
XPM	cross-phase modulation
X-NLPN	cross-nonlinear phase noise
XPolM	cross-polarization modulation
100GbE	100 gigabit Ethernet

SUMMARY

The ongoing growth of Internet traffic being driven by data storage and video file-sharing traffic have placed huge bandwidth and capacity requirements not only for the long-haul networks but also for the last mile access networks. In response to the remarkable development, the line rate in the metro core networks based on fiber-optic technology has to be upgraded from 10 Gb/s to 100 Gb/s, while a millimeter-wave radio-over-fiber technology has been considered the most practical and efficient solution for future super-broadband wireless access networks. The Ph.D. work then focuses on investigating both wired and wireless communications over optical systems for the provision of high-data-rate applications in next-generation telecommunications network.

The radio-over-fiber system at millimeter wave, especially 60-GHz band with 7-GHz unlicensed bandwidth, has unique potential to deliver multi-gigabit services to remote base stations. Therefore, one major objective of this work is to develop a simple and cost-effective millimeter-wave optical-wireless system through the all-round research on the technical challenges of optical millimeter-wave generation, full-duplex transmission, transmission impairments compensation, and multi-band generation. The general methods of optical millimeter-wave generation were reviewed concerning the system flexibility, structure complexity, and power efficiency. Then two novel optical frequency-doubled millimeter-wave generation schemes based on external phase modulation were proposed and experimentally demonstrated their simplicity, reliability, and cost-efficiency compared with the existing schemes. For successful full-duplex transmission, two methods for eliminating the requirements of light sources and

wavelength management at the base station were shown here: downlink wavelength reuse and remote-carrier delivery for uplink. Moreover, the penalties due to backscattering signals for bi-directional transmission over a single fiber can be mitigated by different wavelength assignments for downlink and uplink. The transmission distance limited by fiber chromatic dispersion is also a key challenge for cost-efficient millimeter-wave radio-over-fiber implementations with less central offices. The numerical analysis and experimental demonstration suggested that a radio-over-fiber system with the optical single-sideband-plus-carrier format or remote optical-carrier-suppression is more resistant to this transmission impairment and then achieve longer transmission distance. Additionally, several radio-over-fiber systems were designed to simultaneously deliver multi-band wireless services on a single optical infrastructure, enabling converged system control and quality maintenance in central office. Some proposed schemes efficiently integrated the new 60-GHz band with commercial wireless services at low RF regions, allowing a system not only providing multi-gigabit data and video distributions but also has backward compatibility to legacy wireless services. The lightwave centralization, frequency doubling/tripling, long transmission distance, high-level modulation format were also realized in these novel multi-band RoF architectures.

For the long-haul core network, moving from 10G to 100G line speeds comes with technical challenges. The Ph.D work explored the issues related to successful implementations of transmitter, transmission link, and receiver of a serial 112-Gb/s polarization-division multiplexing-quadrature phase shift keying (PDM-QPSK) optical transport. The experimental results based on our constructed 112-Gb/s testbed indicated that careful dispersion management can effectively increase QPSK channel tolerance to

nonlinear transmission impairments. Moreover, 100G dense wavelength-division multiplexing networks with reconfigurable optical add-drop multiplexers (ROADMs) enable dynamically reconfigurable networks and are therefore part of the solution needed to meet increasing bandwidth and routing flexibility requirements for future metro core networks. Thus, the special emphasis on the two impairments in a 100G ROADM-enabled network, passband and in-band crosstalk effects, was studied in this thesis. The experimental results showed the penalties contributed by passband narrowing and frequency detuning are pulse format dependent; return-to-zero pulse shape offers better tolerance to filtering and fiber nonlinearity compared to non-return-to-zero. A weighting method was also demonstrated to quantify the penalty of in-band crosstalk that accounts for the varying spectral content. Lastly, a nonlinearity-enhanced crosstalk penalty were experimentally and numerically demonstrated that results from the nonlinear interaction between crosstalk and signals over long-distance transmission. It is another critical transmission limitation except for the nonlinear interactions between signal and ASE noise. Therefore, the research results related to the dispersion management, fiber nonlinearity penalties, and ROADM-induced impairments can be effectively applied to the deployment and performance estimation of future 100G optical transport networks.

CHAPTER 1

INTRODUCTION

1.1 Background

Envision a global network where people need to access the Internet and exchange information anytime and anywhere. The number of Internet users around the world has grown 444.8% from 2000 to 2010, and the worldwide Internet penetration rate has reached 28.7% in 2010 [1]. Amid the explosive demand for bandwidth over the last decade, the optical fiber has played a key role in providing high-speed and ubiquitous Internet access. In 1966, Charles K. Kao proposed to use glass fibers with large bandwidth and low loss to implement optical communication. This great scientific achievement not only earned Kao the 2009 Nobel Prize in Physics, but also lays the foundation of today's long-haul and high-capacity data transmission. However, the demand for transmission capacity, mostly driven by an increasing popularity of photo and video sharing on social networks, expanding mobile device applications, and the pervasiveness of high-definition television (HDTV), has increased beyond prediction. According to Cisco's forecast [2], as shown in Figure 1.1, the global IP traffic in 2014 will reach 767 exabytes per year or 64 exabytes per month. Moreover, comparing the consumer Internet traffic in 2009 and 2014 shown in Figure 1.2 [2], we can see that the sum of all forms of video (TV, video on demand, Internet, and peer-to-peer) will exceed 91% by 2014. To handle this exponential growth of network traffic, the line rate for local area network (LAN) and wide area network (WAN) are evolving from 10 to 100 gigabits per second (Gb/s). The standardizations of 100G Ethernet and optical transport network (OTN) have finished and reported in IEEE 802.3ba and International Telecommunication Union-Telecommunication Standardization Sector (ITU-T) G.709, respectively [3].

Furthermore, the deployments of 100G networks are expected to take place in a couple of years with commercial 100G products, such as chip sets, client interfaces, router ports, and optical transport gear. Single-wavelength 400G and 1T are taking shape as the next steps for the core network.

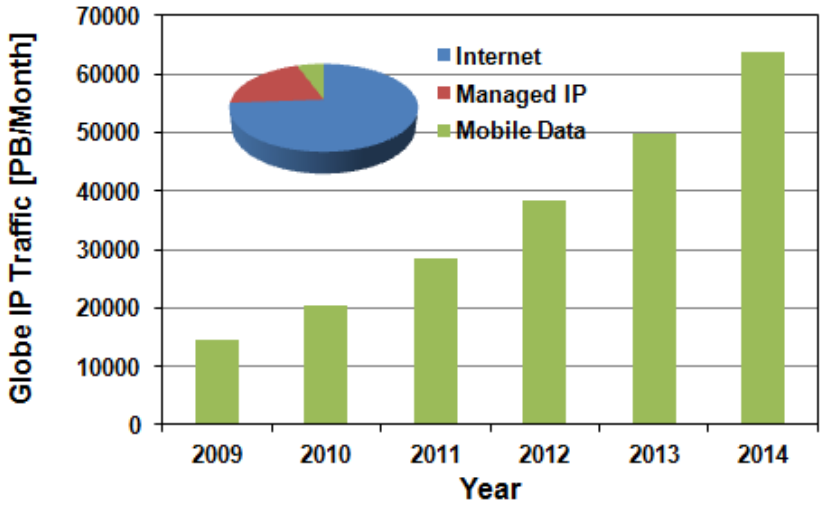

Figure 1.1. Global IP traffic growth from 2009 to 2014.

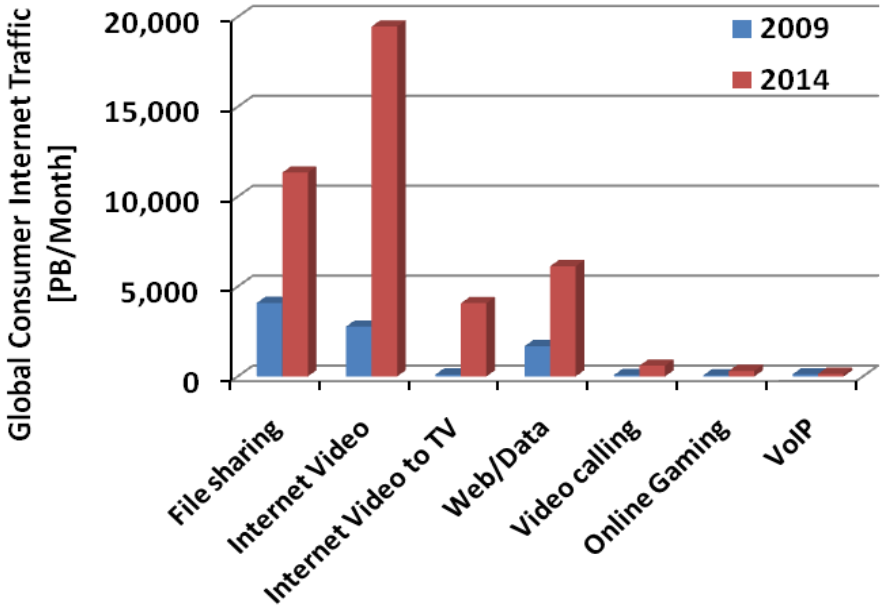

Figure 1.2. Global consumer Internet traffic in 2009 and 2014.

In conjunction with the rapid development of metro core network, the transmission speed for last-meter access network, especially wireless services, is also needed to be scaled up to multi-gigabit rate as shown in Figure 1.3. Owing to rapid increasing mobile users, the data traffic levels in mobile networks are expected to double every year up until 2015 [4] as Figure 1.4 shows. The most effective way to improve the wireless throughput per user is to reduce the cell size. While the throughput is improved with the deployments with small cell size, the utilized RF bandwidth is the limitation factor for the capacity of wireless networks.

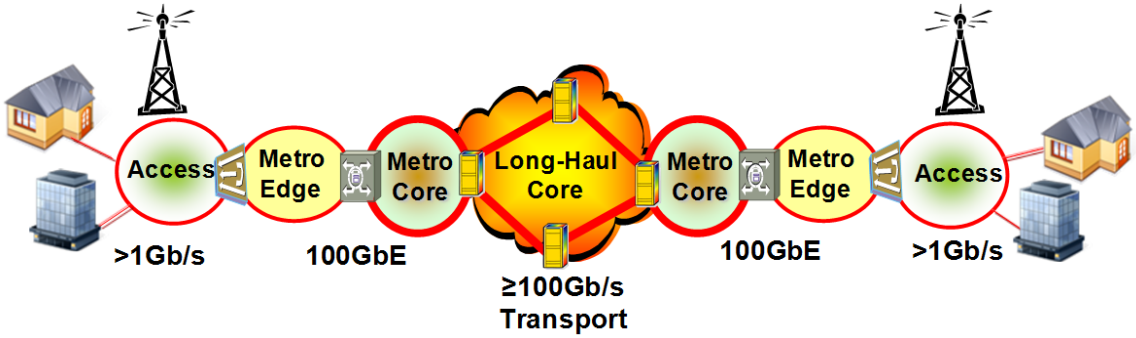

Figure 1.3. Future network with converged transport and Ethernet (100GbE: 100 gigabit Ethernet).

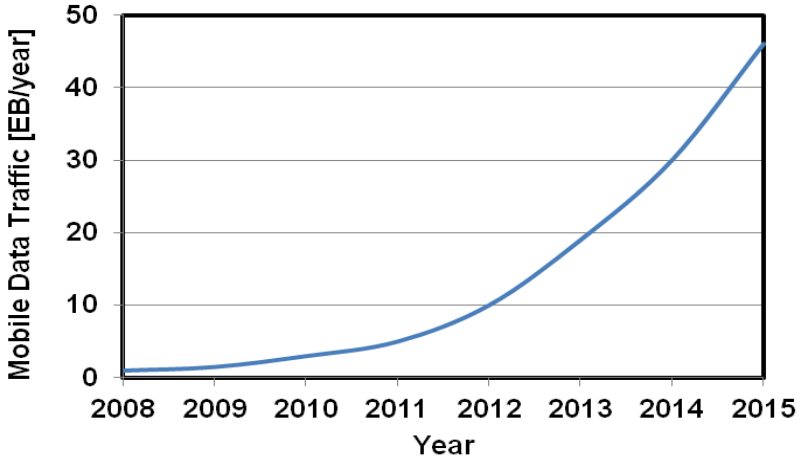

Figure 1.4. Data traffic in mobile access networks from 2009 to 2015.

Recently, broadband wireless access (BWA) technologies, such as Wi-Fi (IEEE 802.11) for wireless LAN (WLAN), Bluetooth for wireless personal area network (WPAN), and WiMAX (IEEE 802.16) for wireless metropolitan area networks (WMAN), have become popular for different application scenarios because of their convenience, flexibility, and mobility [5]. Unfortunately, the bandwidth available for current BWA technologies are only few hundred megaherz. For example, there are only 70 MHz in the 2.4GHz and 500 MHz in the 5 GHz for Wi-Fi. In addition, current wireless communications with lower microwave carrier frequencies have severe frequency congestion because a multitude of consumer products uses those frequencies. Therefore, the most promising way to increase wireless transmission capacity is to migrate to higher carrier frequencies, which offer much more available spectrum.

Furthermore, there is a multitude of multimedia applications calling for wireless transmission, and their required data rates are larger than hundreds of megabits per second. For instance, the uncompressed HDTV 1080i requires a transfer rate of 1.485 Gb/s while the HDTV 1080p requires 2.97 Gb/s. However, current BWA technologies can only handle transmission rates on the order of tens of megabits per second (Mb/s). For example, Wi-Fi, which consists of several standards including IEEE 802.11n, 802.11b, 802.11g, and 802.11a, offers a maximum data rate of 300 Mb/s. For WiMAX, the maximum downlink (DL) data rate specified in IEEE 802.16e is just 128 Mb/s. Obviously, the commercial wireless services cannot accommodate these very-high-throughput applications, and a new wireless technology should be developed to support future demands.

Extremely high frequency (EHF), defined as a range of electromagnetic waves with frequencies between 30 GHz and 300 GHz, has a wavelength of one to ten millimeter; therefore, it is also called millimeter wave (mmW). Compared to lower bands with spectral congestion, the mmW can offer a massive amount of spectral space to support high-speed applications such as wireless LAN bridge and HD video distribution

[6]. In particular, the 60-GHz band has gained much attention and been viewed as the most promising carrier in next-generation wireless networks because of its widest unlicensed bandwidth among all the wireless channels.

This introductory chapter is organized as follows. Section 1.2 gives an overview of the characteristics and standards of 60-GHz mmW applications. A new technology, which integrates optical systems and wireless technologies, is introduced in Section 1.3. Then, Section 1.4 presents the enabling technologies for a 100G optical transport system. Finally, the research objectives and the organization of dissertation are showed in Section 1.5.

1.2 Millimeter-Wave Wireless Communication

In the United States, the mmW technology operating above 40 GHz had been limited to military and scientific applications before 1994. To encourage the development of commercial products and services operating above 40 GHz, the United States Federal Communications Commission (FCC) in October of 1994 issued a Notice of Proposed Rulemaking (NPRM) that proposes to open a portion of the mmW frequency bands above 40 GHz for commercial uses. Nowadays, many countries around the world have an approximately 7-GHz unlicensed bandwidth in the 60-GHz band as Figure 1.5 shows. As a result, the 60-GHz mmW systems have not only about 7-GHz unlicensed bandwidth available for use, but also negligible interferences with commercial wireless services with low-frequency carriers. Because of these features, the 60-GHz mmW systems have been considered as an ideal candidate for the implementation of very-high-throughput WLAN or WPAN.

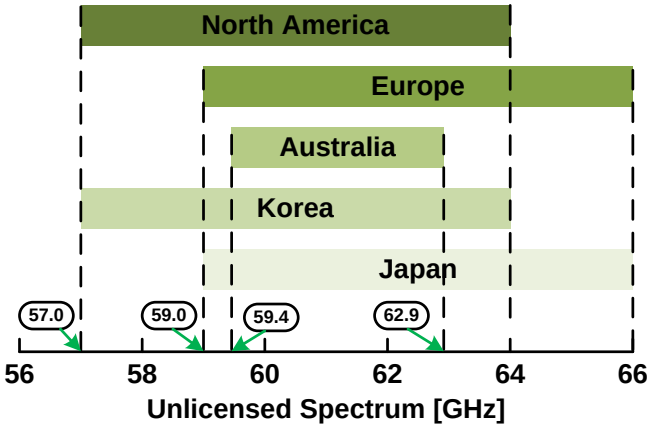

Figure 1.5. Worldwide unlicensed spectrum in the 60-GHz band.

Before designing a 60-GHz system, we should understand all the channel characteristics that could affect the performance of the system. The first characteristic is the path loss, which includes the free-space path loss, the atmospheric absorption, and so on. The free-space loss characteristic of a RF signal can be explained by Friis transmission equation [7]:

$$P_r = P_t G_t G_r \left(\frac{\lambda}{4\pi R}\right)^2, \tag{1.1}$$

where P_r is the power received by the receiving antenna, P_t is the power input to the transmitting antenna, G_t and G_r are the antenna gain of the transmitting and receiving antennas, respectively, λ is the wavelength, and R is the distance. This equation proves that, for the signal with a high frequency like mmW, the wireless transmission of which over a short distance will suffer from a very large propagation loss. Figure 1.6 shows the free-space loss for different carrier frequencies. For example, the 10 m free-space transmission would induce about 84 dB loss for a 60-GHz RF signal.

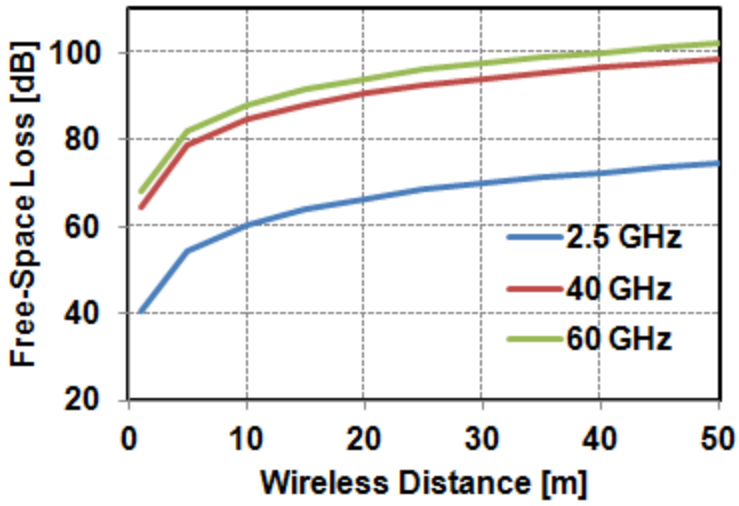

Figure 1.6 Free-space loss versus distance for 2.5-, 40-, and 60-GHz signals.

In addition, for the 60-GHz signal, the atmospheric gaseous attenuation is also quite large as shown in Figure 1.7, which is mainly due to oxygen absorption [8]. Since the propagation of 60-GHz signals over air is strongly attenuated, the 60-GHz system is more suitable for the short-range broadband communications than for the long-range (i.e. over ten meters) wireless communications. Furthermore, because of the high material attenuation at the 60-GHz band compared to 2.5-GHz band (Table 1.1; [9]), the operating range for the 60-GHz services is confined to a single room. In other words, since the 60-GHz signal attenuates considerably in the walls and floors, it can offer high security as well as suffer low interference from the adjacent networks. Lastly, because the 60-GHz signal has a very short wavelength, we can install an antenna array in a small area, which not only compensates for the path loss but also increases the link budget.

Table 1.1. Material attenuation at 60 GHz and 2.5 GHz

Material	**Loss at 60 GHz (dB/cm)**	**Loss at 2.5 GHz (dB/cm)**
Drywall	2.4	2.1
Whiteboard	5.0	0.3
Glass	11.3	20.0
Mesh Glass	31.9	24.1

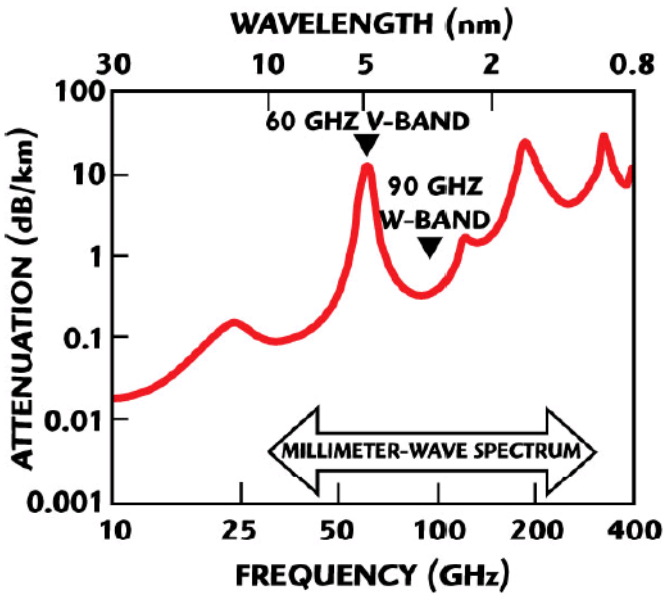

Figure 1.7. Average atmospheric absorption versus frequency.

Table 1.2 compares three typical implementations using different unlicensed bandwidth, including the 60-GHz, Ultra-wideband (UWB), and IEEE 802.11n systems, based on various criteria near the FCC regulatory limit [10]. First, the 60-GHz system owns one of the largest unlicensed, continuous bandwidth for gigabit wireless applications (Table 1.2; column 1). Second, the 60-GHz system has the largest antenna gain (Table 1.2; column 3) that can be used to boost the output power of a power amplifier (PA) (Table 1.2; column 2), which currently is limited to 10 dBm due to the implementation challenge at this frequency. Finally, the FCC regulatory limit allows the 60-GHz signals to transmit with much higher power—or specifically the equivalent isotropic radiated power (EIRP) —than the UWB and 802.11n systems to overcome its large path loss (Table 1.2; column 4).

Table 1.2. Comparison between typical implementations of 60 GHz, UWB and 802.11n.

	Frequency [GHz]	PA Output Power [dB]	Antenna Gain [dBi]	EIRP Output [dBm]
60 GHz	57.0-64.0	10.0	25.0	35.0
UWB	3.1-10.6	-11.5	1.5	-10.0
IEEE 802.11n	2.4/5.0	22.0	3.0	25.0

Because of the many advantages mentioned earlier, the industry and standards organizations have been trying to standardize the WPAN and WLAN technologies at 60-GHz band with great efforts. For the WPAN technology, standards such as IEEE 802.15.3c [11], ECMA 387 [12], and WirelessHD [13] have been proposed in hopes of promoting the global use of multi-gigabit 60-GHz wireless technology such as HD multimedia and high speed kiosk data transfers. Among all these standards, the WirelessHD and IEEE 802.15.3c have already been published, and one can even find WirelessHD set-top boxes at retail stores. The ECMA 387, which was renamed the ISO/IEC 13156 by the end of 2009, specifies the high-rate 60-GHz physical layer (PHY), the distributed medium access control (MAC) sublayer, and the HDMI protocol adaptation layer (PAL) for 60-GHz wireless networks.

Meanwhile, the industry and standards organizations also aim to standardize the next generation WLAN at 60 GHz through the establishment of the IEEE 802.11ad [14] and Wireless Gigabit Alliance (WiGig) standards [15]. Specifically, the IEEE 802.11ad intends to integrate past 802.11 standards by facilitating the fast switch between 2.4-, 5- and 60-GHz bands. It is targeting a final approval by December 2012. The WiGig, on the other hand, is broadly supported by industries and its version 1.1 specifications have already published in July 2010.

1.3 Broadband Optical-Wireless Convergence

In order to accomplish 60-GHz wireless communications, a technology called radio-over-fiber (RoF) has recently proposed [16-24]. The key idea of this technology is

the integration of optical transmission systems and wireless access networks. For a mmW RoF system, the mmW signals are carried by optical carriers and then distributed to user terminals through fibers and antennas. Compared with the electrical mmW generation method, optical up-conversion methods offer definitive advantages. First of all, optical fiber provides immunity to electromagnetic interference. Secondly, it can be seamlessly applied to the deployed optical transport networks. Thirdly, some optical mmW generation methods are capable of generating multiples of a reference local oscillator (LO), providing relaxing the bandwidth requirement of electronic devices and saving costs. Therefore, the converged RoF technology with high transmission capacity, large coverage and good cost efficiency has been considered as the most promising solution for future 60-GHz wireless access networks.

Figure 1.8 shows the basic RoF structure, which is composed of a central office (CO), fiber spans, base stations (BSs), and antennas. The up-converted optical DL signals are transmitted from the CO to BSs through fiber spans. The BS is then an optical to electrical (O/E) converter which sends the electrical RF signals to end users; the BS is also called remote access unit (RAU). The CO is also responsible for the optical-to-electrical (O/E) conversion and down-conversion of uplinks (ULs). The biggest advantage of the RoF system is to simplify the architecture of BS by realizing most complicated works such as modulation, coding, and up-conversion in the CO. Especially for 60-GHz applications with numerous BSs, the implementation of RoF technology can save much cost from simple and compact BSs. Furthermore, some carefully designed RoF systems can simultaneously offer wired and multi-band wireless services based on their ultra-wide bandwidth and protocol transparent characteristics. The transmission capacity can also be increased by integrating with wavelength-division multiplexing (WDM) technology. The WDM passive optical network (PON) that can provide large guaranteed bandwidth through the point-to-point dedicated connectivity is foreseen to

replace current time-division multiplexing-PON (TDM-PON) as the next-generation access technology.

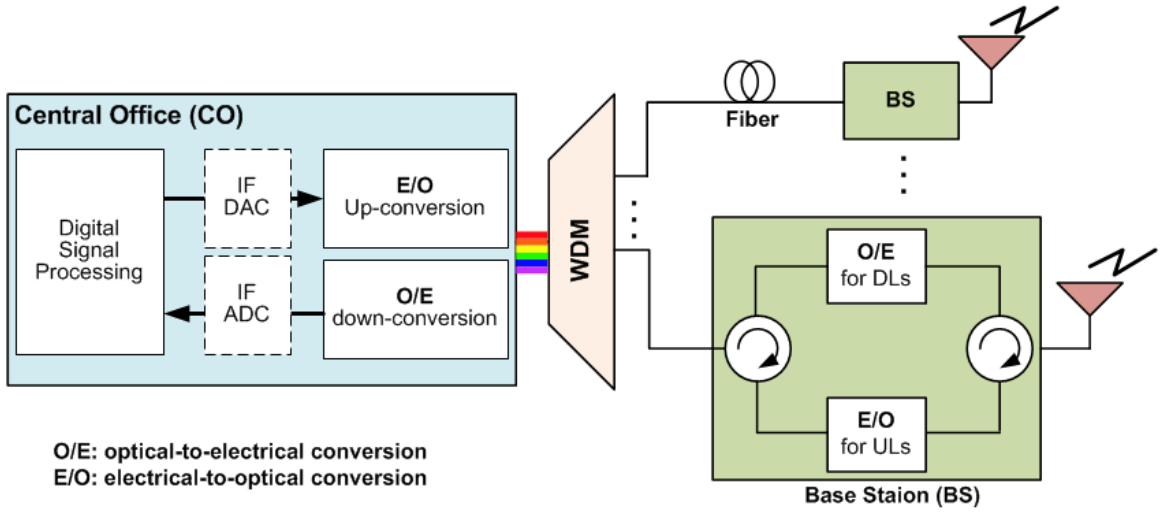

Figure 1.8. General structure of the RoF system.

1.4 100G Optical Transport Network

As mentioned in Section 1.1, the data rate of optical networks has gradually increased from 10 Gb/s to 100 Gb/s to support near-term needs for high-capacity data storage, voice, and video applications. Depending on the targeted applications, the 100G standardization includes parallel transport such as 10 × 10 Gb/s and 4 × 25 Gb/s and serial 100-Gb/s transport. The parallel transport is realized by splitting 100 Gb/s among multiple parallel lanes or among multiple parallel wavelengths [3], and it is used for short-range applications like data centers, interconnect space, and LAN Ethernet Transport. For example, 100-GBASE-LR4 and 100-GBASE-ER4 designed for 100GbE have 4 different wavelengths of 25G on the fiber and 10 electrical signals of 10G on the host [25]. The serial 100-Gb/s transport, literally, transmits data in a serial fashion (i.e., on a single optical wavelength and through a single fiber) and is expected to offer services in wide-area networks. Moreover, the total transmission capacity of the serial

100-Gb/s transport can be further increased by integrating with WDM technique to carry multiple 100-Gb/s data streams.

To achieve a long-haul transmission with 100G and beyond line rate, several advanced enabling technologies have to be employed as shown in Figure 1.9. At the transmitter, the multilevel modulation format [26-28], the multi-carrier modulation [29, 30], and the polarization multiplexing [31] can be used to decrease the baud rate for the provision of high spectral efficiency. In the transmission line, the dispersion management has been demonstrated as a necessary technique to mitigate nonlinear impairments especially for the systems with high bit rates [32, 33]. Also, new fibers with low loss and/or large effective area [34, 35] and advanced amplification techniques such as erbium doped fiber amplifier (EDFA)/Raman hybrid amplifiers [28-31, 35] can be used to improve the optical signal-to-noise ratio (OSNR) and thus increase the transmission distance. Moreover, for dense WDM (DWDM) 100G and beyond networks, the wavelength management and networking aspects need to be addressed. For example, the loss and passband effects from add/drop nodes would cause transmission penalties and the limit of transmission distance; a detailed analysis regarding this issue is required for successful network deployments [36].

For the receiver, direct detection can provide the required performance for metro networks at the lower cost and complexity compared to coherent detection. However, direct detection is restricted within specific modulation formats. On the other hands, coherent detection is sensitive to the phase as well as amplitude, so can be applied to demodulate different modulation formats. Furthermore, it moves the complexity of phase and polarization tracking into the digital domain. Some linear and nonlinear optical impairments such as chromatic dispersion (CD), polarization-mode dispersion (PMD), cross-phase modulation (XPM), single-phase modulation (SPM), and cross-polarization modulation (XPolM) can also be electrically compensated by using the coherent detection [26-31, 34, 35].

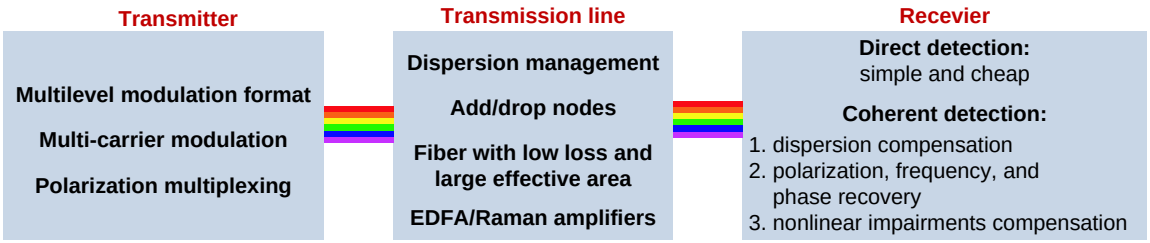

Figure 1.9. Enabling technologies for long-haul networks with high transmission capacity.

1.5 Objectives and Organization of Thesis

The objective of this dissertation is to develop the enabling technologies and identify the issues of future high-speed metro and access networks over optical fibers. The comprehensive study on both long-haul optical transport and last mile, last meter optical-wireless communications with high-data-rate applications is the novelty of this work. For the next-generation wireless access network, RoF technology at mmW band has been viewed as the most promising way to deliver multi-gigabit services to remote access units. The research focuses on the development of a simple, cost-effective and converged wireless access network through the investigations of mmW generation, multi-band generation, transmission impairments compensation, and full-duplex transmission.

As bandwidth consumption continues to rise, the serial data rate in metro network should be increased from current 10-Gb/s transport, rather than the number of parallel color channels based on WDM technology. The line rate of 100G over optical networks is designed to transport 100GbE, the latest speed boost for Ethernet. Then the other major focus of this Ph.D work is to explore the issues related to successful implementations of transmitter, transmission link, and receiver of a single-wavelength 112-Gb/s optical transport. The special emphasis on the impairments analysis for a 100G ROADM-enabled network is also investigated.

The outline of this dissertation is as follows. Chapter 2 discusses the design challenges of a practical mmW RoF system. The characterization of optical mmW

generation with a single Mach-Zehnder modulator under different configuration is also shown in this chapter. Several schemes for efficient optical mmW generation and long-reach fiber transmission have been proposed and experimentally demonstrated. Chapter 3 focuses on the multi-band generation in one optical platform based on RoF technology. Various schemes are presented for simultaneously delivering mmW, microwave, baseband, and commercial low-RF wireless services. A novel multi-band generation method via 60-GHz sub-bands distribution and band mapping concept is proposed and is one of the main topics of this thesis. Chapter 4 gives an overview of a 112-Gb/s optical system, taking special interest in modulation format, transmission link, and detection method. Moreover, the dispersion management and transmission impairments induced by add-drop nodes in WDM networks are experimentally examined. Finally, Chapter 5 provides a summary of the main results achieved throughout this work and presents the potential research topics in the future.

CHAPTER 2

MILLIMETER-WAVE RADIO-OVER-FIBER TECHNOLOGY

This chapter is organized as follows. Section 2.1 gives an overview of a mmW RoF system in terms of functions and design challenges for each component. In section 2.2, the introduction and comparison of common methods for optical millimeter-wave generation are presented. The proposed optical mmW generation methods based on phase modulation are also shown in this section. Then, the fiber transmission impairments due to chromatic dispersion and backscattering interference are analyzed in section 2.3; the architectures designed to overcome these impairments are experimentally and numerically demonstrated here.

2.1 Introduction

Figure 2.1 shows a typical schematic structure of a mmW RoF system. For the downlink transmission, the CO, a RF/optical interface, is responsible for signal generation, processing and multiplexing. A number of wireless-optical signals are delivered to the BSs through fiber networks and remote nodes (RNs). The broadcast of mmW signals can be accomplished by in-building or outdoor antennas as Figure 2.1 shows. In contract to baseband-over-fiber and intermediate frequency (IF)-over-fiber methods, which having transceiver RF front-ends in the BSs, the only functions that need to be carried out at the BSs for mmW RoF systems are the O/E conversion and the broadcast of RF signals. Overall, the mmW RoF technology provides a centralized architecture in which the costly signal-processing equipments, the installation and maintenance efforts are consolidated at the CO.

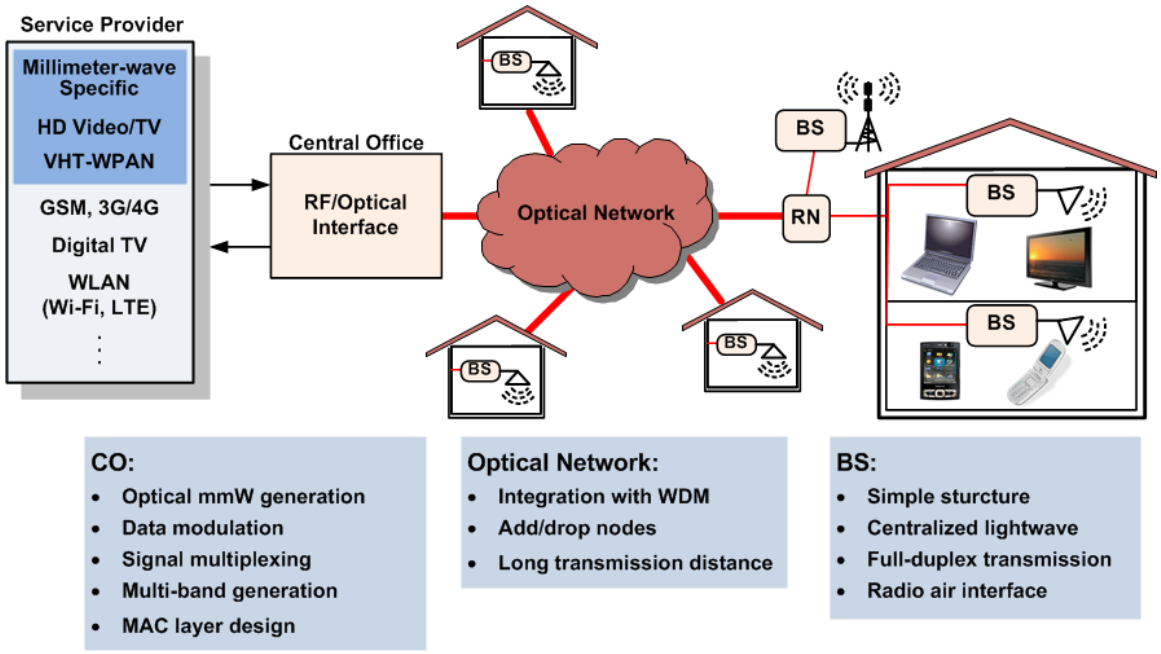

Figure 2.1. Schematic structure and technical challenges of the mmW RoF system.

There are several challenges and design issues for each component of the mmW RoF system as shown in Figure 2.1, which are related to many enabling technologies to achieve successful RoF deployments in the real networks. The main function of CO is to optically up-convert the digital baseband or analog IF signal into the mmW band. A cost-effective and simple method of optical mmW signal generation is critical to the successful deployment of RoF systems. The mmW generation methods will be investigated thoroughly in the next section. In addition, based on the ultra-wide bandwidth and protocol transparent characteristics of RoF links, a novel signal integration design called multi-band generation, which aims at integrating mmW, microwave (MW; 3 - 30 GHz), and wireless signals at low RF regions (Wi-Fi, WiMAX, etc.) on the same optical platform, has been proposed recently. Although the implementation of this design is challenging at the CO, the relatively easy system control and quality maintenance makes it as a popular choice for providing various kinds of wireless services in the future. Several schemes realizing the multi-band generation have been demonstrated in [37-42]. Additionally, except for the conventional intensity

modulation (ex. on-off-keying (OOK)), different modulation formats such as higher-level quadrature amplitude modulation (QAM) and orthogonal frequency-division multiplexing (OFDM) can be employed to increase transmission capacity or overcome the multipath spreading interference [43-46].

The long fiber transmission distance and flexible wavelength assignment are the goals for the optical network. The deployment of reconfigurable optical add/drop multiplexers in a WDM-PON RoF system can achieve good network transparency [47, 48]. However, the transmission distance for optical mmW signals is limited by the fiber chromatic dispersion, which causes the fading effect and time shifting of the codes [49-53]. The detailed analysis for these transmission impairments and the methods proposed to overcome the dispersion effect are described in Section 2.3.

Additionally, the structure and cost of BS are key points to achieve a cost-effective mmW RoF system. This is because the mmW RoF system has short distance of radio propagation and then needs a large number of BSs within a small area. For example, one of the design issues for a full-duplex mmW RoF system is how to centralize all lightwave sources in the CO. It means that there is no need for uplink lasers in BS, which can decrease the cost of BS. There are two lightwave centralization methods: DL wavelength reuse and remote-carrier delivery for UL as Figure 2.2 shows. For the DL wavelength reuse methods, which can be achieved by (reflective) semiconductor optical amplifiers ((R)SOAs) [54, 55] or specific modulation formats for the DL [56], the UL wavelength is the same with DL; while the UL wavelength is different from the DL for remote-carrier delivery [57].

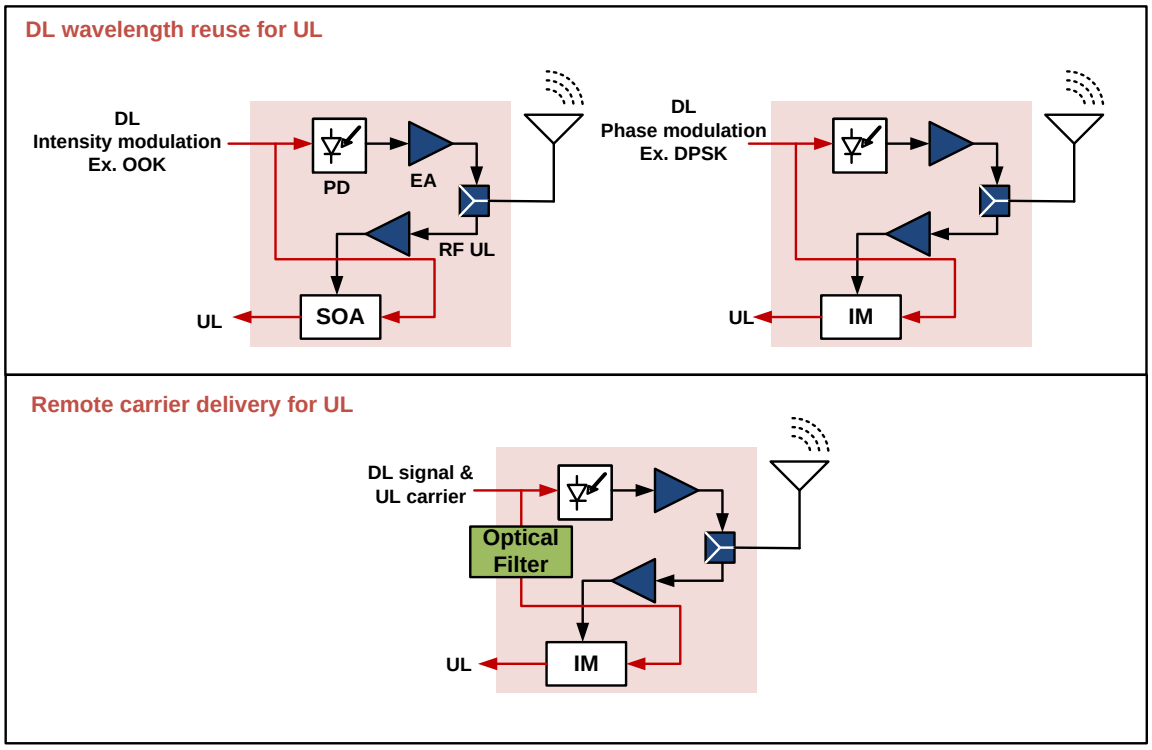

Figure 2.2. BS designs for lightwave centralization: DL wavelength reuse and remote-carrier delivery for UL (PD: photodetector, EA: electrical amplifier; IM: intensity modulator).

2.2 Optical Millimeter-Wave Generation Methods

2.2.1 Methods with One and Dual Lasers

Most technologies of optical mmW generation can be classified into two categories: one laser or two lasers needed as Table 2.1 shows. The generation schemes with one laser are based on direction modulation, external modulation, and dual-mode DFB [53, 58], while the schemes with two lasers are based on nonlinear effects in the nonlinear media [19, 59], heterodyne mixing of independent lasers [60], and injection locking [61, 62].

Table 2.1. Optical mmW generation methods.

One laser	Two lasers
· Direct modulation	· Nonlinear effects
· External modulation	· Heterodyne mixing of independent lasers
· Dual-mode DFB laser	· Injection locking

The direct modulation by laser is a simple way to generate mmW signals, but it is limited by the modulation bandwidth of laser source, which is around 30 GHz. The realization of mmW generation by nonlinear effects such as FWM and XPM [19] in the nonlinear media has the advantages of high conversion efficiency and large conversion bandwidth. However, it requires high input power and has uneven response for the large bandwidth. Furthermore, the heterodyne mixing of two independent lasers has been viewed as the most simple method to optically generate mmW signal. Unfortunately, the large jitter and phase noise induced by the wide signal linewidth and the need of accurate polarization control are the disadvantages for the heterodyne mixing scheme [60]. Although the dual-mode DFB laser can generate two phase-locked modes with specific frequency difference and is without any requirement for electronic feedback systems [58], this kind of laser is not a commercial product and is absence of system flexibility. For the injection locking method, the large injection signal power and only few GHz locking range make it impractical for system implementation [61, 62].

The optical mmW generation using external optical modulation, which taking advantage of the intrinsic nonlinear response of modulators to generate high-order sidebands and obtain the corresponding mmW carrier through the optical heterodyning. The external modulation can be intensity or phase modulation. Among all optical mmW generation methods, this one is most flexible and easy to integrate with WDM system. The main drawback of this method is the insertion loss of external modulators, so it usually require additional optical amplifiers to compensate the power loss. In this thesis,

the proposed RoF systems are all based on external modulation. Table 2.2 summarizes the advantages and disadvantages of the mentioned up-conversion methods.

Table 2.2. Advantages and disadvantages of optical mmW generation methods.

Methods	**Advantage**	**Disadvantage**
Direct modulation	· Simple implementation	· Limited by modulation bandwidth · High RF LO[1] needed
External modulation	· Good system flexibility · Harmonic generation · Easy integration with WDM	· Insertion loss
Dual-mode laser	· Simple and compact source · No RF LO needed	· Not a commercial product · Low system flexibility
Nonlinear effects	· High conversion efficiency · Large conversion bandwidth	· High input power needed · Uneven response for the large bandwidth
Heterodyne mixing	· The simplest one · No RF LO needed	· Large jitter · Large phase noise · Accurate polarization control needed
Injection locking	· No RF LO needed	· Large injection signal power · Only few GHz locking range · Temperature sensitivity

[1] LO: local oscillator

2.2.2 External Intensity Modulation: ODSB, OSSB+C, and OCS

The external intensity modulation realized by dual-arm Mach-Zehnder modulators (MZM) can have three different formats: optical double-sideband (ODSB), optical single-sideband-plus-carrier (OSSB+C), and optical carrier-suppression (OCS) [49]. As Figure 2.3 shows, the three formats can be achieved by one or dual modulators. For the method with dual modulators, the first intensity modulator (IM) is responsible for data modulation, while the second modulator (dual-arm MZM) is for RF modulation; it is a method with all-optical mmW up-conversion. For the case with a single dual-arm MZM, the data has to be electrically up-converted to the RF band and then modulates the

optical carrier. Reference [49] had investigated the three formats achieved by dual modulators, so the following theoretical analysis is for one modulator case.

The continuous-wave (CW) lightwave from a distributed feed-back laser diode (DFB-LD) is represented by $E_0 e^{j\omega_c t}$, where E_0 and ω_c are the amplitude and angular frequency of the CW. It is then modulated by a RF signal, which is a baseband data A(t) mixed with a RF LO $V_1 cos\omega_m t$. For ODSB scheme, only one arm of MZM is driven by the RF signal, and the bias point of MZM (V_b) is at linear region. The electrical output of MZM is

$$
\begin{aligned}
& E_0 e^{j\omega_c t} \cdot \frac{1}{2}\left[\exp\left(j\frac{\pi}{V_\pi}V_1 A(t) cos\omega_m t\right) + \exp\left(j\frac{\pi}{V_\pi}V_b\right)\right] \\
&= E_0 e^{j\omega_c t} \cdot \frac{1}{2}\left[\exp\left(j\frac{\pi}{V_\pi}V_1 A(t) cos\omega_m t\right) + \exp\left(j\frac{\pi}{V_\pi}\cdot\frac{V_\pi}{2}\right)\right] \\
&= \frac{1}{2}E_0 e^{j\omega_c t}\left[\sum_{k=-\infty}^{\infty} j^k J_k(m_{h1}) e^{j\omega_m t} + j\right] \\
&\approx \frac{1}{2}E_0 e^{j\omega_c t}[(J_0(m_{h1}) + j) + jJ_1(m_{h1})e^{j\omega_m t} + jJ_1(m_{h1})e^{-j\omega_m t}] \\
&= \frac{1}{2}E_0 e^{j\omega_c t}[\sqrt{1 + {J_0}^2(m_{h1})}\, e^{jtan^{-1}J_0(m_{h1})} + J_1(m_{h1})e^{j(\omega_m t + \pi/2)} \\
&\qquad + J_1(m_{h1})e^{-j(\omega_m t - \pi/2)}],
\end{aligned}
\tag{2.1}
$$

where V_b is set as $V_\pi/2$, m_{h1} is the modulation index $\pi V_1 A(t)/V_\pi$, and $J_n(\beta)$ is the Bessel function of the first kind of order *n*. The Bessel function rapidly reduces with the increase of the order n in this range, so we just consider the 0th- and 1st-order Bessel functions. In Equation (2.1), the central optical carrier is with large DC component and little data information, which is different from the method based on two modulator [49]. As Figure 2.4(a) shows, the extinction ratio induced by data information for the central optical carrier is less than 2.5 dB; for the ODSB format, the m_{h1} is usually less than 1.6, in other words, the amplitude of the driving RF signal is less than $0.5V_\pi$.

For OSSB+C scheme, the bias point should be set at $V_\pi/2$, and the two arms of MZM are driven by two RF signals with equal amplitude and ±π/2 phase shift. The electrical output of MZM is

$$E_0 e^{j\omega_c t} \cdot \frac{1}{2}\left[\exp\left(j\frac{\pi}{V_\pi}\frac{V_1}{2}A(t)cos\omega_m t\right) + \exp\left(j\frac{\pi}{V_\pi}(\frac{V_1}{2}A(t)cos(\omega_m t - \frac{\pi}{2}) + V_b)\right)\right]$$

$$= E_0 e^{j\omega_c t} \cdot \frac{1}{2}\left[\exp\left(j\frac{\pi}{V_\pi}\frac{V_1}{2}A(t)cos\omega_m t\right) + \exp\left(j\frac{\pi}{V_\pi}\frac{V_1}{2}A(t)sin\omega_m t\right)\right]$$

$$= \frac{1}{2}E_0 e^{j\omega_c t}[\sum_{k=-\infty}^{\infty}(j^k + j)J_k(m_{h1})e^{jk\omega_m t}]$$

$$\approx \frac{1}{2}E_0 e^{j\omega_c t} \cdot [(1+j)J_0(m_{h1}) + 2jJ_1(m_{h1})e^{j\omega_m t}], \quad (2.2)$$

where phase difference between two driving RF signals is -π/2, and m_{h1} is $\pi V_1 A(t)/2V_\pi$. In Equation (2.2), the lower 1st-order sideband is suppressed, and the central optical carrier is also with large DC component and small extinction ratio as Figure 2.4(b) shows. The amplitude of the driving RF signal is usually less than $0.25V_\pi$ for the OSSB+C format (m_{h1} < 0.8).

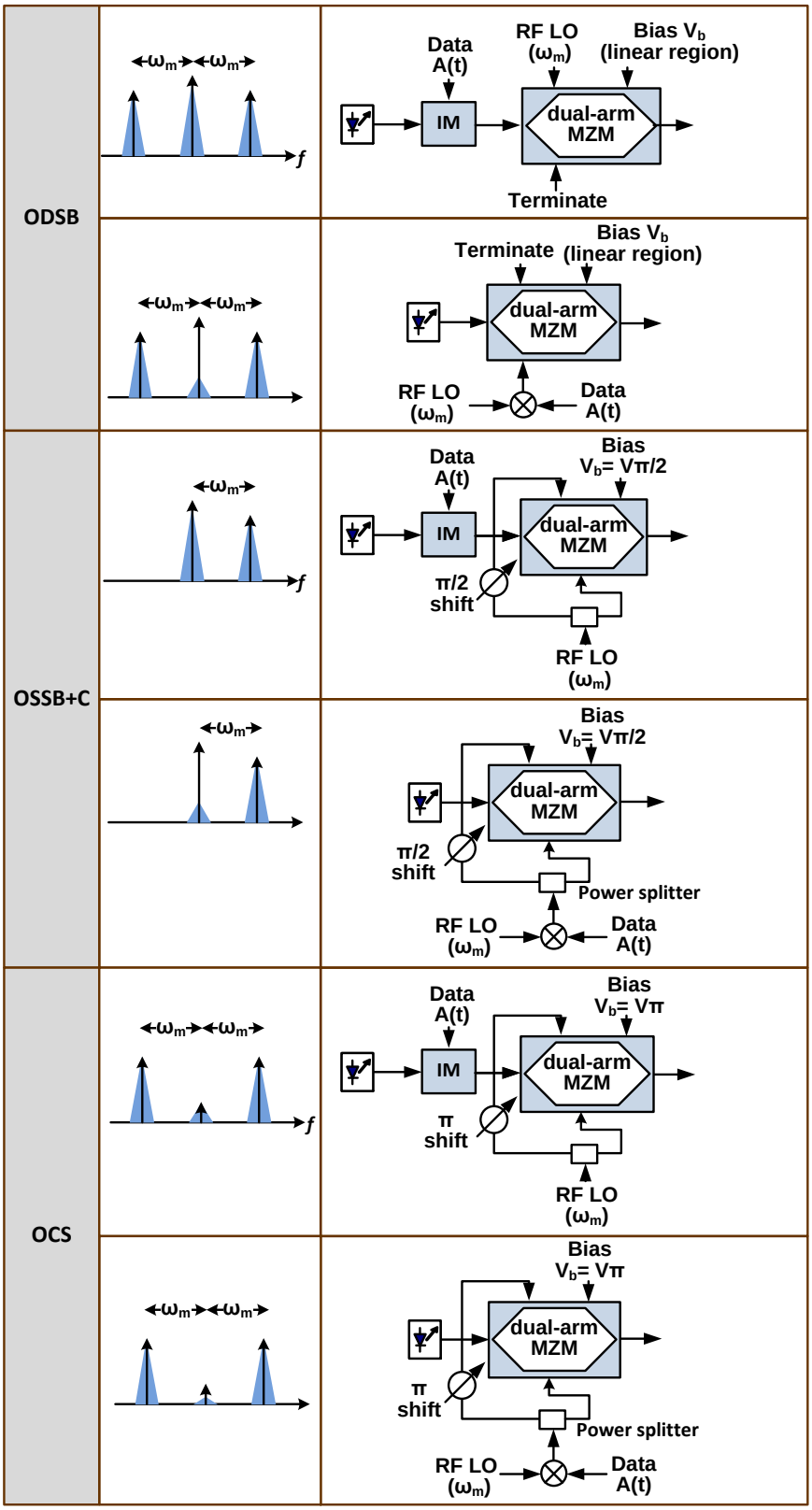

Figure 2.3. Optical mmW generation based on external modulation with ODSB, OSSB+C, and OCS formats.

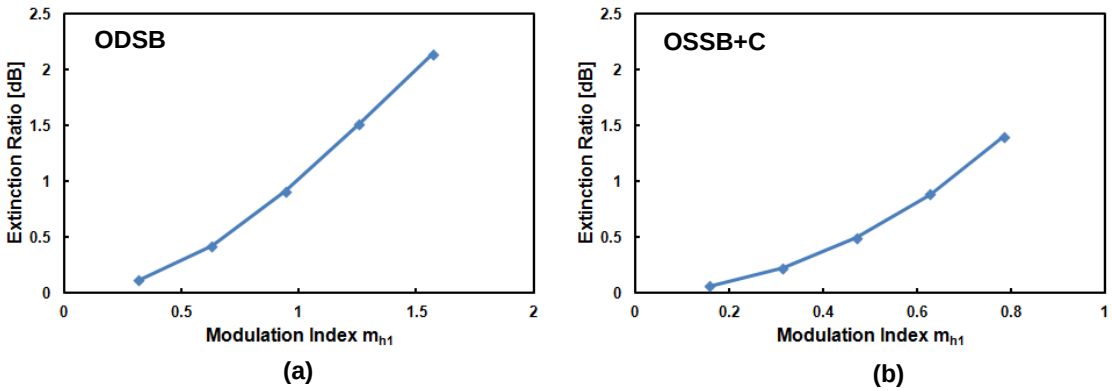

Figure 2.4. Extinction ratios induced by data information for the central optical carrier with the (a) ODSB and (b) OSSB+C format.

For OCS scheme, the bias point should be set at V_π, and the two arms of MZM are driven by two RF signals with equal amplitude and out of phase. The electrical output of MZM is

$$E_0 e^{j\omega_c t} \cdot \frac{1}{2}\left[\exp\left(j\frac{\pi}{V_\pi}\frac{V_1}{2}A(t)cos\omega_m t\right) + \exp\left(j\frac{\pi}{V_\pi}(\frac{V_1}{2}A(t)cos(\omega_m t - \pi) + V_b)\right)\right]$$

$$= E_0 e^{j\omega_c t} \cdot \frac{1}{2}\left[\exp\left(j\frac{\pi}{V_\pi}\frac{V_1}{2}A(t)cos\omega_m t\right) - \exp\left(j\frac{\pi}{V_\pi}\frac{V_1}{2}A(t)cos\omega_m t\right)\right]$$

$$= \frac{1}{2}E_0 e^{j\omega_c t}[\sum_{k=-\infty}^{\infty} j^k(1-(-1)^k)J_k(m_{h1})e^{jk\omega_m t}]$$

$$\approx \frac{1}{2}E_0 e^{j\omega_c t}[2jJ_1(m_{h1})e^{j\omega_m t} + 2jJ_1(m_{h1})e^{-j\omega_m t}], \quad (2.3)$$

where m_{h1} is also $\pi V_1 A(t)/2V_\pi$, and the optical carrier is suppressed.

To generate a mmW signal with frequency of ω_m, the ODSB needs a RF LO at ω_m, and its spectrum occupies the largest bandwidth, which is about $2\omega_m$. For the OSSB+C, the occupied bandwidth is only ω_m, but it also needs a RF LO at ω_m. As for the OCS scheme, it only need a RF LO at $\omega_m/2$. In other words, the OCS scheme can double the radio frequency to obviate the use of a RF LO with high frequency.

Another mmW generation based on external IM is to use an expensive modulator known as an integrated MZM, also called the IQ modulator. This modulator, which consists of two parallel MZMs and requires cautious bias voltage control, has been shown in previous studies to successfully generate a mmW signal with frequency doubling OSSB+C format [43] as well as a frequency sextupling scheme [44].

For the generation of mmW signals achieved by the phase modulation [40-42, 56], a small LO signal is used to drive an optical phase modulator (PM) to produce several sidebands. The OCS scheme can also be achieved by coupling with an optical filter (OF) to suppress the optical carrier and keep the 1st-order sidebands. Similar to the OCS scheme of the external IM, the PM with an OCS filter can also double the radio frequency, but its structure is more simple and stable because there is no need to adjust the bias voltage or the offsets of the driving RF signals.

2.2.3 Optical Millimeter-Wave Generation Based on Phase Modulation

As mentioned in section 2.2.1, a RoF system with OCS format is with lower requirements for the frequency of RF LOs and the bandwidth of electronic components. The OCS scheme can be commonly realized either by biasing a MZM at its null transmission point to suppress the optical carrier, or through the external narrowband optical filtering to select specific sidebands while rejecting the carrier. However, the former method suffers from bias drafting and requires complicated current controls, while the latter one is sensitive to the wavelength offset between the laser source and the narrowband OFs, thus compromises the stability of generated optical mmWs.

In reference [42], two 1st-order sidebands of a phase-modulated optical carrier are analyzed to be inherently out-of-phase with each other. It is evident that the 1st harmonic produced by the beatings between center carrier and 1st-order sidebands will be cancelled after optical heterodyning while the out-of-phase condition is maintained. Therefore, the beating frequency of a phase-modulated optical signal is twice as high as the driving RF

signal. Therefore, a novel frequency-doubled optical mmW generation scheme based on phase modulation without OCS is proposed [63].

The schematic structure is shown in Figure 2.5. A phase-modulated optical carrier is generated by modulating the phase of a CW lightwave with a sinusoid microwave signal, and its complex electrical field can be approximated by

$$E_{PM}(t) = E_0 e^{j\omega_c t} e^{j\beta cos\omega_m t} = E_0 \sum_{k=-\infty}^{\infty} j^k J_k(\beta) e^{j[(\omega_c + k\omega_m)t]}, \quad (2.4)$$

where β is the phase modulation index (MI), and ω_m is the angular frequency of the modulating microwave signal. The phase-modulated optical carrier features multiple sidebands, which are equally separated in frequency by ω_m. After rejecting higher-order sidebands by using an optical filter with a wide bandwidth (2 to 4ω_m), the resulting phase-modulated optical carrier mainly consists of a central carrier and the 1st- and 2nd-order sidebands, which is given by

$$E_{PM}(t) \approx E_0 \left\{ \alpha_0 J_0(\beta) e^{j\omega_c t} + \alpha_1 J_1(\beta) e^{j\left((\omega_c + \omega_m)t + \frac{\pi}{2}\right)} - \alpha_{-1} J_1(\beta) e^{j\left((\omega_c - \omega_m)t - \frac{\pi}{2}\right)} \right.$$
$$\left. - \alpha_2 J_2(\beta) e^{j(\omega_c + 2\omega_m)t} - \alpha_{-2} J_2(\beta) e^{j(\omega_c - 2\omega_m)t} \right\}, \quad (2.5)$$

where α_0, α_1, α_{-1}, α_2, and α_{-2} are the filter losses for each spectral band. The filter spectrum is assumed to be fully symmetric ($\alpha_1 = \alpha_{-1}$ and $\alpha_2 = \alpha_{-2}$), and no group delay is introduced. As shown in Equation (2.5), the 1st-order upper and lower sidebands exhibit phase-shift (out-of-phase) after the phase modulation and the optical filtering, and thus the detected photocurrent is given by

$$I(t) = \mu E_0{}^2\{[\alpha_0{}^2 J_0{}^2(\beta) + 2\alpha_1{}^2 J_1{}^2(\beta) + 2\alpha_2{}^2 J_2{}^2(\beta)] + [-4\alpha_0\alpha_2 J_0(\beta)J_2(\beta) + 2\alpha_1{}^2 J_1{}^2(\beta)]\cos(2\omega_m t)\}, \quad (2.6)$$

where μ is the responsivity of the PD. Clearly, the output photocurrent contains only the DC and the 2nd harmonic, which implies that suppressing the center carrier of the phase-modulated optical carrier to double its beating frequency is unnecessary. Moreover, the laser phase noise is canceled out after the heterodyning.

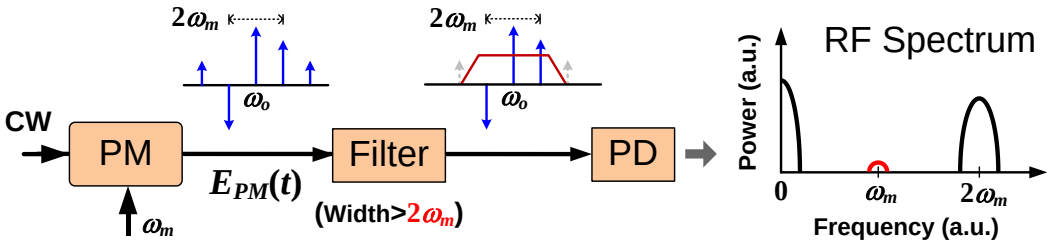

Figure 2.5. Block diagram of the optical mmW generation using a PM without OCS.

Figure 2.6(a) shows the simulated RF power variation of the 1st and 2nd harmonics versus the wavelength of the PM optical carrier relative to 1550 nm, where the swept frequency ω_m is 30 GHz and the 3-dB bandwidth of 4th-order Gaussian filter is 100 GHz. The suppression ratio of the 1st harmonic relative to the second one is larger than 18 dB within the detuning range of ±0.016 nm, and the insets illustrate the corresponding RF spectra. Figure 2.6(b) illustrates the requirement of the filter bandwidth in the proposed approach. It is found that the 70- to 100-GHz bandwidth is ideal to generate a 60-GHz carrier with the RF power variation < 1.8 dB. In addition, when the bandwidth is larger than 100 GHz, the 60-GHz RF power will reduce significantly since the 2nd-order sidebands will act negatively to the amplitude of the 2nd harmonics as indicated in Equation (2.5). Figure 2.6(c) shows that for a filter bandwidth of 100 GHz the carrier frequency of the optical mmW is widely tunable from 60- to 90-GHz with the

RF power variation < 2 dB. We also simulate the power fluctuation of the 1st and 2nd harmonics against the distance of fiber transmission with CD coefficient set to 2.7 or 17 ps/nm•km (Figure 2.6(d)). The pre-eliminated 1st harmonic is gradually recovered during the transmission since 1st-order sidebands in Equation (2.5) will suffer uneven dispersive phase delays, which will turn themselves into in-phase at a rate proportional to the amount of CD coefficients [42]. Therefore, to achieve frequency doubling without inducing the 1st harmonic at a given fiber distance, the CD coefficient should be minimized.

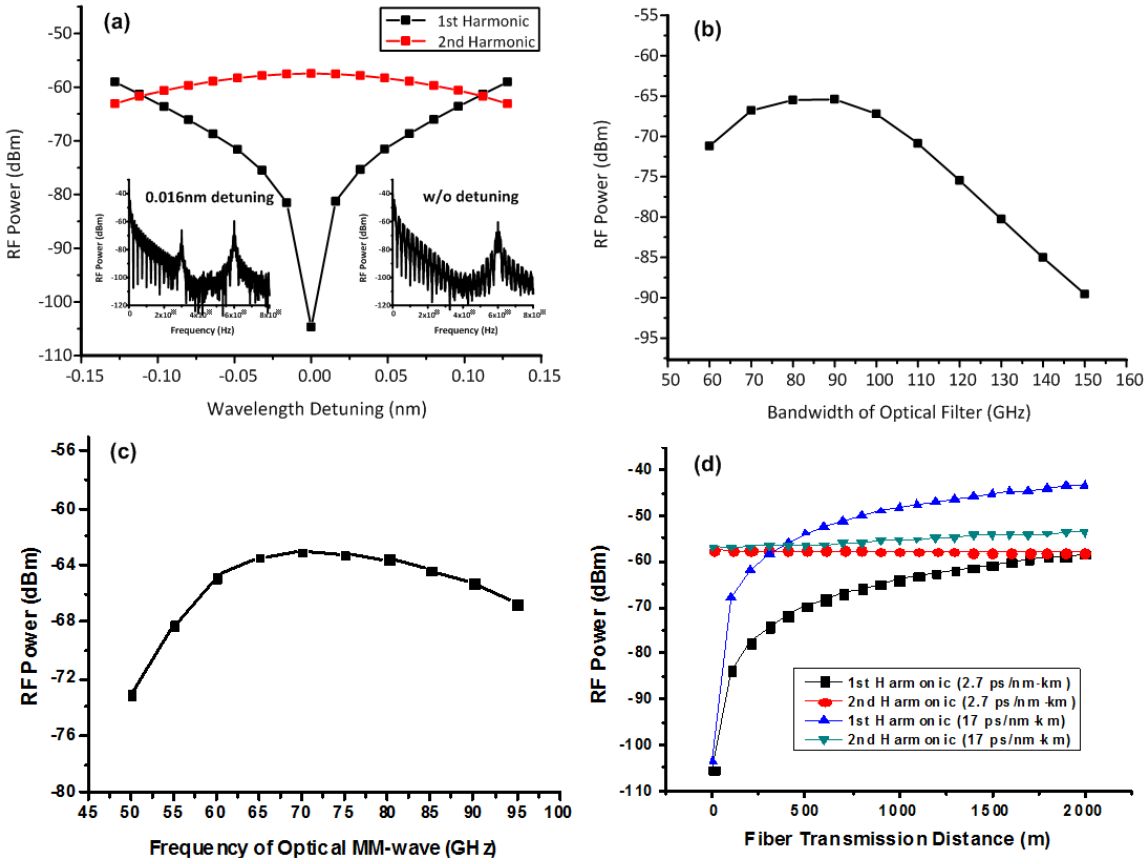

Figure 2.6. Simulated RF power variation of (a) the 1st (30 GHz) and 2nd (60 GHz) harmonics at a detuned wavelength relative to 1550 nm, and (b) the 2nd harmonics (60 GHz) versus filter bandwidth, (c) the generated optical mmW at different carrier frequencies from 50 to 95 GHz, and (d) the simulated RF power variation of the 1st and 2nd harmonics versus the distance of fiber transmission with CD coefficient set to 2.7 or 17 ps/nm·km.

Figure 2.7 shows an experimental setup of the proposed 60-GHz RoF system using a PM without OCS. This test link comprises of a CO, a BS, and a subscriber unit. In the CO, a 2.5-Gb/s pseudorandom bit sequence (PRBS) baseband signal with a word length of 2^{31}-1 is going to directly modulate an optical transmitter (Tx) at 1553.2 nm, and is then fed into a $LiNbO_3$ optical PM with V_π of 4 V, which is driven by a 30-GHz RF sinusoidal clock at 2.5 V ($\beta \approx 0.98$ rad) to generate a PM optical carrier with 30-GHz-spaced upper and lower sidebands. A fiber Bragg grating (FBG) filter with a flat group delay over its 3-dB bandwidth of 0.65 nm is then utilized to select the central optical carrier and the 1st-order upper and lower sidebands and to suppress the higher-order sidebands. After the wideband filtering, a 60-GHz carrier can be observed while preserving the nature of π out of phase between the two 1st-order sidebands. The fiber distance between the CO and BS is designed at 250 m to emulate the environment of an in-building wireless distribution. After the fiber transmission, the optical mmW is directly detected by a 50-GHz PD, boosted by a high-power EA with 5-GHz bandwidth centered at 60-GHz and transmitted through a double-ridge guide rectangular horn antennas with 25 dBi gain at the range of 50-GHz to 75-GHz. The optical input power to the PD is about 0 dBm, and the output power of the high-power EA is about -4 dBm. Thus, the resulting EIRP is around 21 dBm, adhering to the 40-dBm limitation for in-building 60-GHz radio by FCC regulation. Another 60-GHz horn antenna having 25-dBi gain is placed at a couple of meters away, the received, amplified 60-GHz is down-converted to the baseband data by using a balanced mixer, a 2.8-GHz low-pass filter (LPF), and a 60-GHz electrical LO which is generated by 15-GHz clock signal and a 1:4 frequency multiplier (FM).

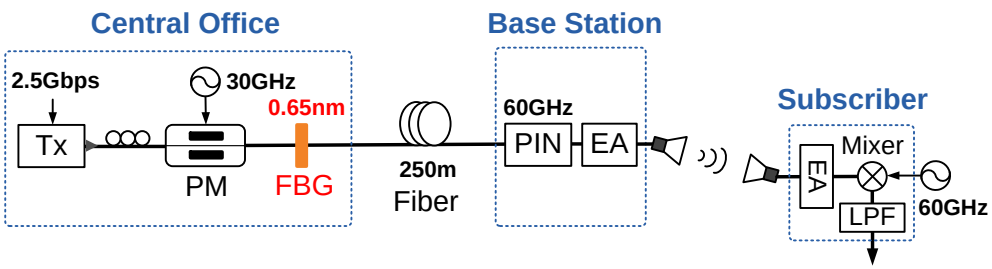

Figure 2.7. Experimental setup of an in-building RoF link to assess a 60-GHz optical mmW using a PM without OCS.

Figure 2.8 illustrates the measured optical spectra of the generated PM optical carrier before and after the FBG, and the FBG reflective spectrum in the CO. Since the FBG spectrum is not fully symmetric, the central wavelength of FBG is tuned to eliminate the 1st harmonics at 30 GHz as possible.

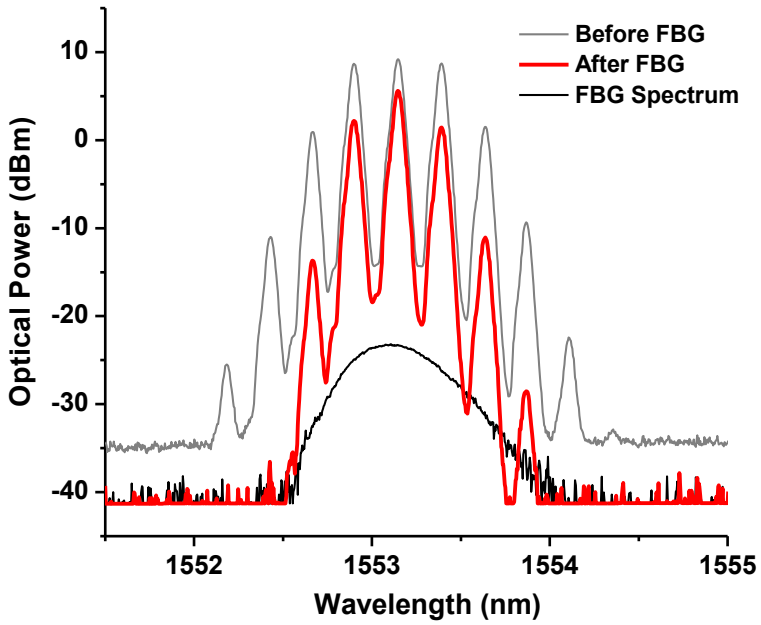

Figure 2.8. Measured optical spectra of the phase-modulated optical carrier before and after the FBG, and the FBG reflective spectrum.

Figure 2.9 displays the bit error rate (BER) as a function of the distance of wireless transmission. To investigate the impact of chromatic dispersion on the generated optical mmW, two types of 250-m fiber are employed: standard single-mode fiber (SSMF, ex. SMF-28) and dispersion-shifted fiber (DSF). The results show that both cases have equivalent performance since the 2nd harmonic at 60 GHz is much immune to the dispersion effect as illustrated in Figure 2.6(d), and the 1st harmonic will always be blocked out by the band-limited EA. Error-free wireless distance is 3 m, which is extendable by increasing the output power of EA. The insets illustrate the measured electrical eye diagrams of the mmW signals for both cases. Similar to the previous analysis, the 1st harmonic at 30 GHz is revived after the SMF-28 transmission, but is negligible in the DSF case.

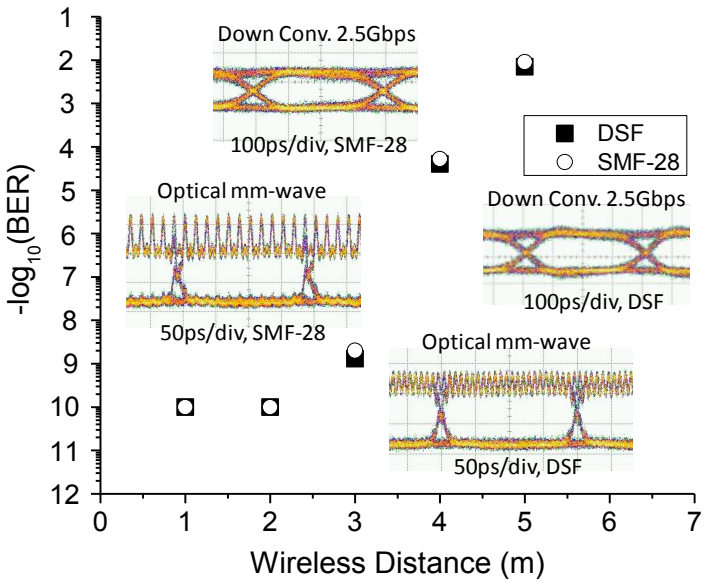

Figure 2.9. BER versus the distance of wireless transmission for the link composed of DSF and SMF-28.

Based on the previous experimental results, the undesired 1st harmonic after the O/E conversion is weak after a length of DSF or with 1310-nm lightwave sources, which

has zero CD and is commonly adopted in current broadband distributed antenna systems (DASs). However, for a long SSMF transmission with C-band (1530-1565 nm) lightwave sources, the enhanced 1st harmonic will become a source of intra-band interference in a multi-band RoF system. Therefore, as part of the effort to resolve this problem, another novel mmW RoF scheme with OCS through the MI enhancement is proposed [64].

This proposed scheme can achieve a superior carrier-suppression ratio (CSR) with highly relaxed bandwidth requirement for optical filters, which can be implemented in a simple and cost-effective manner and is potential for the future integration with other WDM optical access systems through the sharing of remote wavelength splitters. Figure 2.10 illustrates the concept (a) and schematic structure (b) of the proposed scheme for mmW generation with OCS by simply using a modulation index enhanced-phase modulator (MIE-PM). The phase-modulated optical carrier features multiple optical sidebands centered at ω_c and separated by ω_m as shown in Equation (2.4). Inset (i) of Figure 2.10(a) shows the values of Bessel function of the first kind for orders n=0, 1, and 2 with different MIs. As can be seen, when the phase MI increases from β_1 to β_2, the amplitude of the central carrier will decrease accordingly from $J_0(\beta_1)$ to $J_0(\beta_2)$, which means that the optical carrier would be suppressed or even entirely removed when the driving voltage is high.

Additionally, a wideband filter with bandwidth of ~$2\omega_m$ (for a single-channel scheme) or an arrayed-waveguide grating (AWG) with periodic passbands of ~$2\omega_m$ (for a WDM scheme) is used to separate the specific carriers as shown in Figure 2.10(b). When the MI is equal to β_2, the power of central optical carrier decreases much to be very low, and the photocurrent of the output signal can be written as

$$I(t) \approx \mu {E_0}^2 \{ \left[2{\alpha_1}^2 {J_1}^2(\beta) + 2{\alpha_2}^2 {J_2}^2(\beta) \right] + \left[2{\alpha_1}^2 {J_1}^2(\beta) \right] \cos(2\omega_m t)] \}. \quad (2.7)$$

Equation (2.7) shows that there are only baseband and mmW signal at $2\omega_m$. Since the

V_π of phase modulator is smaller than the normal MZM, the required power level of the RF driving signal for enhancing the MI is still acceptable in our proposed scheme.

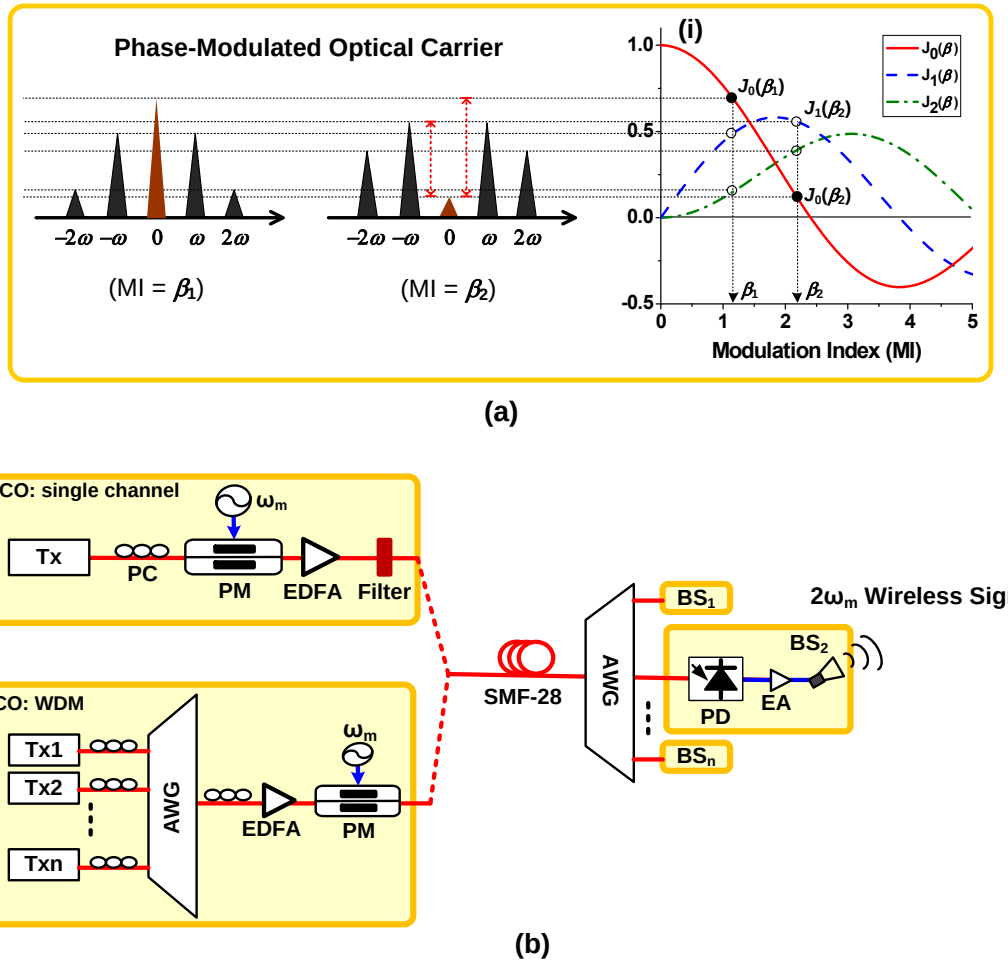

Figure 2.10. (a) Conceptual diagram and (b) schematic structure of the proposed optical mmW generation with OCS using a MIE-PM: single channel or WDM case.

Figure 2.11(a) shows that the CSR of the proposed MIE-PM scheme can be higher than 25 dB with the MI set between 2.39 and 2.43, and can ultimately go up to 55 dB at MI = 2.41. Moreover, in Figure 2.11(b), power levels of the 1st- and 2nd-order sidebands keep the same, and only the optical carrier changes with the increase of MI to generate different CSRs. It means there is no trade-off between the higher-order sidebands and the amount of CSR at this range of MI.

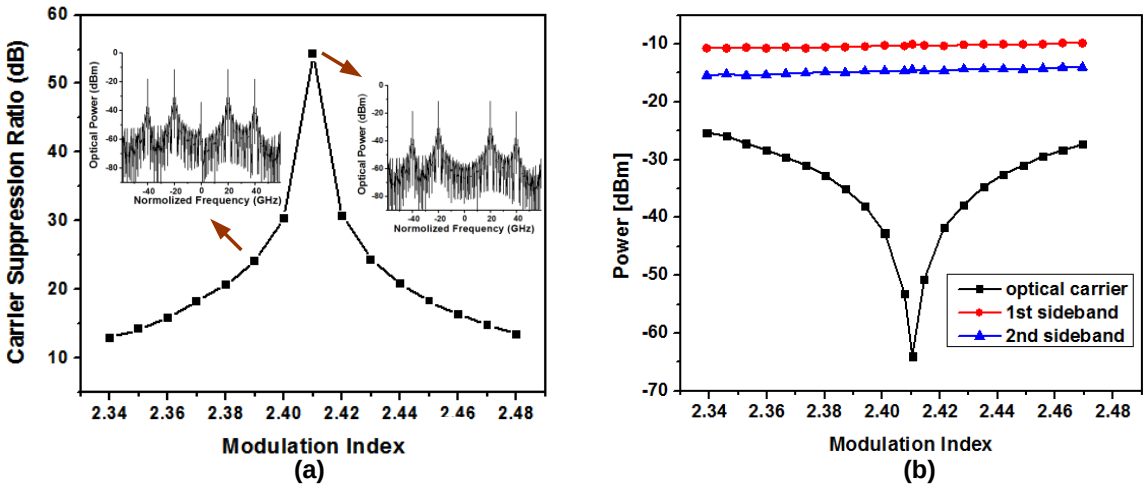

Figure 2.11. Simulation analyses of (a) CSR versus MI for the MIE-PM scheme and (b) power levels of optical carrier, the 1st- and 2nd-order sidebands versus MI for the MIE-PM scheme.

Compared with the OCS scheme using a minimum-point-biased MZM, the simulated results in Figure 2.12(a) show that its maximum CSR is only ~37 dB at V_{bias} = V_{π}, and the drift of bias voltage would degrade CSR to a certain extent. The relative bias detuning is defined as $(V_{bias} - V_{\pi})/V_{\pi} \cdot 100\%$. Figure 2.12(b) depicts that 50- to 100-GHz is an ideal range of filter bandwidth for generating a 40-GHz carrier with harmonics-suppression ratio (HSR) of larger than 20 dB in back-to-back (B2B, BTB) case; the HSR is the RF power difference between the 1st and 2nd harmonics. However, through a 10-km SSMF, the HSR will suddenly reduce while the filter bandwidth is larger than 60 GHz ($3\omega_m$). This is because that π out-of-phase condition for two 1st-order sidebands of the MIE-PM scheme is violated by the CD-induced phase rotation, and then the 1st harmonic is generated by the beatings between the 1st- and 2nd-order sidebands. Nevertheless, this 1st harmonic would not affect the RF power of the 2nd harmonic (40 GHz) after a 10-km fiber transmission, which remains constant regardless of the change in the filter bandwidth. The HSR reduction can be improved by using a narrower filter to suppress the 2nd-order sidebands more.

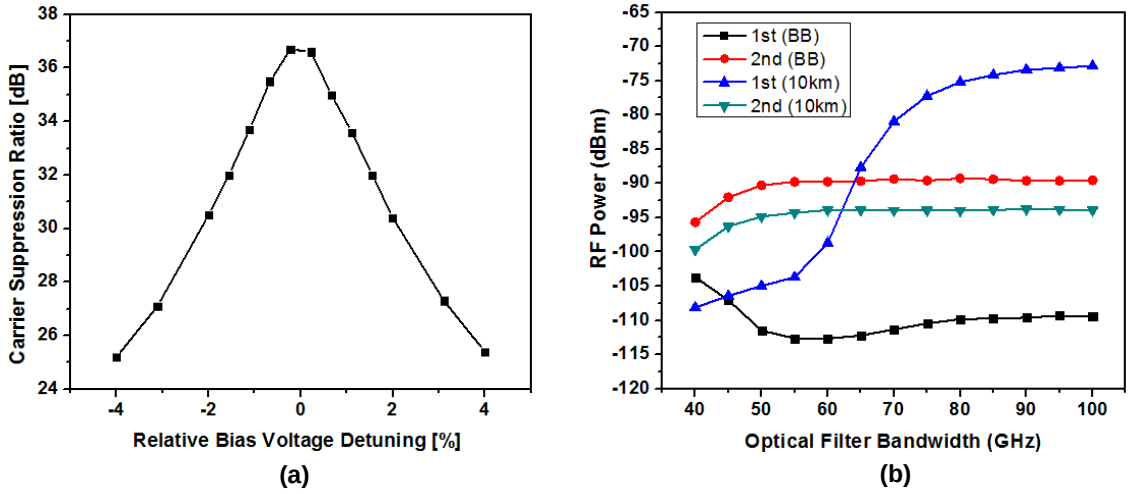

Figure 2.12. (a) CSR versus relative bias voltage detuning for the carrier-suppression scheme using minimum-point biased MZM, and (b) RF power of the 1st and 2nd harmonics versus the 3-dB filter bandwidth for the MIE-PM scheme.

Figure 2.13(a) shows an experimental setup for the proposed RoF system with the MIE-PM to generate one 40-GHz optical mmW. At the CO, a 2.5-Gb/s PRBS signal with a word length of 2^{31}-1 is used to modulate a CW lightwave at 1553.2 nm, and then fed into a PM with V_π of ~3.8 V driven by a 20-GHz sinusoidal wave of 5.8 V_{pp} (MI = 2.4) to achieve optical up-conversion with OCS. A 50/100-GHz optical IL is used to select the 1st-order sidebands and to suppress higher-order ones. After a 10-km fiber transmission, the O/E conversion of the 40-GHz signal is completed by a 50-GHz PD following by a PA. A pair of 40-GHz horn antennas having 20 dBi gain are utilized to broadcast and receive the 40-GHz signal. After the wireless transmission, the down-conversion is achieved by a EA, a mixer, a 10-GHz clock source, a 1×4 FM and a 2.8-GHz LPF. For comparison, we also evaluate the traditional scheme by replacing the 50/100-GHz IL with a 25/50-GHz IL functioning as a narrow-band carrier-suppressing filter and reducing the RF voltage to about 2.8 V_{pp} (MI = 1.2). We plot the BER against the distance of wireless transmission for our and traditional schemes after a 10-km SMF-28 (Figure 2.13(b)). Both cases have similar performance of achieving 3-m error-free distance with

EIRP = ~17 dBm, and the rapid BER drop reflects the free-space loss characteristic of a 40-GHz radio at a given transmitting power which can be explained by the Friis transmission equation (Equation (1.1)). The sudden drop in BER shown in Figure 2.13(b) is also caused by the weak input signal power to the BER analyzer, and could be improved by increasing the gain of EA used after the down-conversion. In addition, the insets show the measured 2.5-Gb/s down-converted signal at different distances for the MIE-PM case.

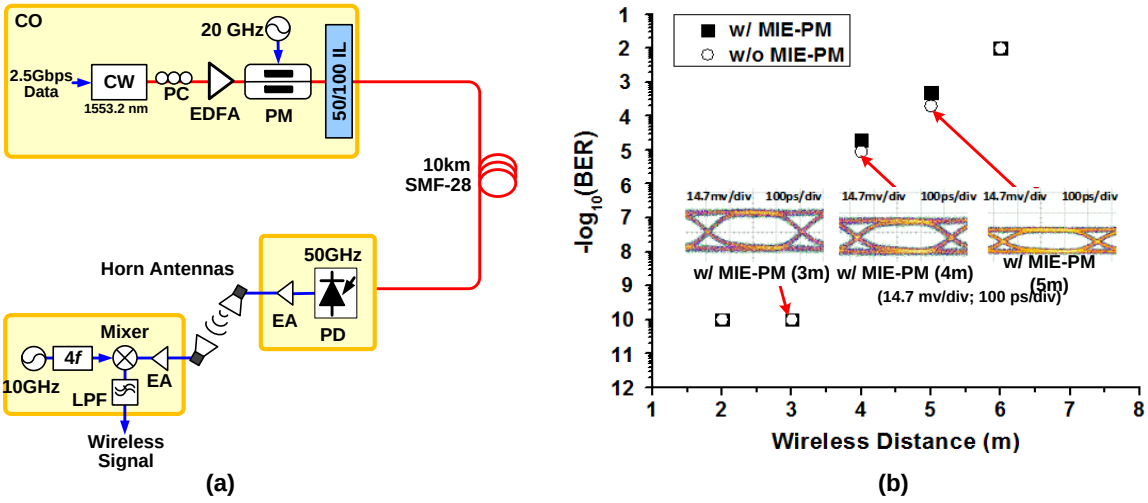

Figure 2.13. (a) Experimental setup of the proposed 40-GHz RoF system based on the MIE-PM for the single-channel case. (b) BER measurements for the single-channel case over a combined optical-wireless link.

We utilized three CW lightwaves at wavelengths from 1557.32 to 1558.92 nm with 100-GHz spacing to evaluate the MIE-PM scheme in a WDM network environment in Figure 2.14. The center channel and two adjacent channels carry two independent 2.5-Gb/s data, respectively, to investigate the crosstalk effects between channels. This WDM scheme can be accomplished by using an AWG to separate the specific carriers without any IL.

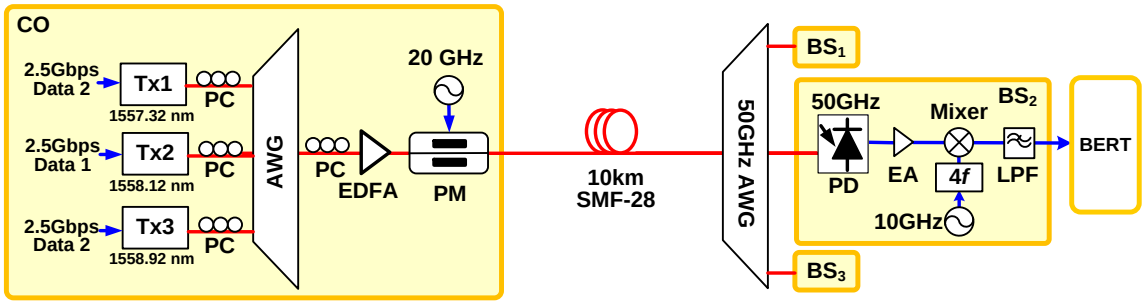

Figure 2.14. Experimental setup of the proposed 40-GHz RoF system based on the MIE-PM for the WDM case.

Figure 2.15(a) and 2.15(b) illustrate the measured optical spectra of the generated optical carrier with and without the MIE-PM, respectively. Over 20-dB CSR are observed for both cases. The BER measurements for two cases are shown in Figure 2.16(a). After a 10-km SMF-28 transmission, the measured power penalties are about 0.5 dB for both two schemes at the BER of 10^{-9}. The receiver sensitivity for the traditional scheme (without the MIE-PM) is a little better than that of the proposed MIE-PM scheme by 0.5 dB. This is because the crosstalk effects from adjacent channels are severer as the MI increases. However, it is acceptable to have only 0.5 dB penalty but make structure simpler and cost lower by comparing the traditional scheme with an expensive narrowband filter.

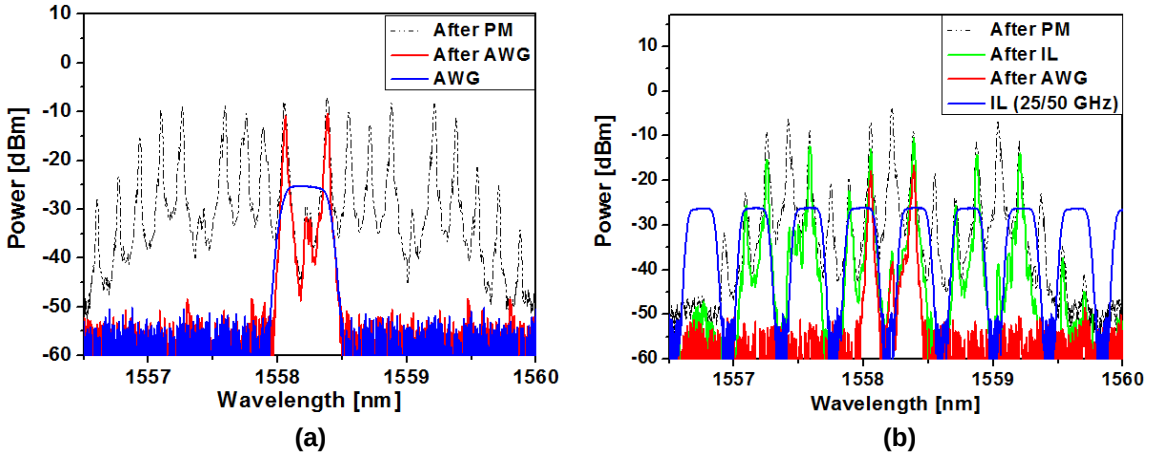

Figure 2.15. Measured optical spectra of the WDM optical mmW generation scheme (a) with and (b) without the MIE-PM.

We also compare the BERs of the single-channel case and the WDM case to investigate the influence brought by adjacent channels. In Figure 2.16(a), the penalty from the crosstalk is less than 4 dB for our proposed scheme after a 10-km SMF-28 transmission. Moreover, Figure 2.16(b) shows four optical eye diagrams with different MIs after a 10-km SMF-28, and we can find that the proposed MIE-PM scheme with higher CSR can avoid the interference from the 1st harmonic (20 GHz) as compared to the case with a lower MI.

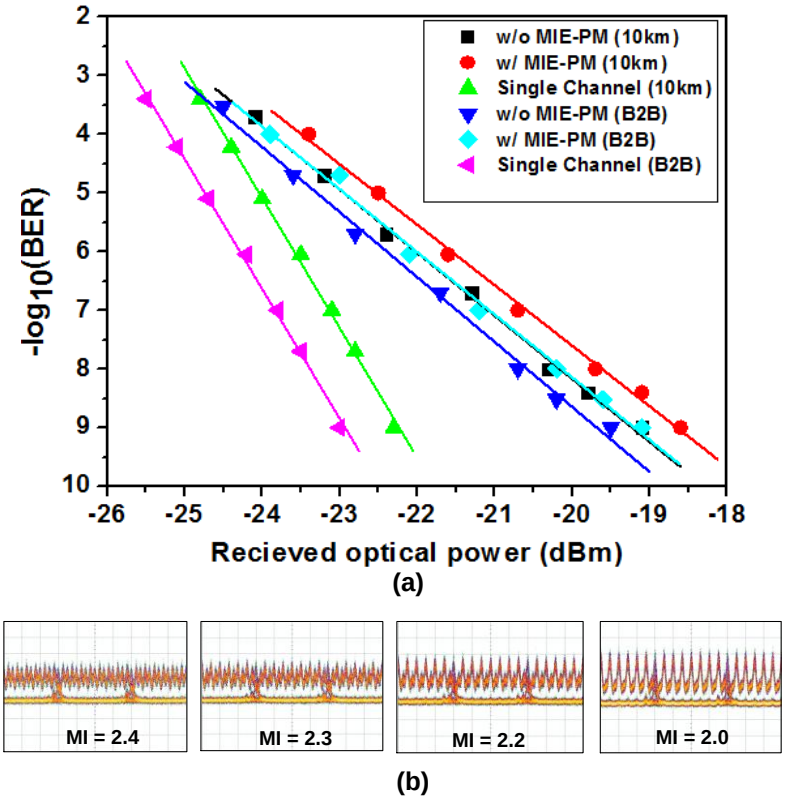

Figure 2.16. (a) The WDM case over a 10-km SMF-28 with and without the MIE-PM, and (b) optical eye diagrams with different MIs at 2.5 Gb/s (100 ps/div).

Based on the phase modulation, we designed and experimentally demonstrate two frequency-doubled mmW generation methods. No narrowband optical filtering or complicated bias control is required for both schemes. The first one can achieve frequency doubling without suppressing the carrier by taking advantages of the out-of-

phase property between sidebands of a phase-modulated optical carrier. We also conclude that launching a low-cost zero-dispersion wavelength over SMF-28 is the best scheme for the first proposed method to mitigate the intra-band interference induced by CD in multi-band systems. The second proposed method is designed to solve the interference problem in the first method: it is a carrier-eliminated scheme using MIE-PM. Therefore, we believe the proposed MIE-PM scheme for simplifying the structure and lowering the cost of optical mmW transmitters is promising for the future WDM mmW wireless over fiber access networks.

2.3 Fiber Transmission Impairments

For a full-duplex optical system with mmW signals, the main fiber transmission impairments are induced by fiber chromatic dispersion and backscattering interference. The effects induced by CD would limit the fiber transmission distance, and the theoretical analysis is presented in this section. Then a novel architecture of long-reach 60-GHz RoF system base on the remote OCS (ROCS) is proposed to overcome this dispersion issue. Bidirectional transmission suffers backscattering interference, which is also introduced in this section.

2.3.1 Fiber Chromatic Dispersion-Induced Effects

Due to chromatic dispersion, the optical carrier and other subcarriers are transmitted over fiber with different velocities. The time shift $\Delta t_{kk'}$ of the codes carried by at $\omega_c+k\omega_m$ to that at $\omega_c+k\omega_m$ is

$$\Delta t_{kk'} = \frac{\beta(\omega_c + k\omega_m)}{\omega_c + k\omega_m} z - \frac{\beta(\omega_c + k'\omega_m)}{\omega_c + k'\omega_m} z, \tag{2.8}$$

where β is the propagation constant, and z is the fiber length. By considering the Taylor's

expansion of the propagation constant

$$\beta(\omega_c \pm k\omega_m) = \beta(\omega_c) \pm k\omega_m\beta'(\omega_c) + \frac{1}{2}(k\omega_m)^2\beta''(\omega_c) + \cdots , \qquad (2.9)$$

and the time shift becomes [49]

$$\Delta t_{kk'} \approx (k - k')\omega_m{}^2\beta''(\omega_c)z = -(k - k')D\lambda_c^2 f_m C^{-1} z. \qquad (2.10)$$

Here, $\beta''(\omega_c) = D\lambda_c^2/2\pi c$; D is dispersion coefficient, λ_c is the wavelength of CW source, and C is light speed. When the time shift $\Delta t_{kk'}$ is closed to code width τ, the eye diagram will close. The code width τ is η/R, where η is duty cycle (return-to-zero (RZ): $0< \eta<1$ and non return-to-zero (NRZ): $\eta =1$), and R is the bit rate. The fiber transmission distance is limited by the code shift.

For the OCS scheme in Equation (2.3), the RF signal at $2\omega_m$ is generated by the beating between the upper 1st-order sideband ($k' = +1$) and the lower 1st-order sideband ($k' = -1$). Therefore, the fiber transmission distance should be shorter than l_{ocs}

$$l_{ocs} = \frac{\eta c}{2R\lambda_c^2 D f_m} . \qquad (2.11)$$

For example, the eye diagram of 2.5-Gb/s NRZ data at 60 GHz would totally close when the data is transmitted over a 50-km SSMF as shown in Figure 2.17. Normally, the maximum transmission distance, which can have error-free performance, is just half of $l_{ocs.}$

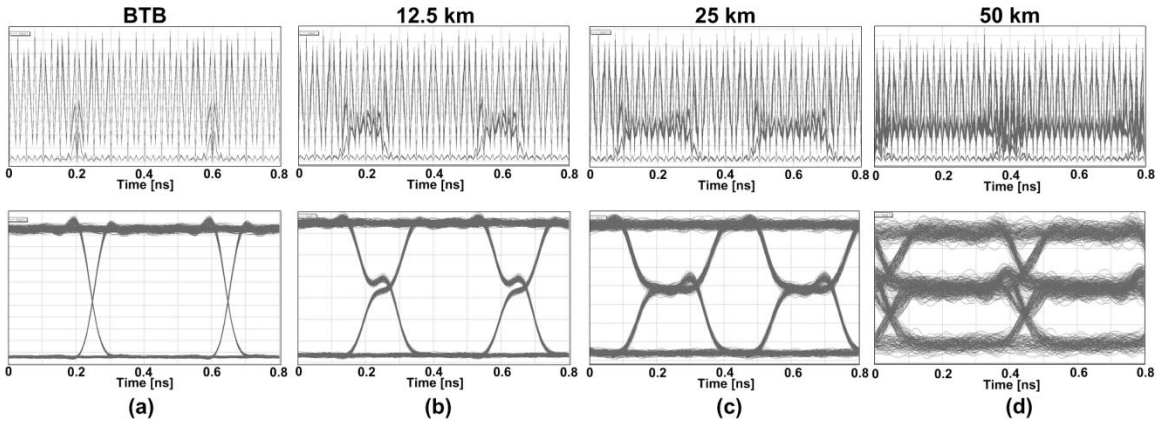

Figure 2.17. Simulated eye diagram of the OCS optical mmW signal at 60 GHz (upper), and the eye diagram of baseband data after down-conversion at (a) BTB, (b) 12.5-km, (c) 25-km, (d) 50-km SSMF transmission. (100 ps/div).

For the ODSB and OSSB+C scheme based on a single MZM represented in Equation (2.1) and (2.2), respectively, the RF signal at ω_m is generated by the beating between the optical carrier (k = 0) and both two 1st-order sidebands (ODSB) or only the upper 1st-order sideband (OSSB+C). However, the central optical carriers for both schemes are with large DC components, and the code information is mainly carried by the sidebands. It means the code-shifting problem induced by chromatic dispersion is relatively small. Moreover, if the OSSB+C and ODSB formats are produced by dual MZMs as [49] and Figure 2.3 show, the benefit of high tolerance to code-shifting problem vanishes due to the code information is also carried by their central optical carriers.

However, for the ODSB scheme, the dispersion causes the other impairment: fading effect [49]. We have already know that the RF signal at ω_m is from two beating harmonics. The photocurrent of the harmonic at ω_m can be expressed as

$$I_{\omega_{m,ODSB}} = 4\mu\sqrt{1 + {J_0}^2(m_{h1})}\, J_1(m_{h1}) \cos(\omega_m t - \omega_m \beta'(\omega_c) z)$$
$$\times \cos\left(\frac{1}{2}{\omega_m}^2 \beta''(\omega_c) z + tan^{-1}(m_{h1}) - \frac{\pi}{2}\right). \quad (2.12)$$

According to Equation (2.12), the photocurrent fades with the period of fiber transmission distance *L*.

$$L = \frac{-2\pi}{{\omega_m}^2 \beta''(\omega_c) z} = \frac{c}{{f_m}^2 D {\lambda_c}^2}\ . \quad (2.13)$$

The fading effect is due to the two beating signals are added constructively or destructively with the fading period. For a 2.5-Gb/s NRZ data at 60-GHz carrier frequency, *L* is about 2 m as shown in Figure 2.18(a). After the O/E conversion, down-conversion to baseband and a 2.5-GHz LPF, Figure 2.18(b) presents the electrical eye diagrams of 2.5-Gb/s data with different fiber transmission distances.

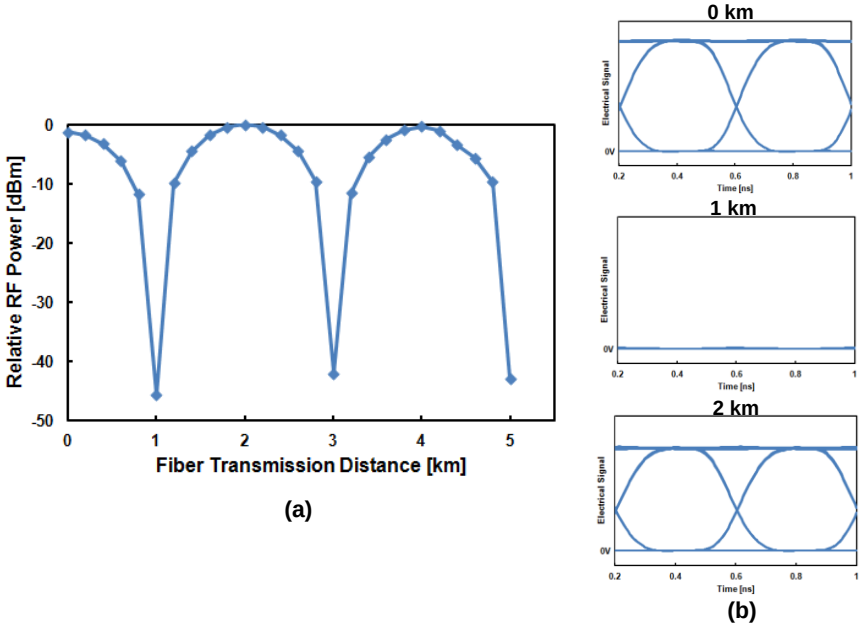

Figure 2.18. (a) Relative 60-GHz RF power versus fiber transmission distance. (b) Electrical eye diagrams of 2.5-Gb/s data after down-conversion and 2.5 GHz LPF.

Compared to the ODSB and OCS optical mmW formats, the OSSB+C format generated by one MZM eliminates the fading effect and time shifting of codes. Thus the fiber transmission distance can be extended. Once the distance issue is addressed, the long-reach mmW RoF scheme can then lower the implementation cost and cover the same area with fewer COs and as shown in Figure 2.19.

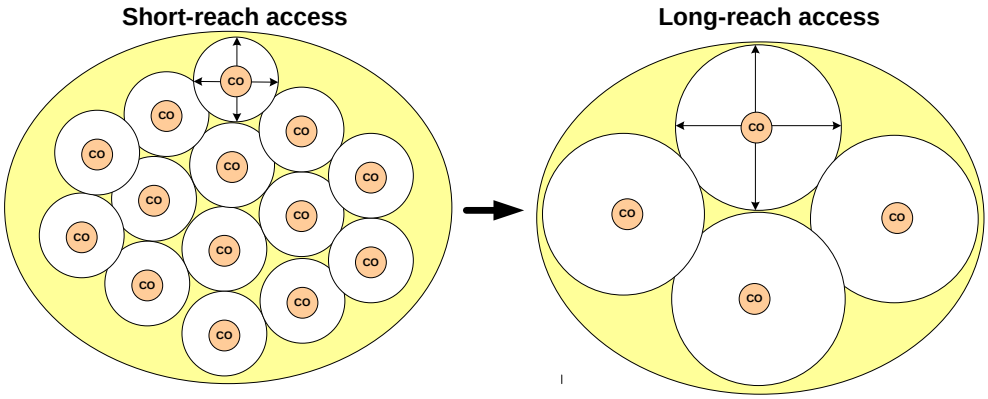

Figure 2.19. Short- and long-reach access networks.

2.3.2 ROCS Millimeter-Wave RoF System with Extended Reach

Except for the use of OSSB+C format, the transmission distance for the 60-GHz RoF system can be extended by remote mmW generation. A novel architecture of long-reach 60-GHz RoF system base on the remote OCS (ROCS) is proposed here [65]. The main difference between the proposed and conventional schemes is the location where the up-conversion of OCS signal is accomplished. For the conventional scheme, the generation of mmW signal is completed at the CO, while the downlink data in the proposed method is up-converted at a local exchange (LE). In this way, over long-distance delivery, the baseband data wouldn't suffer serious distortion caused by fiber chromatic dispersion for mmW until it arrives at LE.

By integrating with the WDM technique, this scheme can simultaneously transmit 8 channels with 2.5-Gb/s OOK hybrid wired and wireless data over a 125-km SSMF. The experimental setup of this scheme is shown in Figure 2.20. At the CO, eight optical carriers with 100-GHz channel spacing, followed by separate polarization controllers (PCs), are coupled together by an AWG and then modulated by a 2.5-Gb/s PRBS with a word length of 2^{31}-1 by an IM. After transmitted over a 100-km SSMF, the generated 8x2.5-Gb/s signals are fed into a LE and then amplified by an EDFA. To up-convert the baseband data to the 60-GHz band, a ROCS format is achieved by a dual-arm MZM biased at Vπ and driven by two complementary 30-GHz clock sources, which are generated by 1:4 FM and a 7.5-GHz clock source.

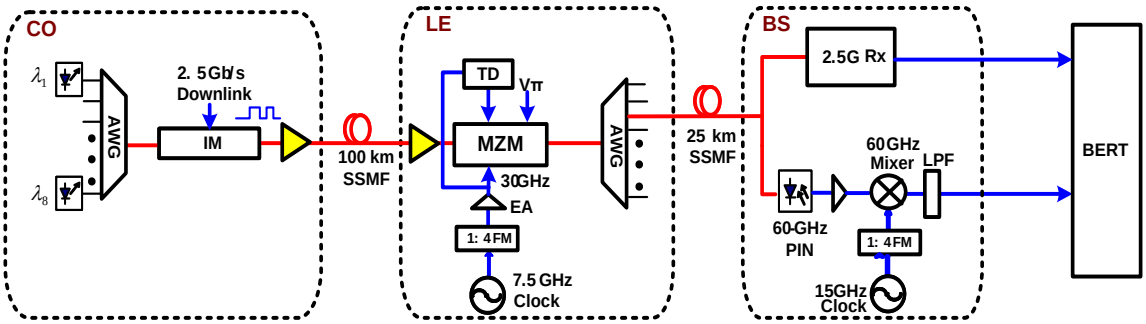

Figure 2.20. Experimental setup of the long-reach WDM 60-GHz RoF system.

After the up-conversion, one of eight channels is filtered with an AWG before transmitted over a 25-km SSMF to the BS. At the BS, the wired signals are directly detected by a compact 2.5-Gb/s receiver with 3R functions, which can remove the high-frequency signal (mmW). On the other hand, for the wireless transmission, the O/E conversion is completed by a 50-GHz PD. The electrical DL signal is amplified by an EA and then down-converted to the baseband form with the same components used in the setup of the first proposed method of optical mmW generation in Figure 2.7. The optical eye diagrams of mmW signals after the 100-km and 125-km SSMF transmission are

shown in Figure 2.21(a) and 2.21(b), respectively. It is seen that the eye diagram after the 125-km transmission has more distortion but still keeps clear and open. Figure 2.22 shows the measured BERs and corresponding eye diagrams for the wired and wireless data. At the given BER of 10^{-9}, the power penalties after the 125-km transmission are about 0.5 dB and 1.4 dB for the wired and wireless data, respectively. The penalties result from the impact of CD for the two sub-carriers with 60-GHz spacing.

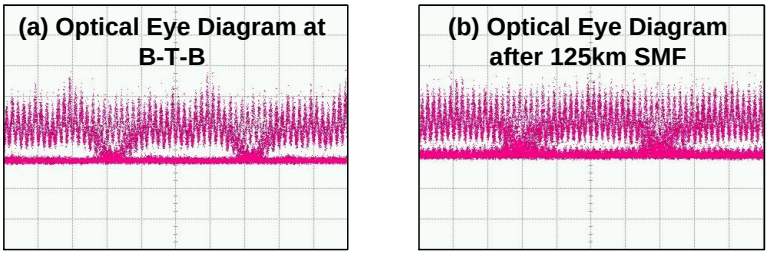

Figure 2.21. Measured optical eye diagrams of the 2.5 Gb/s data at 60 GHz after (a) the 100-km and (b) the 125-km SSMF transmission.

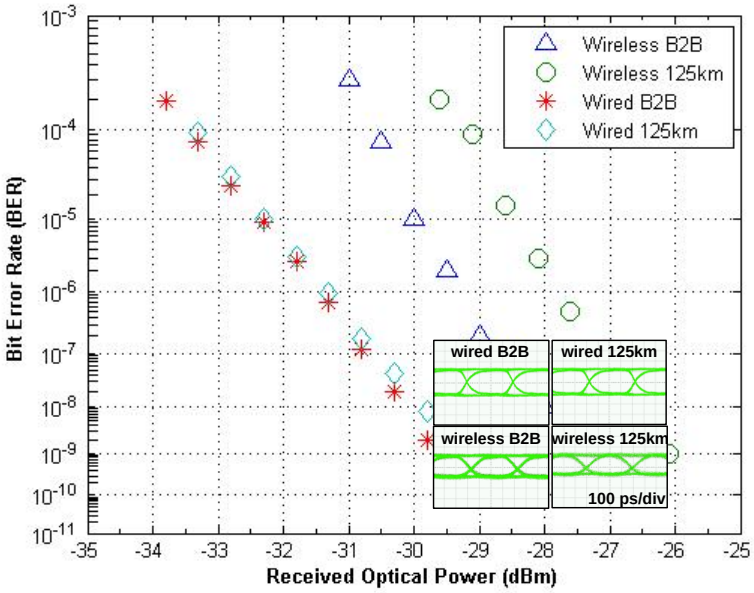

Figure 2.22. BER measurements of the wired and wireless transmission.

2.3.3 Backscattering Interference

Using one single fiber for both DL and UL transmissions, the system cost,

complexity and size of can be reduced. However, for such bi-directional optical systems, interference induced by backscattering light would be a serious impairment for transmission performance. The backscattering interference can be classified into Rayleigh, Brillouin, and Raman scattering light.

Rayleigh scattering results from elastic collisions between the light wave and the silica molecules, and its scattered radiation occurs in all directions uniformly. It accounts for about 96% of attenuation in optical fiber. The attenuation coefficient α_R due to Rayleigh scattering in (pure) fused silica is [66]

$$\alpha_R = 1.7(\frac{0.85}{\lambda})^4, \tag{2.14}$$

where the units for α_R and wavelength λ are dB/km and μm, respectively. For an optical signal with power of 0 dBm and wavelength of 1550 nm, the Rayleigh scattering power increases with fiber transmission distance as Figure 2.23. Some scattered light is reflected back toward the light source, which is main problem for the bi-directional optical system. We call it as Rayleigh backscattering.

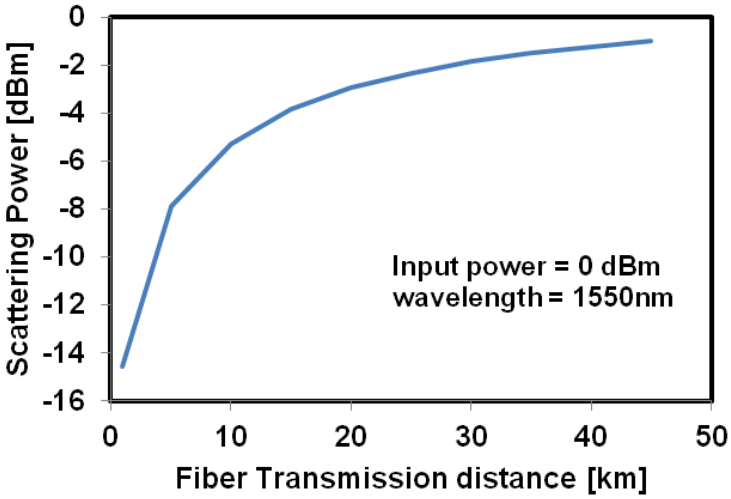

Figure 2.23. Rayleigh scattering power versus fiber transmission distance for an optical signal with power of 0 dBm and wavelength of 1550 nm.

For a bi-directional optical system, the Rayleigh backscattering can be divided into two types: Rayleigh carrier backscattering (CB) and Rayleigh signal backscattering (SB) as Figure 2.24 [67]. For a system with DL and UL using the same wavelength, the Rayleigh CB is unavoidable. Rayleigh SB is severe problem for a system with lightwave centralization, in which the carrier for UL transmission is from DL wavelength reuse or remote delivery as section 2.1 mentions. Recently, several methods have been proposed to mitigate the RB effects [68-72]. Among them, reference [72] can eliminate the Rayleigh CB and Rayleigh SB without additional light sources for UL transmission.

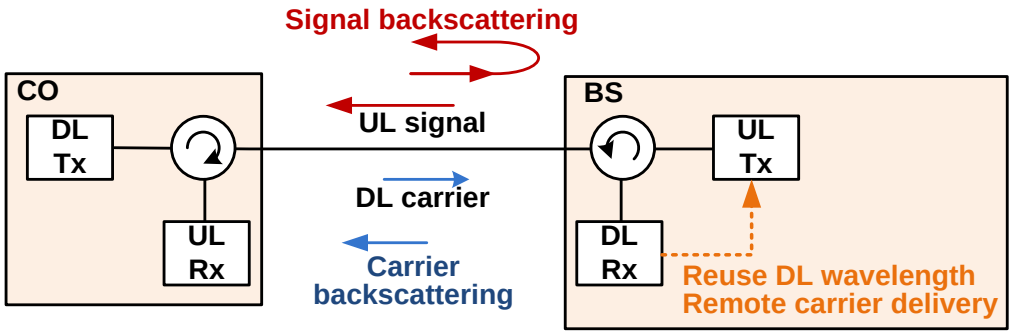

Figure 2.24. Two types for Rayleigh backscattering: signal backscattering and carrier backscattering.

Brillouin scattering is an effect caused by the $\chi 3$ nonlinearity of a medium. Through interaction with the acoustic wave, an incident photon can be converted into a scattered photon of slightly lower energy, usually propagating in the backward direction, and a phonon (vibrational energy) The frequency of the reflected light is downshifted by a given amount corresponding to the acoustic phonon frequency. This is called the Brillouin frequency shift, which is of the order of 10–20 GHz for silica fiber [73]. Spontaneous Brillouin scattering can occur even at low optical powers. When the input optical power achieve a certain threshold value, stimulated Brillouin scattering (SBS) can reflect most of the power of an incident beam. Some types of fiber are designed to have

higher threshold and then prevent the occurrence of SBS [74]. The interference from Brillouin scattering is significant for the system with different wavelengths (~tens GHz) assigned to DL and UL transmissions. It can be mitigated by controlling the power level lower than SBS threshold.

Because simulated Raman scattering (SRS) is up to 15 THz (125nm) apart from input optical signal [75], and SRS has much higher threshold than SBS, the transmission impairment induced by SRS is trivial and can be ignored in RoF systems.

2.4 Chapter Summary

In this chapter, we conclude the key functions and challenges for a mmW RoF system, which is composed of a CO, optical networks, and BSs. In order to reduce the cost and complexity of numerous BSs in mmW systems, optical approaches are used for mmW signal generation at the CO. We concludes the common generation methods with one and two lasers and then summarizes their advantages and disadvantages. Among them, the generation method based on external intensity or phase modulation is more flexible and practical to implementation; the OCS format achieved by an external MZM is theoretically proven with small occupied bandwidth and the benefit of frequency doubling. Moreover, two new schemes based on external phase modulation for optical mmW generation are presented; the experimental results suggest that these developed schemes with high stability and simple design will be the desirable candidates for future optical-wireless networks.

The transmission impairment induced by fiber chromatic dispersion is another focus of this chapter, which would limit the fiber transmission distance of a mmW RoF system. Based on the theoretical analysis, the use of OSSB+C, whose optical carrier is with high DC component, and ROCS technology can increase the fiber transmission distance. We experimentally demonstrate a ROCS RoF system with 8 x 2.5-Gb/s signals

at 60-GHz over 125-km SSMF without any dispersion compensation. Three sources of backscattering light are also introduced and analyzed for the bi-directional RoF system.

CHAPTER 3

ARCHITECTURE DESIGN FOR MULTI-BAND SYSTEM

The simultaneous multi-band signal generation based on the RoF technology can support a variety of wireless systems, regardless of their frequency bands, in a unified optical platform. It transfers the complicated multi-band signal processing functions to a centralized CO, which can make the system control and quality maintenance much easier. In this chapter, some multi-band architectures are presented, which are belonging to three different types. These include simultaneous generation of mmW with MW and baseband in section 3.2, mmW with commercial wireless technologies in low RF regions in section 3.3, and multiple 60-GHz sub-bands in section 3.4. Finally, all these proposed multi-band RoF systems are summarized in section 3.5.

3.1 Introduction

With the rapid growth of bandwidth demand for all kinds of emerging data and video-intensive wired and wireless services, converging traditional baseband systems (EPON and GPON) and wireless systems on the same optical platform based on RoF techniques is foreseen as a promising way to provide multi-band services. This is because the optical transport of radio signals based on RoF technology that can offer wireless services with an extended coverage that is beyond the purely RF range, and have format transparency to integrate multiple wireless services on an optical platform. Figure 3.1 shows the optical-access network architecture, which can simultaneously provide wired and wireless services. The service providers send the data to the CO, a RF/optical interface. Based on the RoF technology, the data are optically up-converted to different RF bands, including baseband, Wi-Fi, WiMAX, MW, mmW and so on. In the remote node, the up-converted multi-band signals with different wavelengths are multiplexed

and demultiplexed by AWGs before they are routed to access points (APs) over fiber. The APs then locally distribute wireless services to antennas for broadcasting, and wired services (baseband) to local area networks such as fiber-to-the-home (FTTH). The APs can be conference centers, airports, hotels, shopping malls, and ultimately homes and small offices.

In this chapter, some proposed architectures about the multi-band generations and transmissions will be discussed. These architectures can be divided into three types according to their generated bands as Figure 3.2 shows. The first type can generate and transmit mmW, MW, and baseband signals at the same time (Figure 3.2(a)), and the second one can simultaneously offer mmW and commercial wireless services at lower RF regions such as Wi-Fi and WiMAX (Figure 3.2(b)). Not like the previous two ones to view the whole 60-GHz as one band, the third type is capable of transmitting multiple services at 60-GHz sub-bands (Figure 3.2(c)).

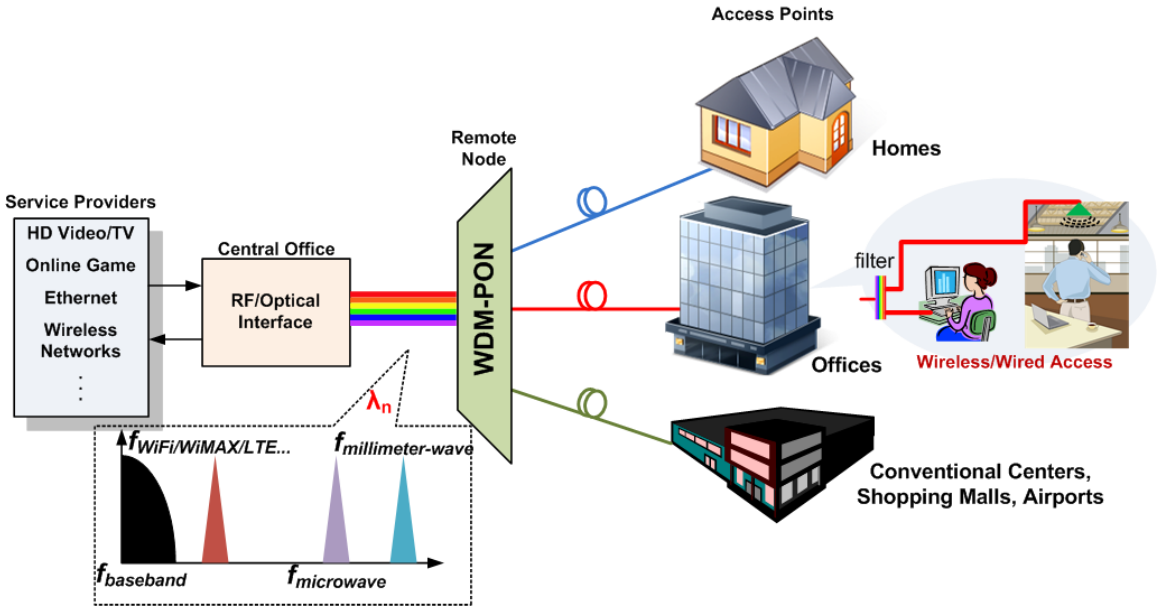

Figure 3.1. The optical-access network architecture for simultaneously providing wired and wireless services.

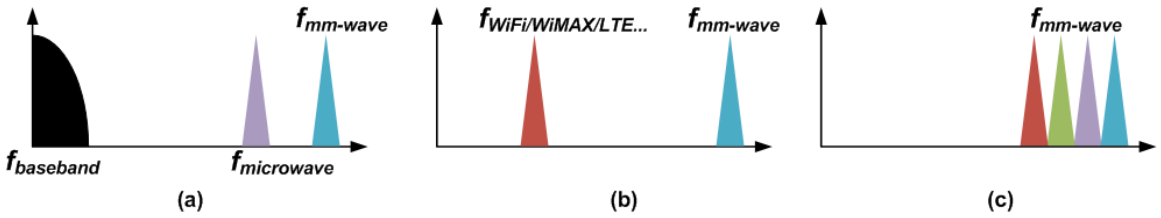

Figure 3.2. Three multi-band types: (a) baseband, MW, and mmW, (b) mmW and wireless services at lower RF regions, and (c) mmW (60 GHz) sub-bands.

3.2 Baseband, Microwave and Millimeter Wave

Recently, the RoF systems with simultaneous multi-band modulation and transmission, including baseband, MW, and mmW, have been demonstrated [76-78]. However, the multi-band signal generation in [76] is implemented with an expensive and complicated modulator, and the EAM nonlinearity, residual chirp and the crosstalk among three signals would limit the transmission performance in [77] and [78]. Additionally, these methods require high-frequency clock source to generate mmW signal. More importantly, the transmission limitation arising from optical fiber chromatic dispersion was not resolved yet for these multi-band systems. In this section, we propose a novel full-duplex RoF system transmitting downlink wireless 60-GHz mmW, 20-GHz MW, and wired baseband data [79]. It is based on a single dual-arm MZM and a subsequent optical filter (OF). The high dispersion tolerance is achieved by the OSSB+C format. The upstream data transmission is obtained by reusing the wavelength of downstream, therefore, there is no need of an additional light source and wavelength management at the BS, which significantly reduces the cost and increases the system stability.

Figure 3.3 shows the schematic diagram of the proposed multi-band RoF system. It is achieved by only one MZM. The CW, which is represented by $E_{in}=E_o\ exp(j\omega_c t)$, is modulated by two driving signals, $V_1(t)$ and $V_2(t)$, via a dual-arm MZM. $V_1(t)$, consisting of a baseband data mixed with a 40-GHz sinusoidal clock, can be written as $V_1(t)$ =

$A(t)\cos(\omega_1 t)$, where $A(t)$ represents the 2.5-Gb/s baseband data, and ω_1 is the angular frequency of the sinusoidal signal. $V_2(t)$, consisting of a 20-GHz RF sinusoidal clock and a DC bias voltage, is written as $V_2(t) = V_b + B\cos(\omega_2 t)$. Here V_b is the DC bias voltage, and B and ω_2 are the amplitude and the angular frequency of the 20-GHz sinusoidal signal. We assume the power splitting ratio of two arms of the MZM is 1/2.The electrical field at the output of the MZM is given by

$$E_{out} \approx \frac{\sqrt{\alpha}\cdot E_0}{2}\left[\left(J_0(m_A)+J_0(m_B)e^{j\pi V_b/V_\pi}\right)\cdot e^{j\omega_c t}+J_1(m_A)\cdot e^{j[(\omega_c+\omega_1)t+\pi/2]}\right.$$
$$+J_1(m_A)\cdot e^{j[(\omega_c-\omega_1)t+\pi/2]}+J_1(m_B)\cdot e^{j\pi V_b/V_\pi}\cdot e^{j[(\omega_c+\omega_2)t+\pi/2]}$$
$$\left.+J_1(m_B)\cdot e^{j\pi V_b/V_\pi}\cdot e^{j[(\omega_c-\omega_2)t+\pi/2]}\right]. \quad (3.1)$$

Here, α is the insertion loss of the MZM. Equation (3.1) shows that carrier and four subcarriers are equally spaced by 20 GHz, and two inner subcarriers are without any data information. After a fiber of length l, an OF is used to separate these subcarriers to generate 60-GHz and 20-GHz signals. As shown in Figure 3.3, the 60-GHz mmW and 20-GHz MW both belong to the optical OSSB+C scheme which has high tolerance to CD. The optical mmW and MW are detected by PDs, and their photocurrents are expressed as

$$I_{mm-wave}=\frac{\mu\alpha {E_0}^2}{4}\left\{{J_1}^2(m_A)+{J_1}^2(m_B)+2J_1(m_A)J_1(m_B)\cdot\cos\left[(\omega_1+\omega_2)t\right.\right.$$
$$\left.\left.-\beta'(\omega_c)(\omega_1+\omega_2)l+\frac{1}{2}\beta''(\omega_c)({\omega_1}^2-{\omega_2}^2)l+\pi V_b/V_\pi\right]\right\}, \text{ and} \quad (3.2)$$

$$I_{MW}=\frac{\mu\alpha {E_0}^2}{4}\{{J_1}^2(m_A)+{J_1}^2(m_B)+2J_1(m_A)J_1(m_B)\cdot\cos\left[(\omega_1-\omega_2)t\right.$$
$$\left.-\beta'(\omega_c)(\omega_1-\omega_2)l-\tfrac{1}{2}\beta''(\omega_c)({\omega_1}^2-{\omega_2}^2)l-\pi V_b/V_\pi\right]\}, \quad (3.3)$$

where the fiber loss is ignored, and μ is the responsivity of the PD. Furthermore, the propagation constant, $\beta(\omega_c+n\omega_m)$, is replaced with its Taylor's expansion (Equation (2.9)) and ignores higher-order fiber dispersion. Moreover, the carrier and the 1st-order subcarrier with lower frequency are remodulated by the upstream data, and then sent back to the CO where a low-speed receiver is utilized for the O/E conversion.

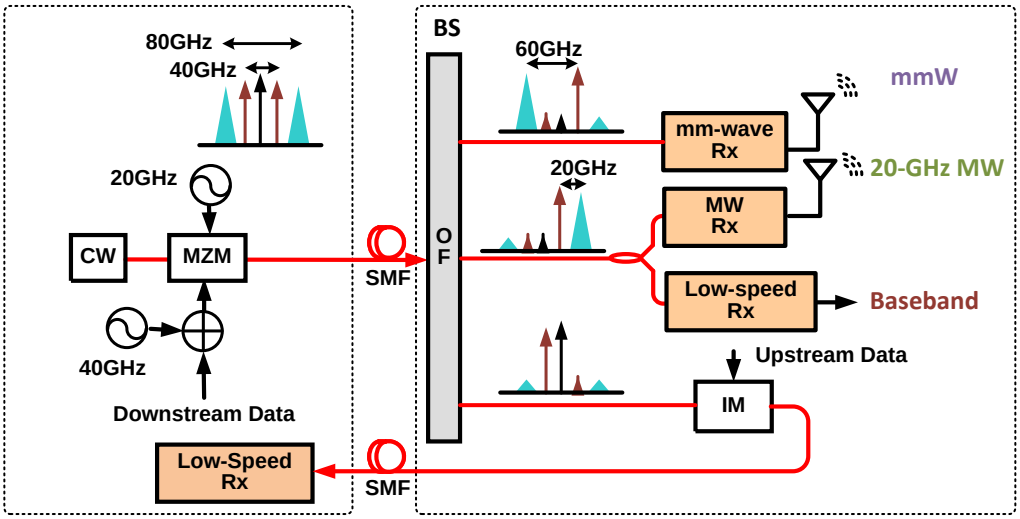

Figure 3.3. Schematic diagram of the multi-band generation (baseband, 20 GHz, and 60 GHz) based on a dual-arm MZM.

As shown in Figure 3.4 , the biased point of the MZM has a major impact on the reused carriers for the UL modulation. The larger the extinction ratio resulting from the DL data delivered by the carrier, the worse the UL performance. Oppositely, the mmW and MW downlink signals have very small variations with the bias point based on the above analysis. Therefore, for this scheme, the optimal bias point should be about $0.8V\pi$.

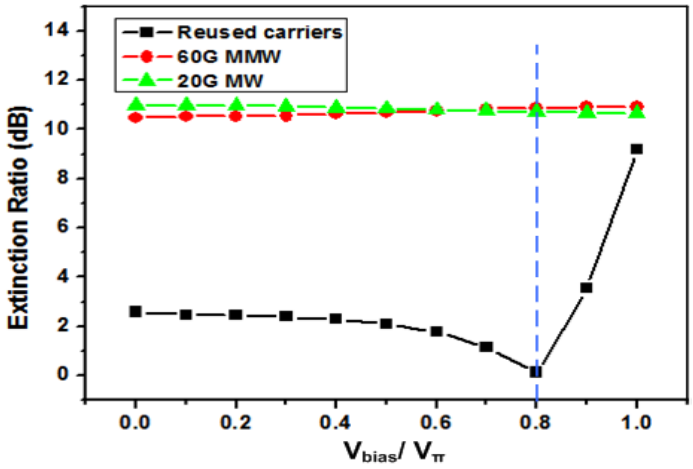

Figure 3.4. Extinction ratio of the reused carriers, 60-GHz mmW and 20-GHz MW versus DC bias voltage with V_{pp} of $V_1(t) = V\pi$ and $B = 0.2V\pi$.

Figure 3.5 illustrates the experimental setup for the proposed multi-band optical-wireless access system over fiber and air links. At its CO, a CW lightwave is generated by a tunable laser at 1551.054 nm and followed by a LiNbO3 dual-arm MZM. One arm is driven by an amplified 20-GHz sinusoidal wave. The 2.5-Gb/s data with PRBS word length of 2^{31}-1 mixed with a 40-GHz sinusoidal RF source, which is generated by 1:4 FM and 10-GHz clock source, is used to drive the other arm of the modulator. The driving amplitude (*Vpp*) of the mixed signal is 6.1 V, and the half-wave voltage ($V\pi$) of this MZM is 4.4 V. An EDFA is used to compensate the insertion loss from the modulator and obtain 3-dBm power before transmitting over 50-km SMF-28 to the BS.

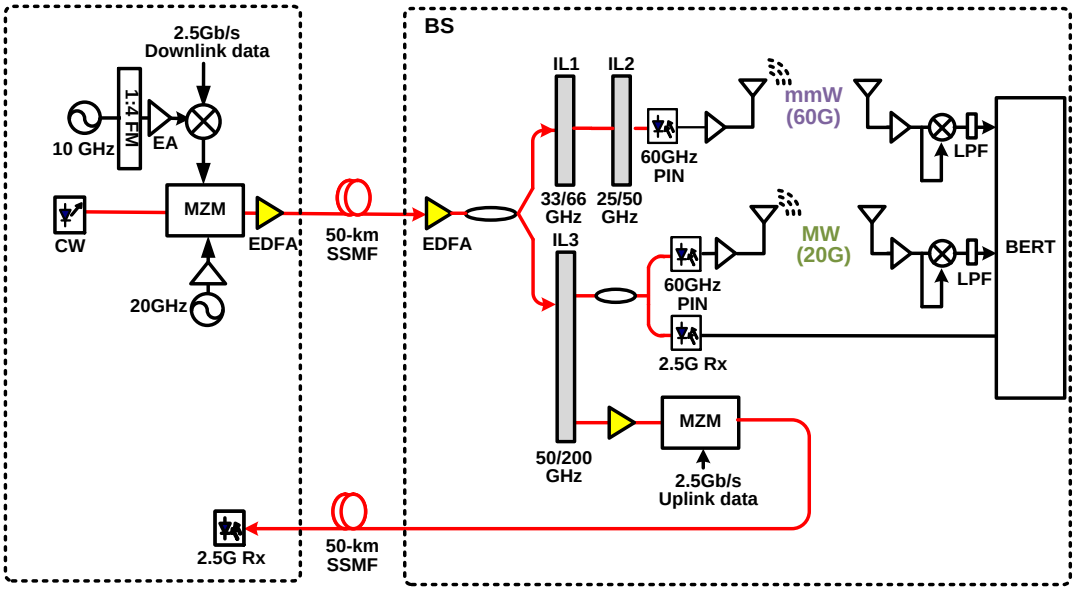

Figure 3.5. Experimental setup of the full-duplex RoF system with a 60-GHz mmW, a 20-GHz MW, and a baseband signal base on a dual-arm MZM.

At the BS, the multi-band signals are first divided into two parts by an optical splitter. Next, an optical filter, which is achieved by cascading a 25/50- and 33/66-GHz optical interleavers (IL1 and IL2) with 200-GHz periodicity and >30-dB channel isolation, is used to get the 60-GHz mmW signal from one part of the multi-band signals; the optical spectra of the filter window and the filtered signals are shown in Figure 3.6. The inset of Figure 3.6(b) is the BTB optical eye diagram of 60-GHz signal. The optical spectra of the 20-GHz MW signal and uplink carriers separated by a 50/200-GHz interleaver (IL3) are shown in Figure 3.7 insets (a) and (b). The O/E conversion and RF signal broadcast are completed with the same components for the first proposed method of optical mmW generation shown in Figure 2.7.

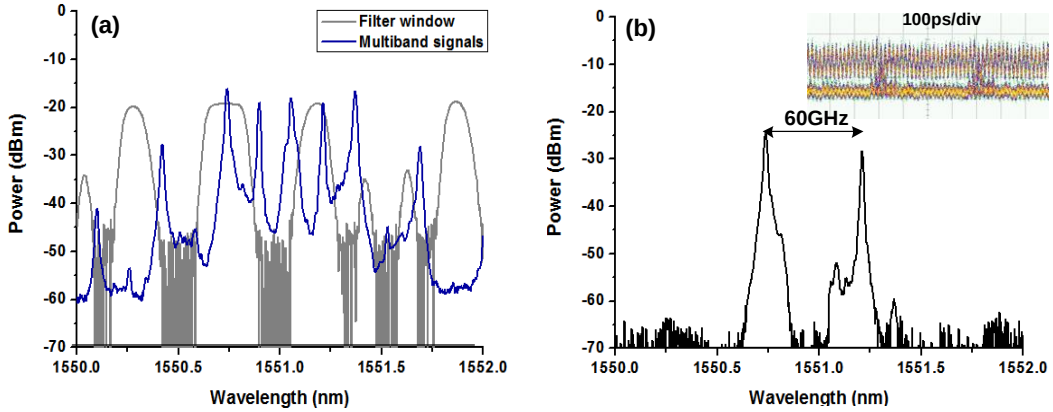

Figure 3.6. (a) Optical spectra of filter window, and (b) 60-GHz mmW signal with its optical eye diagram (resolution: 0.01 nm).

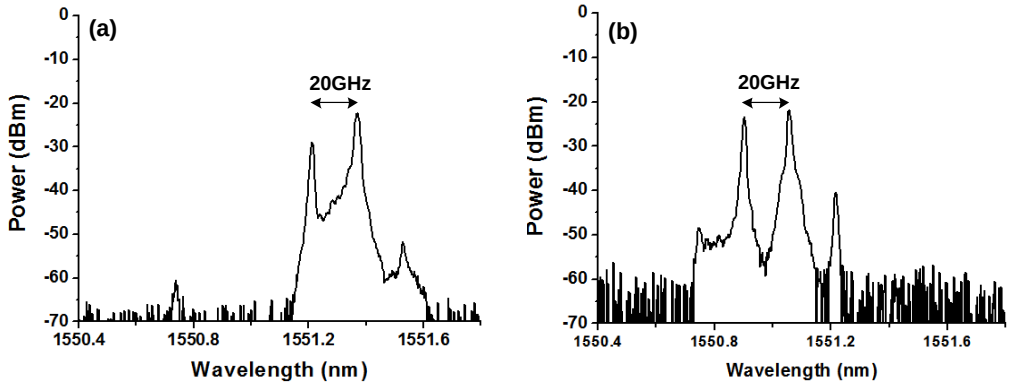

Figure 3.7 (a) Optical spectra of two ports of IL3: 20-GHz microwave signal, and (b) uplink carriers (resolution: 0.01 nm).

After the received antenna, the down-conversion is achieved by self-mixing method through a balanced mixer without requiring any local oscillator signal. For the wireline baseband data, we utilize a 2.5-Gb/s receiver with 3R function to directly detect the 20-GHz MW signal from the port 1 of IL3. The down-conversion of 20-GHz MW signal is not implemented on account of the absence of the 20-GHz mixer, antennas and low noise EAs. For the uplink, the signal from the port 2 of IL3 is remodulated by a symmetric 2.5-Gb/s PRBS 2^{31}-1 data after amplified by an EDFA, and then transmitted over 50-km SMF-28. The uplink signal is detected by a low-speed receiver which also filters out the residual part of the 20-GHz MW signal. In order to assure good

performance for downlinks and uplink, the minimum out-of–band rejection completed by ILs is about 20-dB.

The BER measurements for the DL wired signal and the DL 60-GHz signal with a 4-m wireless transmission are shown in Figure 3.8. The receiver sensitivity is relatively high because an optical pre-amplifier is utilized. At the given BER of 10^{-9}, the power penalties after a 50-km SMF-28 transmission are about 0.3 dB and 1.4 dB for the wired and wireless services, respectively. The penalty for the wireless transmission is mainly due to the amplified spontaneous emission (ASE) from EDFA and the noise from EAs at the BS. The BERs for the 2.5-Gb/s remodulated UL are also shown in Figure 3.8, and its power penalty is less than 0.5 dB over the same transmission distance. The electrical eye diagrams after the 50-km SSMF transmission for the DL and UL signals are also provided in the insets of Figure 3.8.

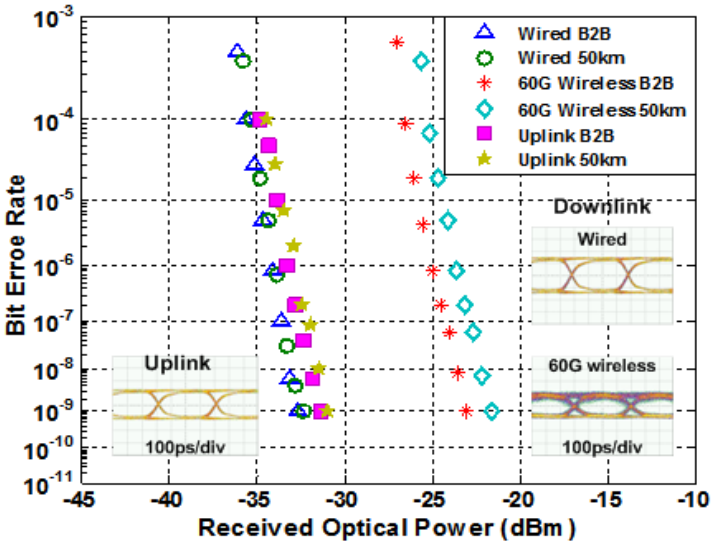

Figure 3.8. BER measurements and electrical eye diagrams for the uplink and downlinks of the wired and 60-GHz signal with a 4-m wireless transmission.

The unique advantages of this multi-band RoF system are to utilize simple components to realize dispersion-tolerant transmission and without the lasers in the BS

for the uplink transmission. The experimental results prove that the proposed scheme is suitable to simultaneously offer high bandwidth, multi-services for the future optical access networks.

3.3 Millimeter Wave with Wireless Services in Low RF Regions

As discussed in Chapter 1, optical-wireless access technologies have been considered the most practical and efficient solution to increase the capacity, coverage, bandwidth, and mobility for the last mile and last meter. Various RoF systems with commercial wireless services at lower RF regions (ex. Wi-Fi at 2.4 GHz and WiMAX at 5.8 GHz) that deliver multi-megabit signal over in-building fiber network have been proposed and demonstrated [80-82]. On the other hand, the RoF system architecture operating at 60-GHz has recently gained much attention for its availability to achieve multi-gigabit data rate. In order to exploit such bandwidth advantage of 60-GHz mmW and have the backward compatibility of legacy wireless services, in this section, we focus on the RoF architecture design that accommodates advanced mmW and former RF services simultaneously for in-building broadband access systems.

Here, two architectures for the integration of mmW optical-wireless systems with commercial BWA technologies are presented [83, 84]. Both schemes are based on multi-carriers generation with a PM and a MZM, respectively, and can cost-efficiently achieve the long-reach delivery for commercial wireless services and ultra-high bandwidth provision. Furthermore, these schemes have the capability of imposing independent wireless services on different bands.

3.3.1 60 GHz MmW with 2.4 GHz Wi-Fi and 5.8 GHz WiMAX

In Figure 3.9, the first scheme based on a PM and subsequent filtering can simultaneously provide Wi-Fi, WiMAX, and 60-GHz mmW services. The multiple sidebands are generated by a PM, which is driven by a 30-GHz clock source. The

different subcarriers, which are separated by an OF, are modulated by different baseband data from Wi-Fi, WiMAX and mmW services, respectively. After transmitting over a length of fiber, the combined signal is separated by the other OF. The baseband data for Wi-Fi and WiMAX services are up-converted to their belonging frequency bands by using the commercial transceivers, and then broadcasted to users. The 60-GHz optical signal are converted to the electrical domain and also broadcasted by an antenna. Therefore, all-optical up-conversion in the CO is for the high-data-rate 60-GHz signal while the remote electrical up-conversion in the BS for Wi-Fi and WiMAX services. The wired service can also be achieved by using a low-speed receiver to accomplish direct detection as Figure 3.9 shows.

Of course, if the input signals for Wi-Fi and WiMAX services from service provider are already at thier corresponding RF bands, the IMs can be directly modulated by these RF signals. At this situation, the Wi-Fi and WiMAX transceivers are unnecessary.

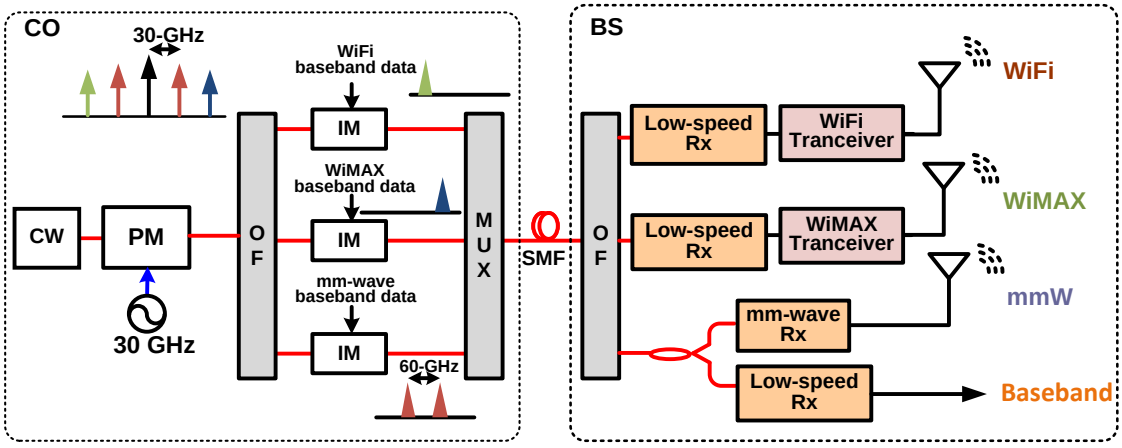

Figure 3.9. Schematic diagram of a multi-band RoF system with mmW, Wi-Fi and WiMAX.

Figure 3.10 illustrates the experimental setup for the proposed multi-band RoF system. At the CO, a CW lightwave at 1554.34 nm is followed by a PM driven by a 30-

GHz sinusoidal wave. The output of the PM can be written as a combination of various sidebands as Equation (2.4). How many sidebands can be generated depends on the amplitude of the driven RF signal on the PM. Here, we assume that the first- and 2nd-order sidebands are generated through optimization of the modulation depth. The removal of the carrier and unwanted high-order sidebands is achieved by the 50/100-GHz optical IL1 as shown in Figure 3.11(a), and then the 50/200-GHz IL2 is utilized to separate the remaining four subcarreirs. The optical spectrum of the signal after the 50/100-GHz IL1 and transmission windows for four ports of the 50/200 IL2 are shown in Figure 3.11(b). The 2nd-order sidebands are viewed as two carriers, which are modulated by a 250-Mb/s and a 1-Gb/s baseband data for the Wi-Fi and WiMAX transmissions, respectively. The mmW is generated by using a coupler to combine the two 1st-order sidebands with a frequency spacing of 60 GHz and then modulated by a 2.5-Gb/s PRBS data with a word length of 2^{31}-1. After sent to an equalizer, whose function is to adjust the power of three signals with either three optical attenuators or three tunable EDFAs, the two baseband signals and one 60-GHz mmW signal are coupled by a MUX and then amplified by an EDFA to obtain 12-dBm power before transmitting over a 25-km SSMF to the BS.

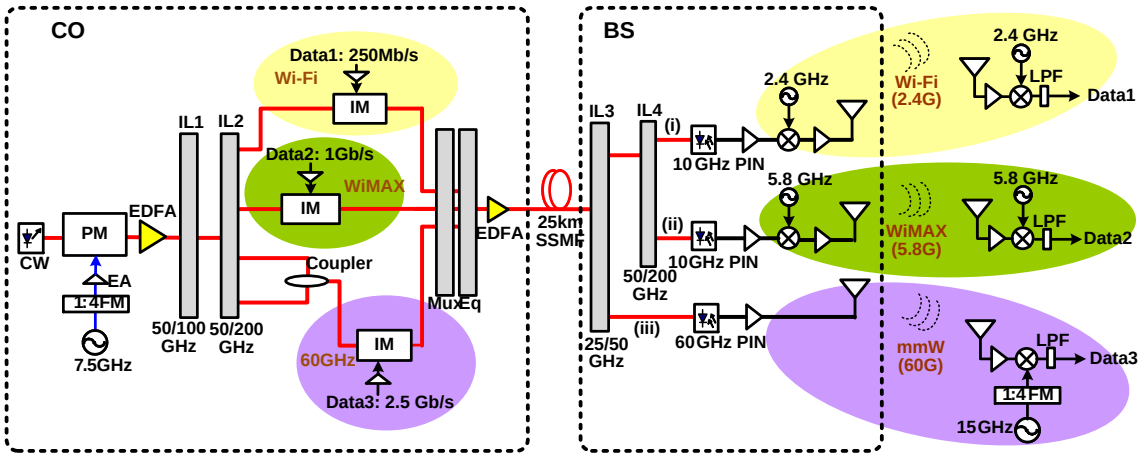

Figure 3.10. Experimental setup of the RoF system with Wi-Fi, WiMAX and mmW services based on a PM and subsequent filtering.

At the BS, three different signals are separated by cascading two optical ILs (IL3 and IL4) with 25/50- and 50/200-GHz channel spacing, respectively. As shown in Figure 3.11(c), the 60-GHz mmW signal passes through the odd port of the 25/50-GHz IL3. Figure 3.12 shows the optical spectra of the three separated multi-band signals at the BS. The components for the O/E conversion, wireless transmission, and down-conversion of the 60-GHz signal are the same with the setup in Figure 2.7. The other two signals for Wi-Fi and WiMAX transmission are divided by the OF formed by the even port of the 25/50-GHz IL3 with the port 2 and port 3 of the 50/200-GHz IL4. However, if the 25/50-GHz IL3 is replace with a 33/66-GHz optical filter, their performance will be better because the filtering window matches the two baseband signals as shown in Figure 3.11(c). The two signals are then sent to the 10-Gb/s PDs and electrically up-converted to 2.4-GHz and 5.8-GHz band to emulate the function of Wi-Fi and WiMAX transceivers. After broadcasted by a 2.4-GHz panel antenna having 10 dBi gain and a 5.8-GHz parabolic dish antenna having 29 dBi gain, the Wi-Fi and WiMAX signals are received by the corresponding antennas and then down-converted baseband forms through electrical mixers, and a 2.4- and a 5.8-GHz electrical LO signal, respectively.

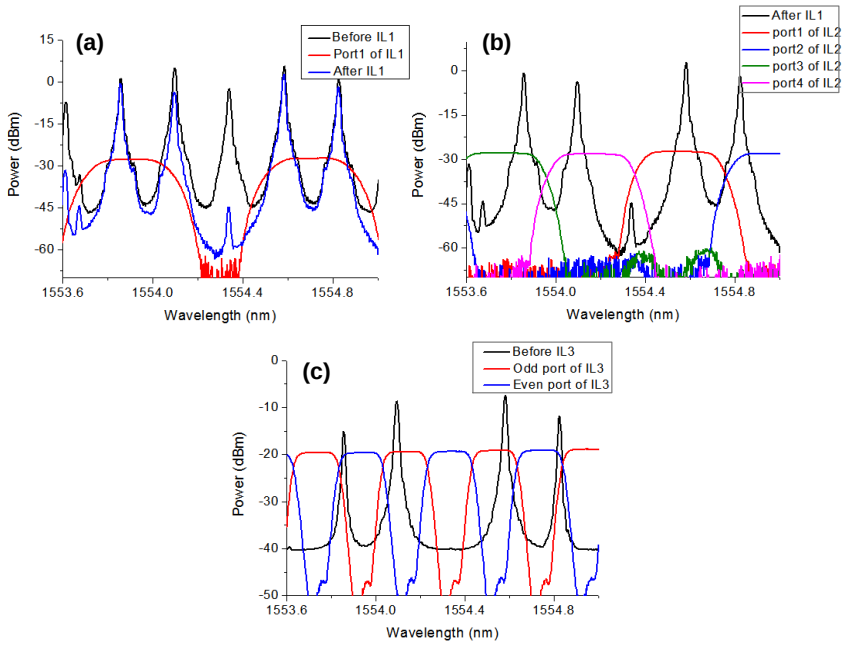

Figure 3.11. Optical spectra for the modulated and filtered signals (resolution: 0.01 nm).

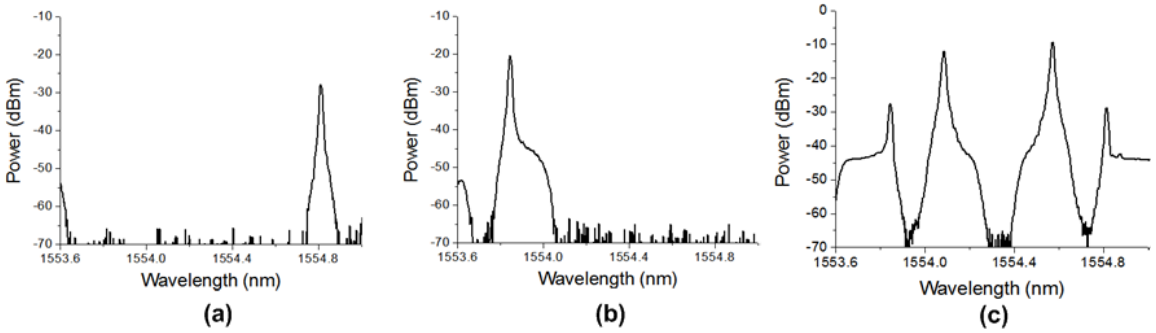

Figure 3.12. Optical spectra measured at point (i), (ii), and (iii) in Figure 3.10: (a) 2.4-GHz RF signal. (b) 5.8-GHz RF signal. (c) 60-GHz mmW signal (resolution: 0.01 nm).

The receiver sensitivities and electrical eye diagrams for the 2.5-Gb/s signal at 60 GHz with different wireless distances are shown in Figure 3.13(a). After transmitting over a 25-km SSMF, the power penalties at the given BER of 10^{-9} for different air distances are less than 1.5 dB. The penalties result from the CD for the two sub-carriers with 60-GHz spacing and the nonlinear modulation in the modulator. Moreover, Figure 3.13(a) also shows that the receiver sensitivities degrade with the increase of the air distance because the power loss is proportional to transmission distance. The BERs and corresponding electrical eye diagrams for the 250-Mb/s and 1-Gb/s signal at the air distance of 4-m are shown in Figure 3.13(b). After a 25-km SSMF, for these two signals, there are almost no power penalties as the CD effects are negligible at these rates. The distance of wireless transmission in the experiment is limited by our lab's space, and our scheme mainly focuses on the functional verification of the multi-services generation and transmission with only one light source at the CO. To our knowledge, this is the first experimental demonstration for simultaneously feeding three independent wireless signals on a single wavelength to provide last mile and last meter wireless access services.

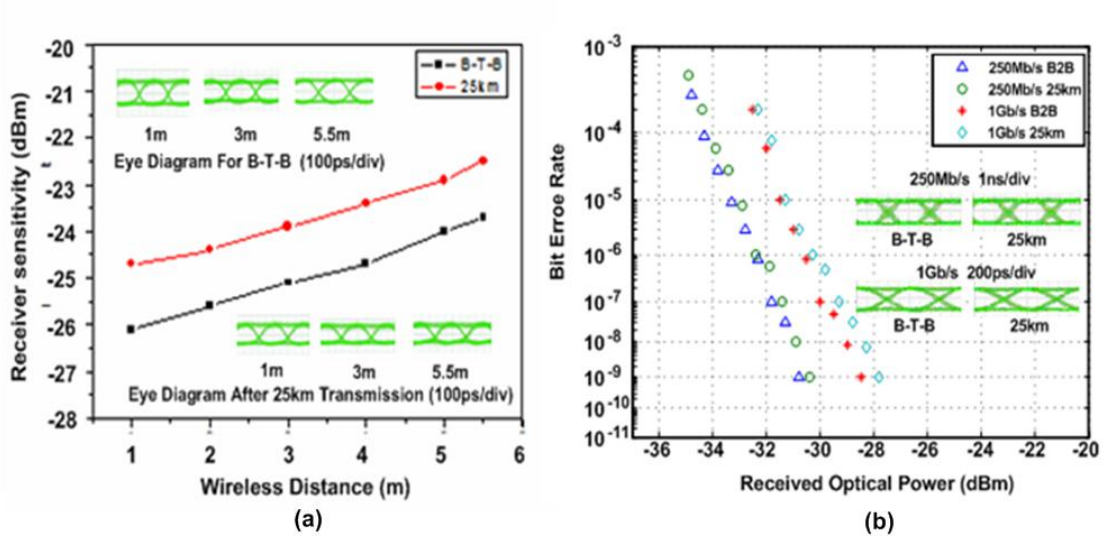

Figure 3.13. (a) Receiver sensitivities and electrical eye diagrams for the 2.5-Gb/s signal with different wireless distances. (b) BER measurements and electrical eye diagrams for the 250-Mb/s and 1-Gb/s signal after transmitted over a 25-km SSMF and 4-m wireless transmission.

3.3.2 Bidirectional OFDM-Based Baseband, MmW, and WiMAX Transmission

The second proposed scheme is based on the multi-carriers generation by a dual-arm MZM. It can simultaneously provide the bidirectional multiple orthogonal frequency-division multiplexing (OFDM)-based services including a mmW signal, a wired signal, and a wireless signal at low RF such as Wi-Fi, WiMAX, Long Term Evolution (LTE). For all of previously proposed RoF schemes, only binary OOK modulation format is used, which is the simplest and easiest modulation format. However, for wireless applications, OFDM, with high spectrum efficiency and robust dispersion tolerance, has been widely used in the commercial BWA techniques and considered as a strong candidate for future long-haul and access networks [85]. So, the successful implementation of a cost-effective and super-broadband wireless access network can be achieved by integrating OFDM and RoF techniques.

In our design, Figure 3.14, the function block of CO generates DL signals and detect UL data. With a dual-arm MZM, the optical carrier is modulated by the wireless

DL at a low RF (ex. WiMAX), from its BS, and the multiple sidebands are simultaneously generated by a LO signal with a frequency of f_1. An OF is used to separate two 2nd-order sidebands from other carriers for the mmW/wired DL modulation. If the data of mmW service is both with amplitude and phase information, which is called vector signal, the mmW baseband data has to be converted IF band [46] by electrical circuits, where the IF is usually much lower than mmW frequency.

After fiber transmission, the DL carriers in BS with mmW/wired signal and WiMAX are converted to electrical domain by direct detections. Meanwhile, two 1st-order sidebands without DL data are employed for UL modulations; it is lightwave centralization with remote carrier delivery. Therefore, no additional light sources and wavelength management function are required at the BS, which significantly reduces cost and improves system stability. Furthermore, the successful bidirectional transmission over a single fiber span is achieved by the mitigation of Rayleigh backscattering (RB), especially Rayleigh CB [67], which is because different frequencies are assigned for DLs and ULs.

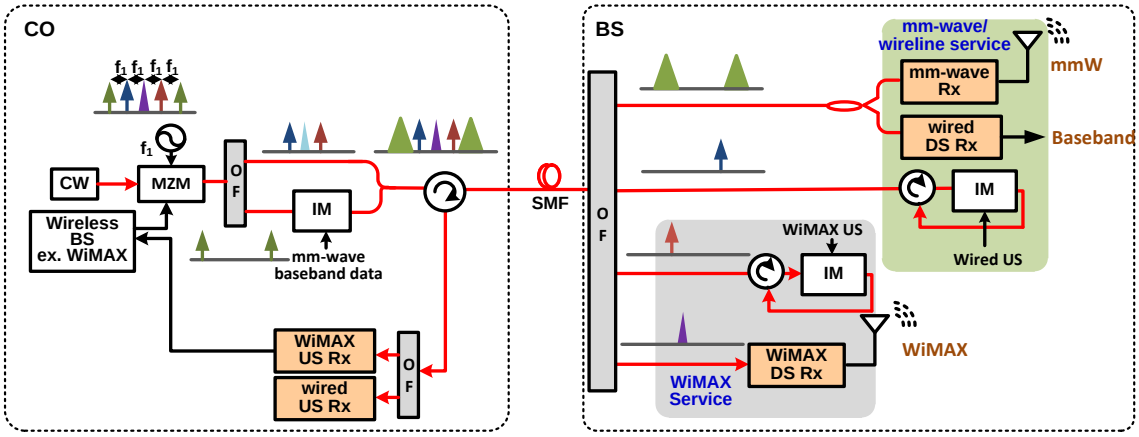

Figure 3. 14. Schematic diagrams of the bidirectional multi-band RoF system with baseband, mmW and wireless service at low RF region.

Figure 3.15 illustrates the experimental setup of the proposed bidirectional access network with multi-band services. At the CO, a CW lightwave at 1551.15 nm is followed

by a dual-arm MZM, which is driven by an amplified 17-GHz clock source and WiMAX DL signal simultaneously. The 17.28-Mb/s OFDM-64QAM WiMAX DL signal, with the center frequency of 2.66 GHz, a bandwidth of 10 MHz, FFT size of 1024, oversampling rate of 28/25, subchannel spacing of 10.9375 kHz and guard period of 1/8, is synthesized by software (Agilent signal studio for 802.16 WiMAX) and generated by a vector signal generator (Agilent N5182A). After the MZM, multi-carriers with spacing of 17 GHz is generated as shown in Figure 3.15(i), and it can be seen that only the central signal is carried by a 17.28-Mb/s WiMAX data; other sub-carriers, including the 1st- and 2nd-order sidebands, are CW lightwaves. After amplification, two optical ILs (50/100-GHz IL_1 and 25/50-GHz IL_2) are used to separate the 2nd-order sidebands from other carriers as shown in Figure 3.15(ii). The 2nd-order sidebands are considered as carriers for the 11.29-Gb/s wired DL OFDM signal with Hermitian symmetry, which is generated offline by MATLAB and uploaded into a Tektronix arbitrary waveform generator operating at 8 GS/s. In this experiment, we only demonstrate the wired transmission and detection because of the limitation of equipments, and just the optical eye diagram of 68-GHz mmW signal is displayed in Figure 3.15(v). Of course, a 68-GHz optical mmW can be realized with DL OFDM signal at IF, which can reserve phase and amplitude information. For the wired DL and UL, 16QAM and quadrature phase shift keying (QPSK) modulation formats are used for baseband symbol mapping. The FFT size is 128, where 96 subcarriers are mapped with random bit sequence (RBS) stream, 27 subcarriers for guard channels, and one subcarrier in the middle of the OFDM spectrum is set to zero for the DC in baseband. The cyclic prefix (CP) with length of 8 samples has been applied to resist CD. Four training sequences are added every 100 OFDM data frames.

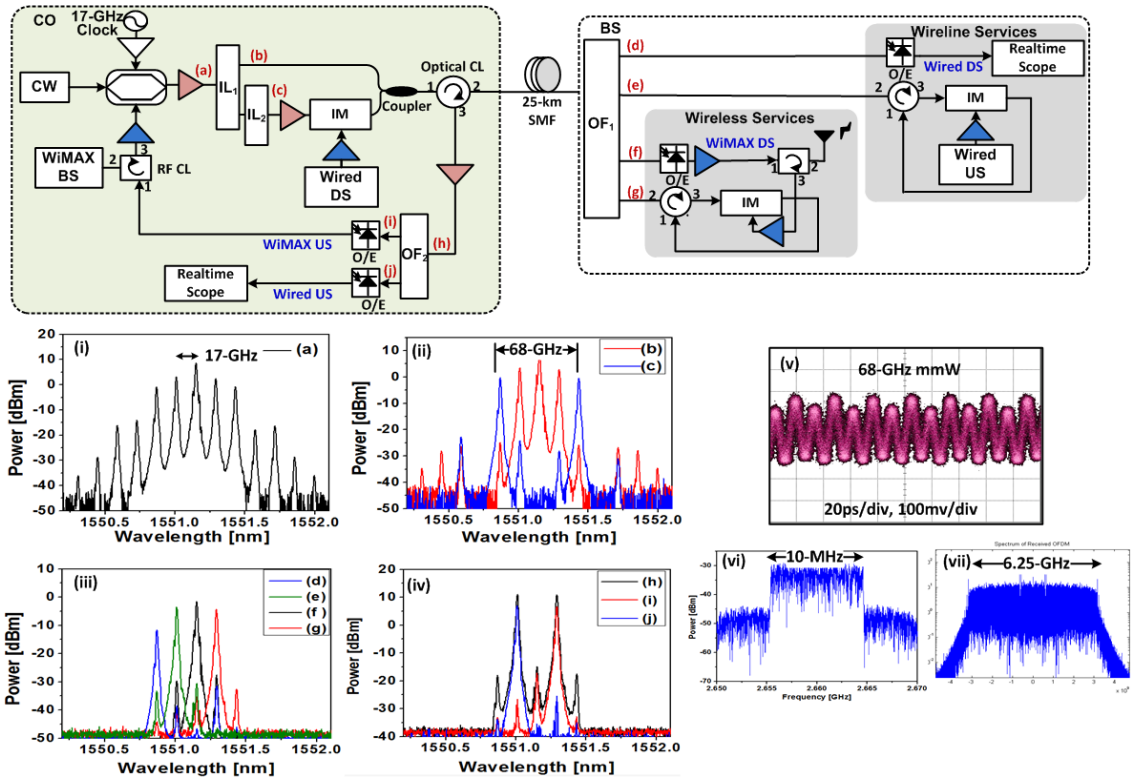

Figure 3.15. Experimental setup of the bidirectional OFDM-based RoF system with baseband and WiMAX service. Insets (i)-(iv): the optical spectra of their corresponding measured points (a)-(j) (0.01-nm resolution). Inset (v): optical eye diagram for the mmW signal. Insets (vi)-(vii): electrical spectra of the received WiMAX and Wired DS.

In the BS, four different signals are separated by OF_1, formed by a wavelength selective switch (WSS), as exhibited in Figure 3.15(iii). For the WiMAX DL carried by the central carrier, a 5-GHz PIN PD is used, and then the detected signal is analyzed by an Agilent N9020A signal analyzer. Furthermore, the O/E-converted wired DL signal is sent to a realtime scope for the offline processing. The electrical spectra of the received WiMAX and wired DLs are shown in Figure 3.15(vi) and (vii). For ULs, two 1st-order CW sidebands are employed for 11.52-Mb/s OFDM-16QAM WiMAX and 5.65-Gb/s OFDM-QPSK wired US modulations, respectively. By using the optical circulators (CLs), the two UL signals are sent back to the CO over the same fiber span and then separated by the OF_2 with a 3-dB bandwidth of 0.1 nm, which is also used to filter out the back reflection from the carriers with DL data as shown in Figure 3.15(iv).

The error vector magnitude (EVM) measurements for WiMAX DL and UL at different RF power are illustrated in Figure 3.16(a) and 3.16(b). According to the IEEE 802.16e standard [86], the EVM thresholds are 3.1% and 6% for the successful WiMAX communication with OFDM-64QAM and 16QAM modulation formats, respectively. The experimental results show that the EVM measurements of over a 25-km SMF-28 with RF power from -60 to -20 dBm are always under the thresholds of WiMAX. The clear constellations before and after the fiber transmission for both WiMAX DL and UL are inserted in Figure 3.16.

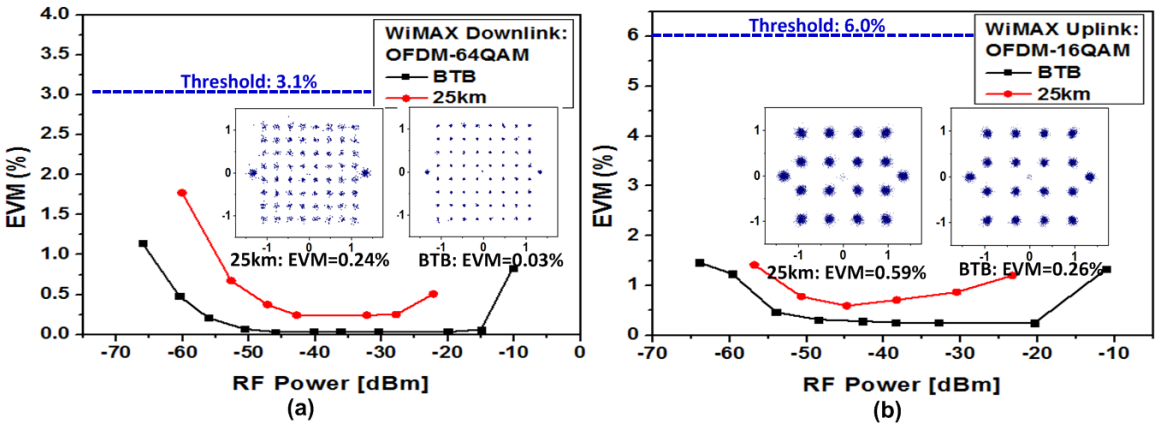

Figure 3.16. EVM versus RF power for the WiMAX(a) downlink and (b) uplink.

Figure 3.17(a) shows the BER versus received optical power for wired DL and UL. The power penalties caused by the 25-km SMF-28 are less than 0.5 dB for both transmissions. The constellations of the OFDM-16QAM and OFDM-QPSK are also shown in Figure 3.17(a). To show the real WiMAX traffic, we also demonstrate a successful back-to-back transmission by utilizing a real WiMAX BS (NEC PasoWings), a 2.5G omni-directional antenna having 3 dBi gain, and a laptop with a PCMCIA WiMAX transceiver as the mobile subscribers (MS). The WiMAX DL and UL are 9-Mb/s OFDM-64QAM and 4-Mb/s OFDM-16QAM signals with 28/25 oversampling factor at 2.66 GHz. Figure 3.17(b) shows the throughputs with different antenna input

power for the WiMAX DL and UL, exhibiting the RF operating range is 20 dB. The constellation for the DL signal with EVM = -32.33 dB and throughput = 9.18 Mb/s is also shown in Figure 3.17(b) as inset. The unique advantage of this scheme is to utilize simple design to realize successful multi-band bidirectional transmission with low RB interference and without additional light sources for USs.

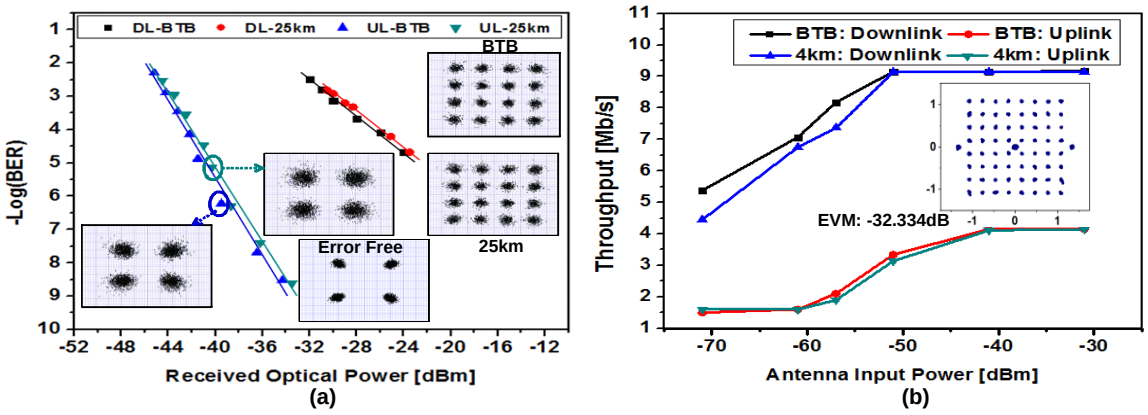

Figure 3.17. (a) BER versus received optical power for the wired DL and UL. (b) Throughput versus antenna input power for the BTB WiMAX DL and UL employing a commercial WiMAX BS from NEC PasoWings.

3.4 60-GHz Sub-bands Generation

The wide 60-GHz unlicensed band can be divided into several sub-bands to increase system flexibility. As mentioned in ECMA-387 [13], the unlicensed 8-GHz band is actually divided into four sub-bands centered at 58.32 GHz, 60.48 GHz, 62.64 GHz and 64.80 GHz with a frequency separation of 2.160 GHz and the symbol rate of 1.728 GS/s on each channel to lower the bandwidth requirement of mmW circuits and devices (Figure 3.18(a)). To address the generation and transmission issues of a converged optical-wireless network with multiple 60-GHz sub-bands, reference [87] based on the ODSB technique generates 60-GHz and 64-GHz mmW signals simultaneously but with an unwanted signal at 62 GHz produced and short distance of fiber transmission. Thus, a

novel RoF systems based on the OSSB+C format and cascaded modulation is proposed, which is with high tolerance to CD and without unwanted RF signals. Furthermore, a converged all-band 60-GHz RoF technology achieved by mapping multiple wireless signals to 60-GHz sub-bands can integrate VHT applications and former wireless services in one optical system.

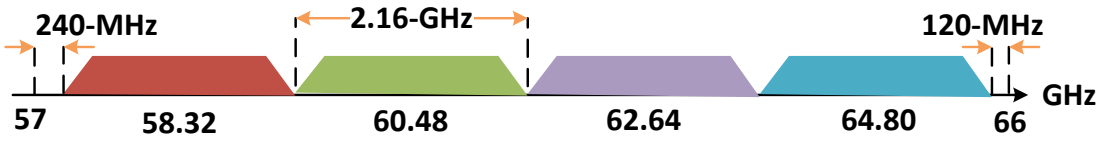

Figure 3.18. ECMA 387: 60-GHz mmW band channel allocation.

3.4.1 VHT Applications at Multiple 60-GHz Sub-bands

As shown in Figure 3.19, in the proposed scheme, the optical carrier with angular frequency ω_c is first modulated by two independent data at different RF signals (ω_{A1} = 36π GHz and ω_{A2} = 40.32π GHz) via a MZM. An OF_1 with a sharp passband window is used for vestigial sideband (VSB) filtering. The frequency of a RF clock, ω_B, is set at 40.32π GHz to further generate higher and lower subcarriers. Another optical filter (OF_2) is used to eliminate unwanted peaks. The remaining three subcarriers of interest, the left one without data and the right twos with different data information, are employed for the system demonstration. The coherent beating between the resultant optical subcarriers ω_1 (= ω_c - ω_B) and ω_2 (=ω_c +ω_{A1} + ω_B) and the beating between ω_1 and ω_3 (=ω_c +ω_{A2} + ω_B) would produce two mmW signals: one is at 50.32 GHz, and the other one is at 60.48 GHz. It can be seen if ω_A is equal to ω_B, one generated signal at frequency ω_A+2ω_B (= 3ω_B) to form exact frequency tripling. However, if ω_B is larger than ω_A by few GHz, it is approximate frequency tripling. The frequency tripling technique for the mmW generation makes these systems cost-efficient, which is with low bandwidth requirement

for electronic components comparing with the traditional mmW RoF systems using frequency doubling technique with the OCS format.

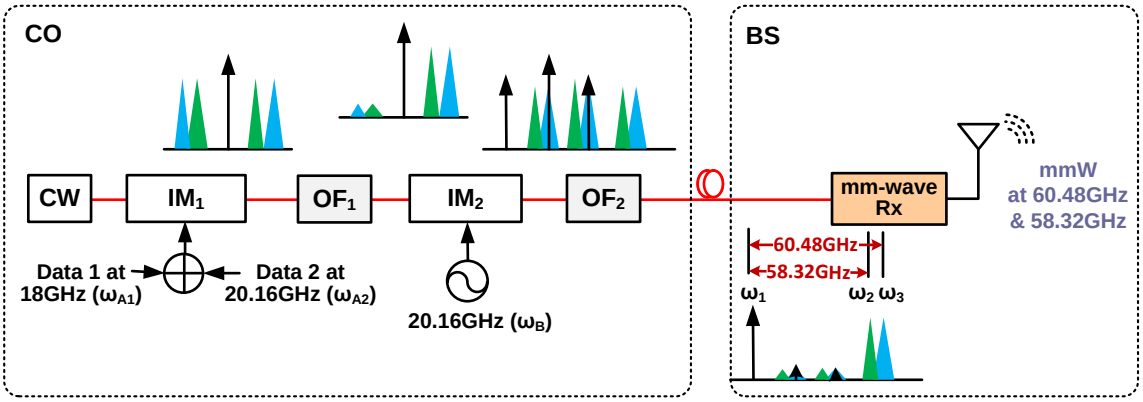

Figure 3.19. Schematic diagram of the RoF scheme based on cascaded modulation for the generation of multiple 60-GHz sub-bands.

At the BS, the optical signal is detected by a high-speed receiver and broadcasted by a 60-GHz mmW broadband antenna, and finally, the end users can select the appropriate band based on their need from the broadcasted multi-band signals. Based on this proposed scheme, we have experimentally demonstrated the generation and transmission of two independent 1-Gb/s data on 55-GHz and 60-GHz carriers over a 50-km SMF-28 without any dispersion compensation. The reason why we chose two bands over the four ones in ECMA-387 is the limitation of our available components and equipments.

The experimental setup is shown in Figure 3.20. At the CO, a CW at 1552.27 nm is modulated by a dual-arm MZM. Two 1-Gb/s data signals with a PRBS word length 2^{31}-1 are respectively mixed with a 15-GHz and a 20-GHz sinusoidal wave, which is generated by a frequency doubler, to realize the SCM and then used to drive the two electrodes of the MZM. The optical spectra after the MZM_1 and the OF_1, which is made by cascading a 33/66- and a 50/100-GHz optical IL and with a 3-dB passband of 37 GHz, are shown in Figure 3.21(a) and 3.21(b), respectively. It is clearly seen that the multiple

sidebands are suppressed over 20 dB while keeping the original carrier and the two modulated first upper-order sidebands. An EDFA is used to compensate around 11-dB insertion loss from the IM and cascaded ILs. The other IM (MZM_2) driven by a 20-GHz clock signal and an OF_2, which comprising of a 25/50- and another 50/100-GHz IL, are used to complete the multi-band up-conversion process. Figure 3.21(c) and 3.21(d) show the optical spectra of the output of the MZM_2, and the transmission window and the output of the OF_2, respectively. It is clear that, the unwanted optical carriers and the 2nd-order sidebands are now suppressed over 20 dB, as shown in Figure 3.21(d). Then, the generated optical multi-band 60-GHz signals, including a 55-GHz and a 60-GHz mmW, are amplified before their transmission over a 50-km SMF-28. The reason why we have to cascade several ILs as OFs is from the fixed passbands and stopbands of the available ILs. Commercial tunable 33/66-GHz ILs can be used as the OF_1 and OF_2 in the proposed setup, even for multi-band 60-GHz wireless systems with more closely-spaced RF carriers defined by the ECMA-387.

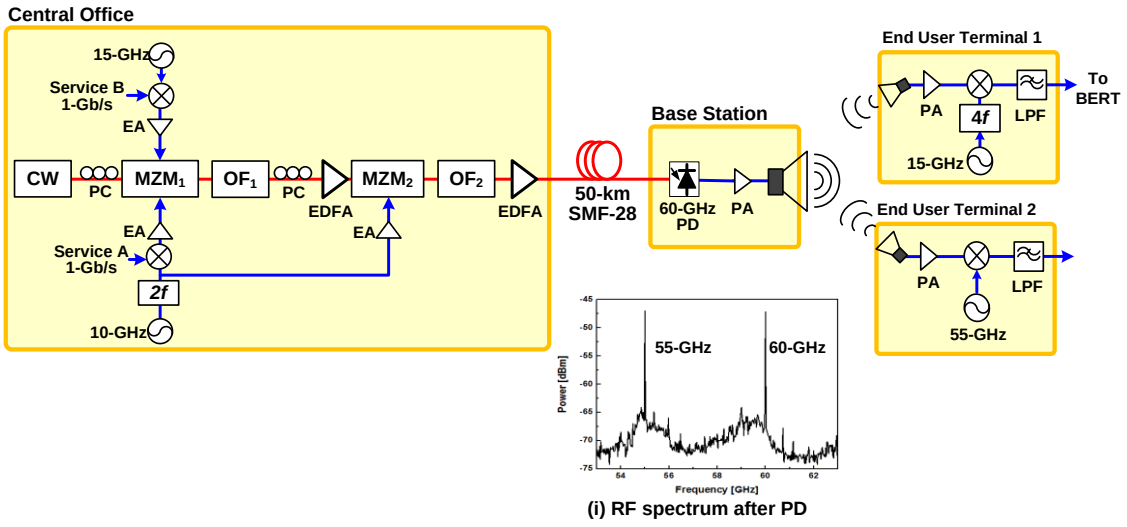

Figure 3.20. Experimental setup for the simultaneous generation of multi-band signals at 60-GHz sub-bands based on cascaded modulation. The RF spectrum with a 55-GHz and a 66-GHz signal is inserted as inset (i) (resolution bandwidth: 3 MHz).

At the BS, the 55-GHz and 60-GHz mmW optical wireless signals are received by a 50-GHz PD. The converted electrical mmW signal is then amplified by a PA with a 7-GHz bandwidth centered at 60 GHz. Although the 55-GHz signal, which is at the edge of bandwidth of the PA, cannot get very flat and maximum gain, the amplified power is still large enough for its data recovery. The inset of Figure 3.20 shows the multi-carrier tones at 55-GHz and 60-GHz mmW. A pair of double-ridge guide rectangular horn antennas, which have 15 dBi gain at the range of 50 GHz to 75 GHz, are utilized to broadcast and receive the multi-band 60-GHz signals. After the electrical multi-band signals are transmitted through a length of air and arrived in an end user terminal, a 60-GHz LO signal is mixed with the received signals to accomplish down-conversion process. A LPF with a 933-MHz bandwidth is used recover the 1-Gb/s baseband data before BER test.

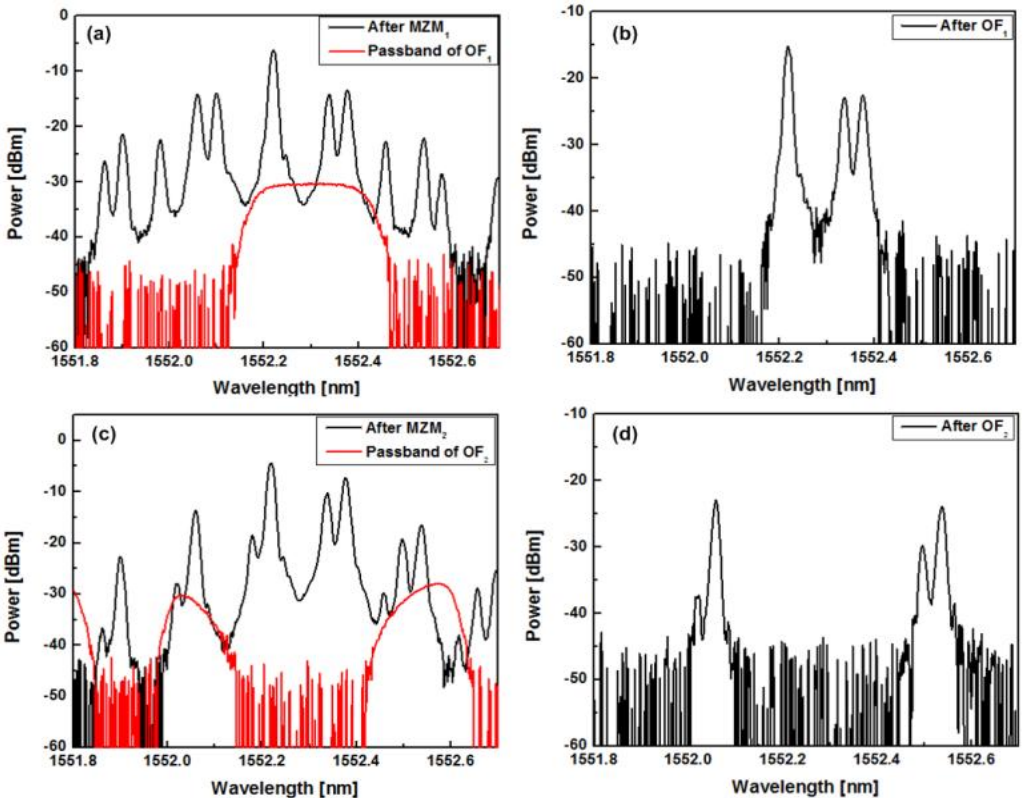

Figure 3.21. The optical spectra at various points (a) the output of MZM_1 and the passband of OF_1, (b) the output of OF_1, (c) the output of MZM_2 and the passband of OF_2, and (d) the output of OF_2 (resolution bandwidth: 0.01 nm).

In Figure 3.22, we measure the BER of the 60-GHz band with or without the presence of 55-GHz band after a 6-m wireless transmission. The 60-GHz signal in the multi-band case needs 2 dB more power to achieve BER = 10^{-9} compared by the single-band case. Moreover, the penalty from the 50-km SMF transmission is 0.8 dB at the BER of 10^{-9} for both single-band and multi-band cases. The insets of Figure 3.22 show the optical eye diagrams for the 55-GHz and 60-GHz signals individually, and the filtering effect in the 55-GHz eye diagram is caused by the imperfect optical filter (OF_2) in the up-conversion process.

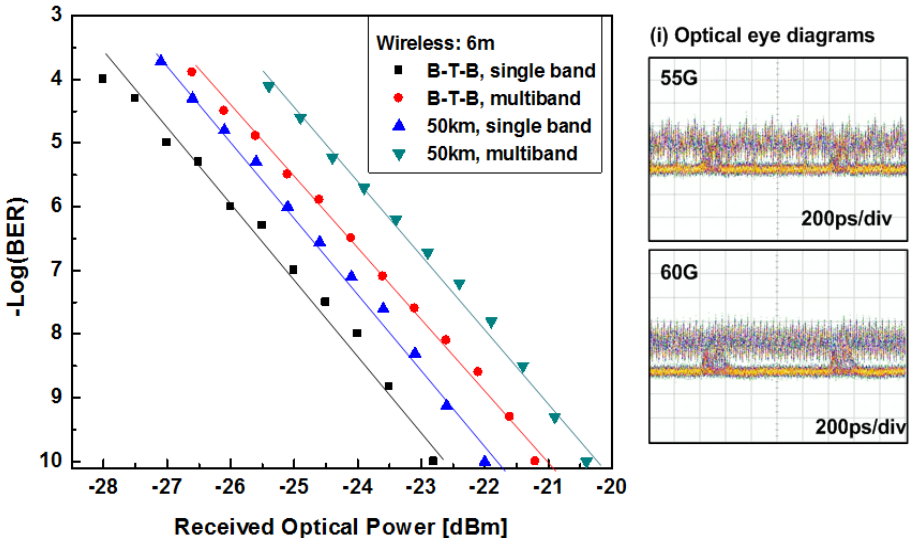

Figure 3.22. BER measurements of the 60-GHz service with or without the presence of the 55-GHz service after a 6-m wireless transmission.

We plot the BER against the distance of free-space propagation with EIRP = 19.8 dBm, under the FCC regulations for in-building 60-GHz radio frequency applications, in Figure 3.23. At the BER of 10^{-9}, the achieved wireless distance of the multi-band transmission is 4 m compared to 6 m in the single-band case. The penalty mainly arises from the lower EIRP for each band signal in the multi-band case compared with the one in single-band case, and some interference from the 55-GHz signal. Therefore, we can improve the performance of the multi-band case by adding a band pass filter to separate

the two bands signals before the down-conversion. The electrical eye diagrams after a 50-km transmission for the down-converted 60-GHz signal are also provided in the insets of Figure 3.23.

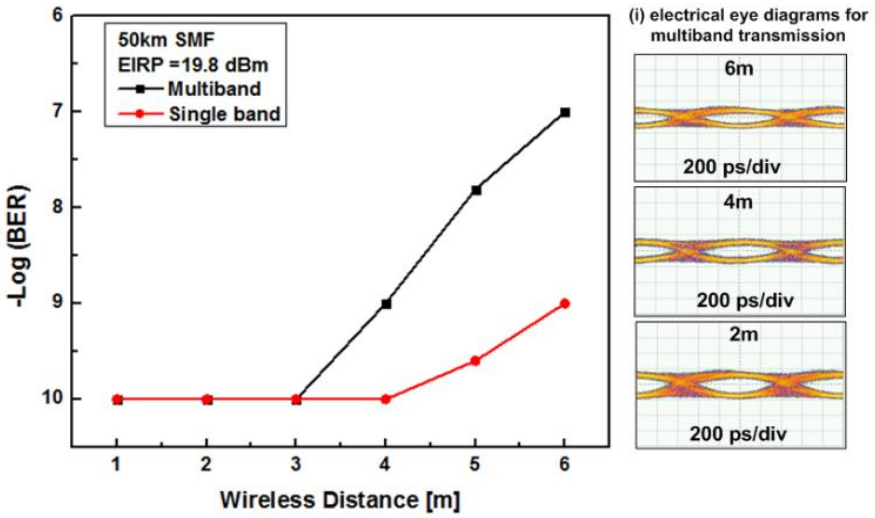

Figure 3.23. BER versus wireless distance for the 60-GHz service with or without the presence of the 55-GHz service with EIRP = 19.8 dBm and after a 50-km SMF-28 transmission.

3.4.2 Converged All-band 60-GHz RoF System

Mapping the commercial wireless services at low RF regions to some 60-GHz sub-bands, as Figure 3.24, makes the new 60-GHz band distribution not only provides VHT data and video distributions but also have the backward compatibility of legacy wireless services. As shown in Figure 3.25, multiple services are optically up-converted to 60-GHz sub-bands based on the RoF technology, which is accomplished in the main hub. After fiber transmission, the all-band signal is distributed to RAUs and then broadcasted to end terminals by using 60-GHz band antennas. These end terminals only need 60-GHz wireless transceivers to enjoy multi-band wireless services. Therefore, the proposed idea can be applied to construct a converged all-bands 60-GHz RoF access network. Based on this novel technology, we experimentally demonstrated a full-duplex and lightwave-centralized 60-GHz RoF system, which can simultaneously generate and

transmit one VHT data and three low-data-rate wireless services through 50-km SMF-28 and radio propagations.

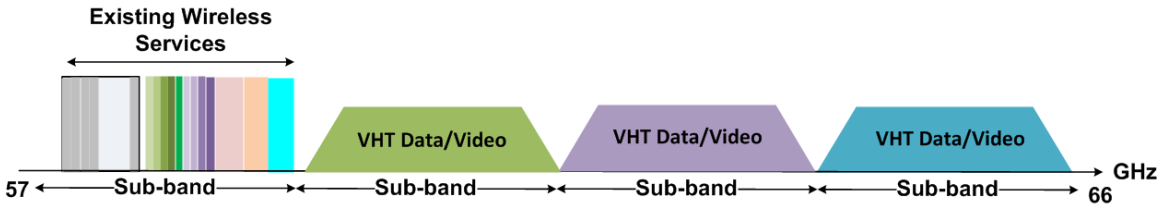

Figure 3.24. Band-mapping concept.

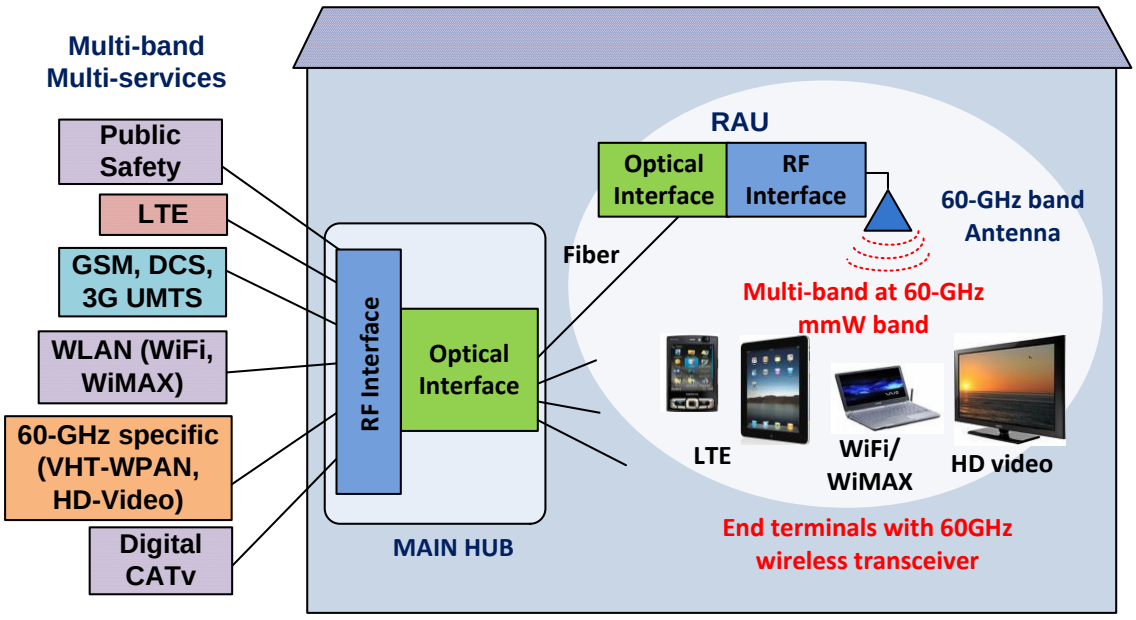

Figure 3.25. Schematic diagram of a converged all-band 60-GHz RoF system.

Figure 3.26 illustrates the experimental setup of the proposed converged all-band 60-GHz RoF system based on a single dual-arm MZM, which delivers four-band DL and UL signals. At the main hub, one CW lightwave is generated by a DFB-LD at 1554.15nm and followed by a dual-arm MZM, which is driven by an amplified 30-GHz RF sinusoidal clock with *Vpp* of 4.5 V and a four-band OFDM-16QAM DL signal. The IFs for four bands are 0.5 GHz, 1.17 GHz, 1.20 GHz, and 1.23 GHz, respectively. The first

band and the other three bands carry 1.5-Gb/s and 60-Mb/s OFDM-16QAM data respectively, which are generated by an arbitrary waveform generator operating at 2.5 GS/s. After the MZM, multi-carriers with spacing of 30 GHz are generated as Figure 3.26(i): only the central carrier is with DL data, and other sub-carriers are CW lightwaves without data. By utilizing a MZM with less $V\pi$, the levels of 2nd-order sidebands can be more equal to the central carrier.

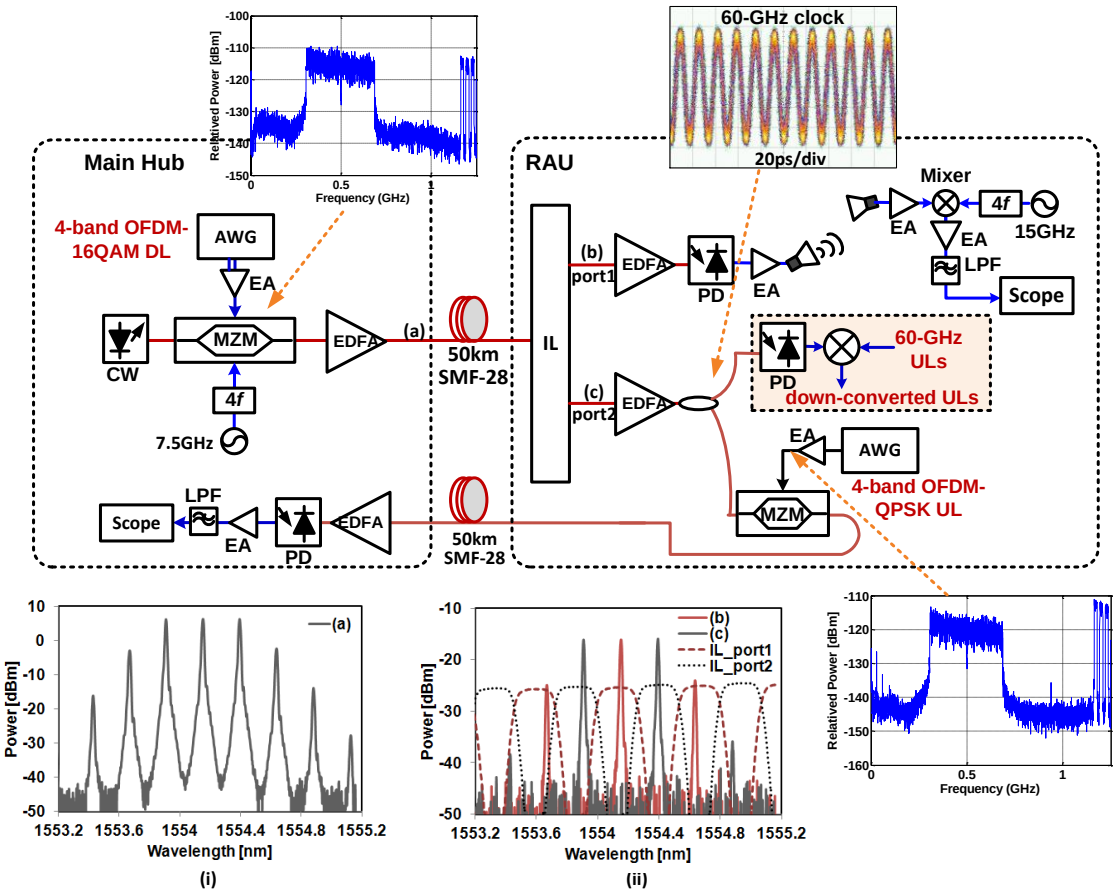

Figure 3.26. Experimental setup for the proposed converged all-band 60-GHz RoF scheme based on a dual-arm MZM, and the corresponding RF spectra (resolution: 3 MHz), optical eye diagram, and optical spectra (resolution: 0.01 nm).

After amplification and 50-km SMF-28 transmission, one 33/66 GHz optical IL in RAU is used to separate the 1st-order sidebands from other carriers as shown in Figure

3.26(ii). The central carrier and 2nd-order sidebands from the port1 of IL are sent to a 50-GHz bandwidth PD with responsivity of 0.65 A/W, and the converted electrical mmW signal (with four bands at 60.5 GHz, 61.17GHz, 61.2 GHz, and 61.23GHz) is then amplified by a EA with 25-dB gain and 10-GHz bandwidth centered at 61-GHz. The reason why we chose these bands over the ones shown in Figure 3.24 is the limitation of maximum sampling rate of our arbitrary waveform generator (2.6 GS/s). A pair of double-ridge guide rectangular horn antennas with 15 dBi gain at the range of 50-GHz to 75-GHz are utilized to broadcast and receive the 60-GHz DL signal. After the DL signal is transmitted through a length of air and arrived in an end terminal, a 60-GHz electrical LO by is mixed with the received DL signal to accomplish down-conversion process. Finally, the amplified down-converted DL with 10-GHz LPF is sent to a real-time digital storage oscilloscope at 10 GS/s for offline demodulation procession.

The two 1st-order sidebands from the port2 of IL are first divided into two parts: one part are used as optical carriers for UL modulation, and the other part can generate a pure 60-GHz clock source after O/E conversion. The 60-GHz uplink signals from end terminals can be down-converted to baseband by being mixed with the produced 60-GHz clock signal, as the pink block in Figure 3.26 shows. The down-conversion accomplished by the produced 60-GHz clock can relax the bandwidth requirement of electronic components used for UL transmission and then decrease system cost. The UL down-conversion function is not implemented here on account of the absence of enough 60-GHz EAs and mixers; nevertheless, an optical eye diagram of produced 60-GHz clock signal is shown in the inset of Figure 3.26. Thus, by an arbitrary waveform generator at 2.5 GS/s, a four-band OFDM-QPSK signal is generated as the UL signal after down-conversion. Four UL bands have the same IF distributions and half data rates with the DL signal. The optical signal carrying UL data, which is done by a 20-GHz MZM, is sent back to the main hub over 50-km SMF-28 and then detected by a 2.5-GHz receiver. For the DL and UL signals, their FFT sizes are 128, where 95 subcarriers are mapped with

RBS streams, 32 subcarriers for guard channels, and one subcarrier in the middle of the OFDM spectrum is set to zero for DC in baseband. CP with length of 32 symbols has been applied to resist chromatic dispersions.

Performance of each demodulated service is evaluated by the EVM parameter. The EVMs for DL1 (1.5 Gb/s) and DL2 (60 Mb/s) signals at different wireless transmission distance are illustrated in Figure 3.27. The total EIRP of four-band signal is -4 dBm. The three low-data-rates bands have similar EVMs; therefore, only the results with IF of 1.17GHz (DL2) is shown here. In brief, the results from this figure can be summarized as follows: first, the EVMs of DL1 and DL2 after 50-km SSMF and 4 m radio propagations are less than -15dB and -20dB, respectively; and second, the EVM penalty caused by 50-km SSMF is around 0.5 dB for DL1 and DL2.

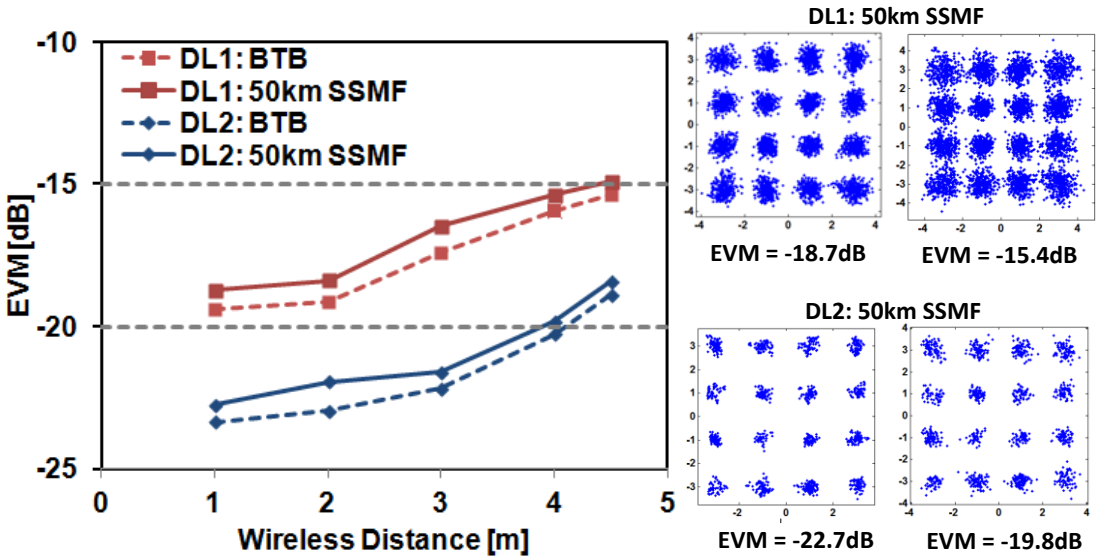

Figure 3.27. EVM vs. wireless distance for DL1 and DL2 with and without 50-km SSMF transmission at EIRP of -4 dBm.

Moreover, Figure 3.28 shows the EVM measurements as a functional of total optical received power for UL1 (0.75 Gb/s) and UL2 (30 Mb/s) signals. Optical receiver sensitivities of UL1 at EVM < 18 dB are -5 dBm and -5.5 dBm for 50-km SSMF and BTB transmissions, respectively, while the EVMs of UL2 with optical received power

from -8 to -3 dBm are always under -20dB. The optical power penalties induced by 50-km SSMF for DL and UL transmissions are mainly due to the ASE noise from the EDFAs used to compensate the fiber loss. The fiber chromatic dispersion penalty can be ignored because the symbol rate of each subcarrier for DL and UL is less than 20MSym/s. The constellations of the OFDM-16QAM and OFDM-QPSK after fiber and air transmissions are also shown in Figure 3.27 and Figure 3.28, respectively. The EVM floors for DL and UL transmissions are limited by the noise from the EAs used to amplify the signals generated by the AWG. As shown in the insets of Figure 3.26, the signal-to-noise ratios of DL and UL signals after EAs are only ~20dB. The way to improve system performance is to utilize EAs with lower noise and a MZM with smaller $V\pi$ as the replacements.

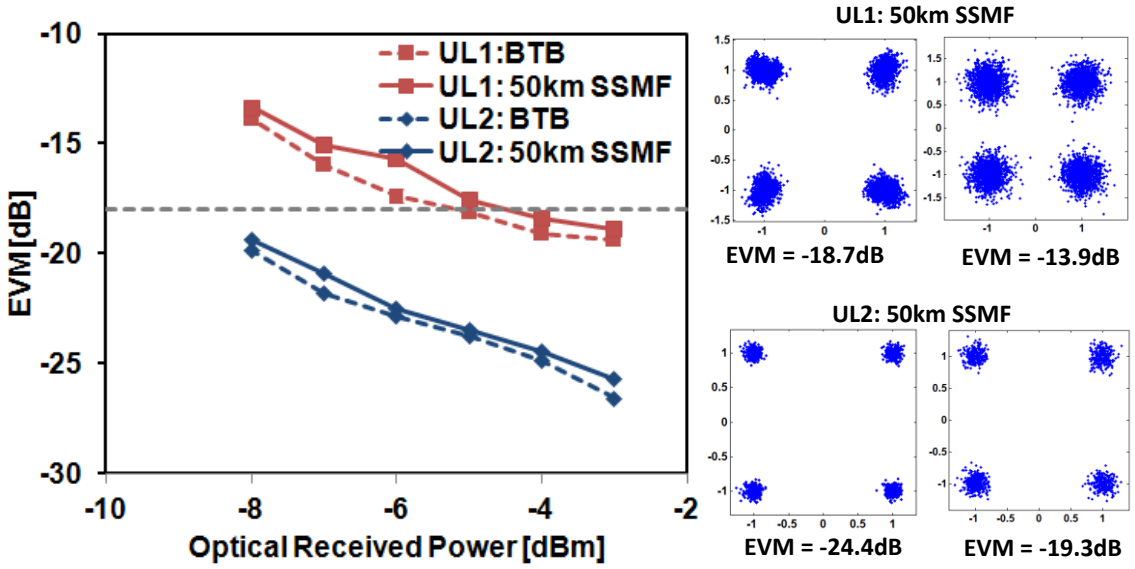

Figure 3.28. EVM vs. optical received power for UL1 and UL2 with and without 50-km SSMF transmission.

3.5 Chapter Summary

In this chapter, we design and demonstrate several novel mmW RoF

architectures for simultaneously delivering wired and multi-band wireless services on a single optical transport platform. These schemes can efficiently generate and distribute multiple wired and wireless services to the users' premises. Table 3.1 summarizes the advantages and disadvantages of these designs with multi-band services; their system design focuses on: high tolerance to CD to increase fiber transmission distance, frequency doubling/tripling to relax the bandwidth requirement for electronic devices, lightwave centralization to decrease the cost of BS, independent signal generation to improve system flexibility, and backward compatibility of wireless services in low RF regions to accomplish a converged system.

Table 3.1. Summarization of proposed multi-band RoF systems

Scheme	Advantage	Disadvantage
Baseband, MW, and mmW		
OSSB+C format based on a dual-arm MZM	· Long fiber transmission distance · Simple CO design · Lightwave centralization with remote carrier delivery for UL	· The need for a specific OF in BS · The need for a 40 GHz LO in CO · Identical signals for multiple bands
MmW with wireless services at low RF regions		
Multi-carriers generation based on a PM	· Independent signal for each band service · Backward compatibility of legacy wireless services · Frequency doubling	· The need for a specific OF in CO · Limited fiber transmission distance due to CD
Multi-carriers generation based on a dual-arm MZM	· Independent OFDM signal for each band · Backward compatibility of legacy wireless services · Remote carrier delivery for ULs · Bidirectional transmission via one fiber span with low RB · Frequency doubling	· The need for a specific OF in BS · Limited fiber transmission distance due to CD · The need for large driving LO in CO
60 GHz sub-bands		
OSSB+C format based on cascaded modulation	· Long fiber transmission distance · Independent signal for each band · Frequency tripling	· The need for specific OFs in CO
OSSB+C format based on a dual-arm MZM	· Long fiber transmission distance · Independent OFDM signal for each band · Frequency doubling · Reproduced 60GHz clock for UL down-conversion · Remote carrier delivery for ULs · Backward compatibility of legacy wireless services	· The need for large driving LO in CO

CHAPTER 4

112-GB/S PDM-QPSK OPTICAL TRANSPORT SYSTEM

Carriers are challenged increasingly by the high-bandwidth demands for new applications, and consequently 100-Gb/s transport system is viewed as the most promising method to meet tomorrow's networking needs. In this chapter, the designs of transmitter, receiver, and transmission link for our 100G optical system is presented in section 4.1. The engineering rules of dispersion management for a 100G system propagating with the deployed 10G channels are investigated in section 4.2. Finally, 100G DWDM networks with reconfigurable optical add-drop multiplexers (ROADMs) enable dynamically reconfigurable networks; the two key transmission impairments induced by ROADMs, passband and in-band crosstalk effects, are experimentally and numerically analyzed in section 4.3.

4.1 Introduction

The serial 100-Gb/s transport is viewed as the most cost-effective choice for the 100G transmission in the long haul networks. Various modulation formats have been discussed for the serial 100G transport such as NRZ on/off keying (OOK), duobinary, vestigial sideband NRZ, differential QPSK (DQPSK) and polarization-multiplexing (Pol-Mux) (D)QPSK. The measured performances for these formats are shown in Figure 4.1 [88]. The performances for binary formats (100-Gbaud) are limited by the bandwidth of electronic and optoelectronic hardwares. The Pol-Mux (D)QPSK format (25 Gbaud) utilizes not only multi-level phase modulation but also polarization-division multiplexing (PDM) and decrease the bandwidth requirements for the electronic components. Moreover, the narrow optical spectrum of PDM-(D)QPSK leads to enhanced tolerance against CD and PMD and facilitates an operation at the 50-GHz ITU WDM grid, which

can achieve higher spectral efficiency compared with binary formats. Therefore, PDM-(D)QPSK has been viewed as the most promising approach for 100G WAN transmission.

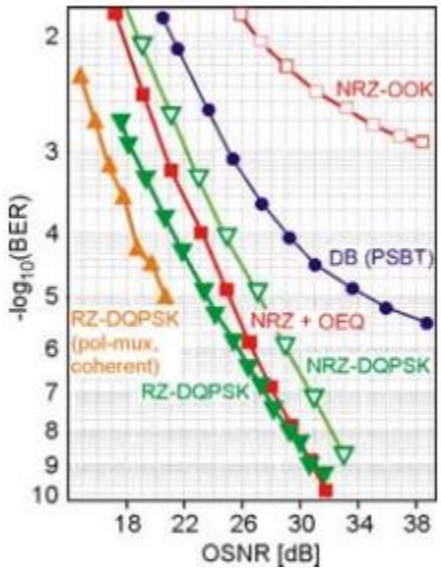

Figure 4.1. BER measurements for BTB 107-Gb/s systems with different modulation formats [88].

4.1.1 Transmitter Design

In Figure 4.2, the (D)QPSK signal is generated using a IQ modulator, which is comprised of a 3 dB optical power splitter, two parallel MZMs, and opticla phase shift and an optical power combiner. The parallel MZMs are biased for minimum optical transmission ($V\pi$) and driven with two 28-Gb/s PRBS data streams with a word length of 2^{15}-1 and the V_{pp} of $2V\pi$. Signals from the in-phase (I) and quadrature (Q) arms are recombined with a relative optical phase shift of $\pi/2$. If the data streams originate from the data and data bar of a pattern generator, it needs integer bits relative delay between them to ensure no correlation and fully explore the (D)QPSK constellation. In (D)QPSK, the information bits are encoded into the phase of the optical carrier and the amplitude of the signal remains constant. The electrical field of QPSK signal can be represented as follows

$$E_0 e^{j(\omega_c t+\varphi_k)}, kT \le t < (k+1)T, \tag{4.1}$$

$$\varphi_k = \begin{cases} \pi/4 & if\big(I(k), Q(k)\big) = (0,0) \\ 3\pi/4 & if\big(I(k), Q(k)\big) = (1,0) \\ 5\pi/4 & if\big(I(k), Q(k)\big) = (1,1) \\ 7\pi/4 & if\big(I(k), Q(k)\big) = (0,1). \end{cases}$$

Here, ω_c is the angular frequency of the carrier, φ_k is the phase of the carrier in the time interval [*kT*, *(k+1)T*], and (*I(k), Q(k)*) is the k_{th} symbol to be transmitted. The RZ format with 50% duty cycle can be created by using another MZM, which is driven at clock rate of 28-GHz between minimum and maximum transmission [89]. The polarization-multiplexed signal is generated by dividing and recombining the signal with some symbol delay using a polarization beam splitter (PBS). Figure 4.3 shows the optical spectra and eye diagrams for the 28-Gbaud NRZ- and RZ-(D)QPSK signals.

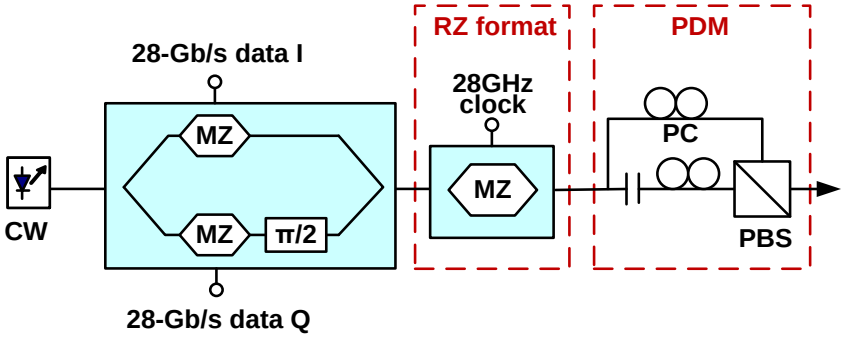

Figure 4.2. Experimental setup of a 112-Gb/s PDM-QPSK transmitter.

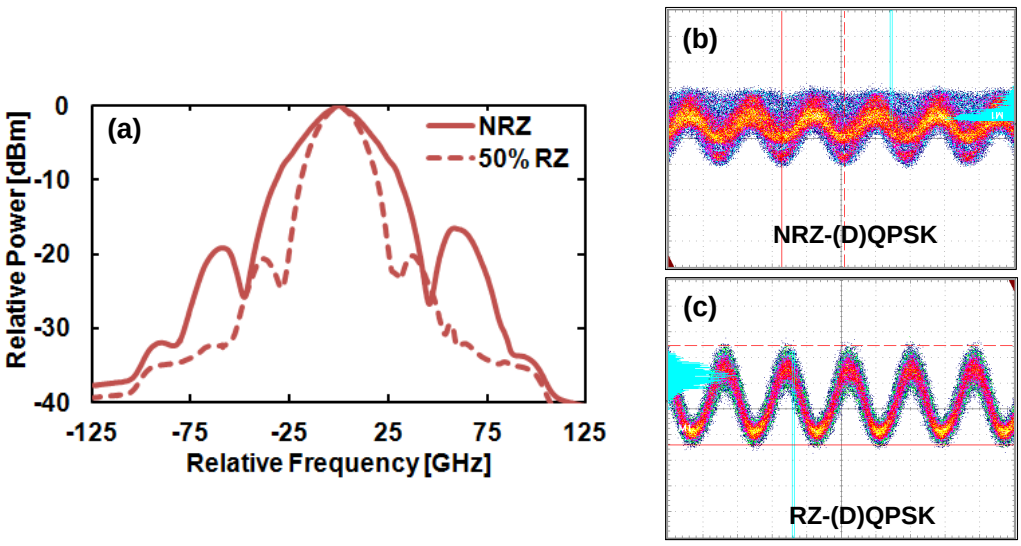

Figure 4.3. (a) Optical spectra and (b), (c) optical eye diagrams of 28 Gbaud NRZ- and RZ-(D)QPSK signal.

4.1.2 Receiver Design

We experimentally constructed two demodulation methods: direction detection for DQPSK signal and coherent detection for QPSK signal as shown in Figure 4.4(a) and 4.4(b), respectively. As shown in Figure 4.4(a), the direction detection technique employs a Mach-Zehnder delay interferometers (MZDI) for the demodulation of each quadrature, followed by the balanced detection. The two DIs are typically designed to have a differential delay of a symbol period T but must be phase shifted differently (by $\pm$ π/4) to decode the in-phase (I) and quadrature (Q) tributaries correctly. Note that the opposite phases of the DIs are equivalent to opposite frequency detunings of $\delta f = \pm S/8$ relative to carrier frequency, where $S = 1/T$ is the baud rate. Assuming ideal 3-dB coupler, the electrical field of the output I1 and Q1 in Figure 4.4 are

$$E_{I1} = \frac{1}{\sqrt{2}} E_0 e^{j(\omega_c t)} (e^{j\varphi_{k-1}} + e^{j(\varphi_k + \pi/4)}), \tag{4.2}$$

$$E_{Q1} = \frac{1}{\sqrt{2}} E_0 e^{j(\omega_c t)} \left(e^{j\varphi_{k-1}} + e^{j(\varphi_k - \frac{\pi}{4})}\right). \tag{4.3}$$

After two balanced receiver with responsibity R, the photocurrent of upper branch is

$$i_I(t) = \frac{{E_0}^2}{2}\cos\left(\Delta\varphi_k + \frac{\pi}{4}\right), \tag{4.4}$$

and the photocurrent of the lower branch is

$$i_Q(t) = \frac{{E_0}^2}{2}\cos(\Delta\varphi_k - \pi/4), \tag{4.5}$$

where $\Delta\varphi_k = \varphi_k - \varphi_{k-1}$. The values of i_I and i_Q can then be used to estimate the transmitted symbol. Typically, for DQPSK transmission, the incoming data streams are pre-coded and then sent to the DQPSK transmitter [90]; after DQPSK demodulator, then, the output signal should be equivalent to the incoming streams. In our experiments, however, we choose decoding method because our BER analyzer can predicts the expected bit sequence after demodulation by the DQPSK receiver [91]. This scenario is more convenient and flexible in the laboratories. Furthermore, for a PDM-DQPSK signal with BTB transmission, the polarization demultiplexing can be achieved by a polarization controller (PC) followed by a PBS as shown in Figure 4.4(a). If the PDM-DQPSK signal is transmitted through a long fiber link, a polarization tracker is needed to automatically rotate the polarization status for the direct detection [92].

For the coherent detection, Figure 4.4(b), the incoming QPSK signal beats with the LO, and the optical 90^o hybrid enables to extract phase and amplitude from the transmitting signal. Simultaneous recovery of data on both polarizations is achieved using a polarization diverse optical 90^o hybrid. After detected by the balanced receivers, the output signals are digitized using a 40-GS/s real-time oscilloscope with front-end analog bandwidth of 16 GHz for the digital signal processing (DSP), which can achieve clock and carrier recovery, transmission impairment mitigation, and polarization demultiplexing. Our offline DSP, employing a standard approach to PDM-QPSK, is done

in six distinct steps [93, 94]. In order, these steps are: (1) chromatic dispersion equalization [94], (2) adaptive polarization demultiplexing based on constant modulus algorithm (CMA) [95], (3) symbol timing recovery via the common digital square and filter method [93], (4) carrier phase recovery with feed-forward Viterbi-Viterbi method [96], (5) per-polarization 15-tap and $T_s/2$-spaced least mean square (LMS) equalization, and (6) symbol detection. All processing is done in a Matlab environment.

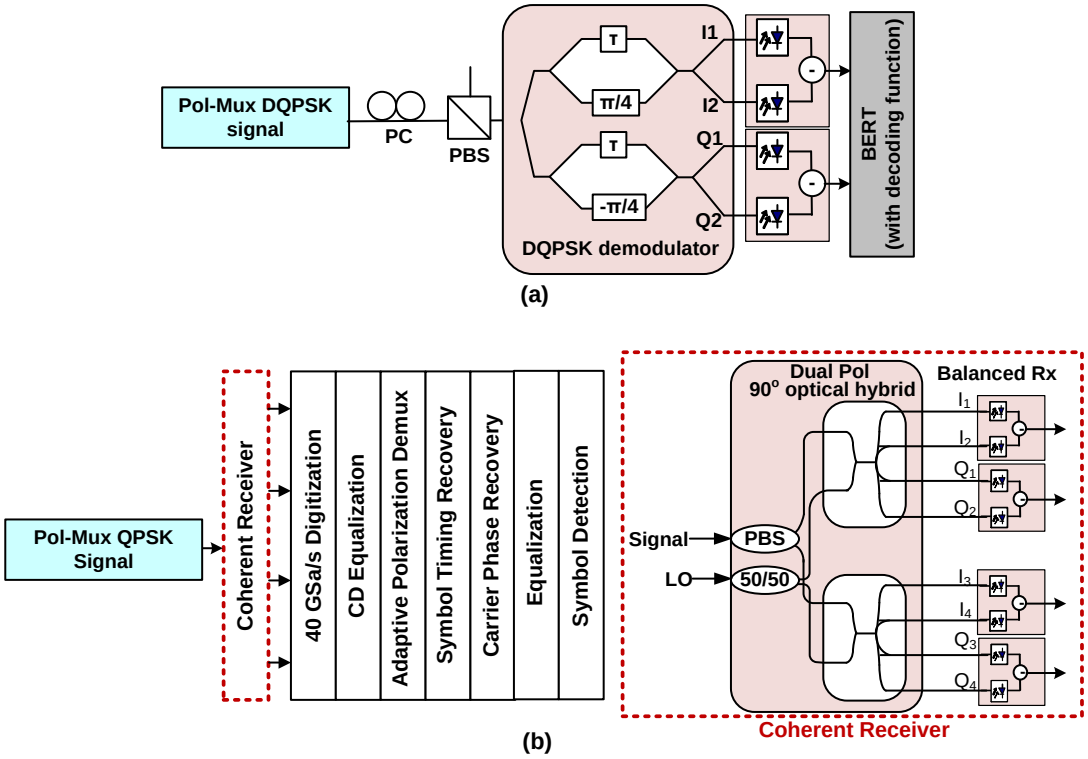

Figure 4.4. Schematic diagrams of (a) direction detection for DQPSK signal and (b) coherent detection for the QPSK signal.

Figure 4.5 shows the BTB BER measurements of the simulation (by Rsoft) and experimental results for the 56-Gb/s (D)QPSK and 112-Gb/s PDM-(D)QSPK signals with the direct and coherent detection. The OSNR value is set using a ASE source with a variable optical attenuator (VOA), which are put before the receiver. As shown in Figure 4.5, the OSNR performances of the coherent detection are 1.5 dB better than the ones of the direct detection, which is consistent with the theoretical analysis [97]. As expected,

the difference in required OSNR between single-polarization (single-pol) and dual-polarization (DP) is about 3 dB. For BER = 10^{-3}, for example, the required OSNR is 15 dB and 12.8 dB for 56-Gb/s (single-pol) and 112-Gb/s (DP) signal, respectively. Moreover, the difference between the laboratory and the simulation is within 0.5 dB in all cases, which results from correct modeling of light propagation in fiber and specific, measured characteristics of laboratory equipment.

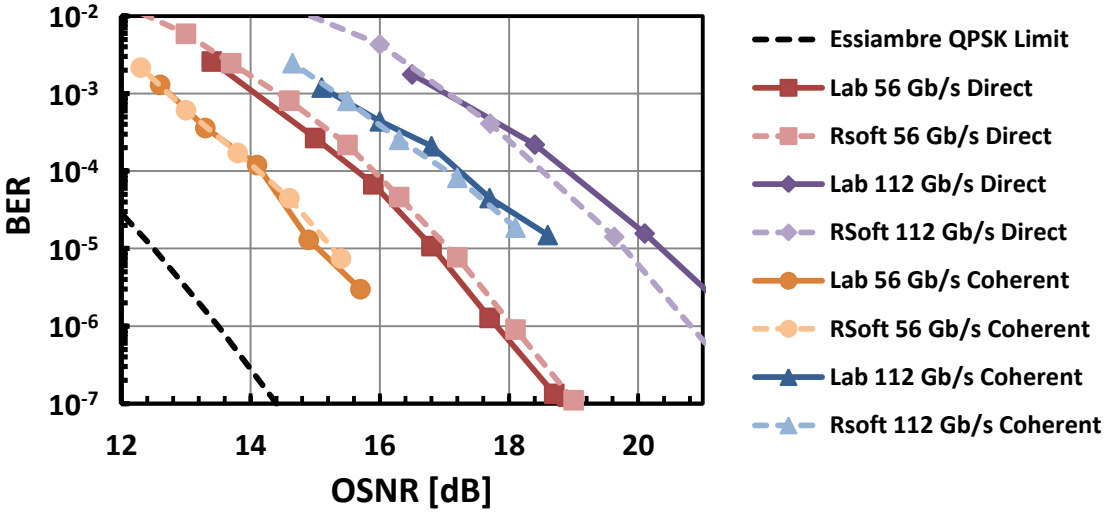

Figure 4.5. BER versus ONSR for 56-Gb/s (D)QPSK and 112-Gb/s PDM-(D)QSPK systems with the direct and coherent detection.

4.1.3 Transmission Line Design

Two different link configurations are investigated: a point-to-point (PtP) link and a recirculating loop as shown in Figure 4.6(a) and 4.6(b), respectively. The 8-span PtP link is configured in two ways: (1) 90-km SSMF spans, (2) 80-km non-zero dispersion-shifted fiber (NZDSF) spans. Each span in PtP link is comprised of one EDFA with midstage access for optional dispersion compensation. Our recirculating loop setup consists of two acousto-optic modulators as transmitter and loop switch, two optical 3 dB couplers, a dynamic channel equalizer formed by a BPF, and three 90-km SSMF spans

with EDFA amplification. Closing the transmitter switch loads the data stream into the optical loop (via the 3-dB coupler). After the loop fills with data, the transmitter switch opens and the loop switch closes. The loaded bit stream then recirculates around the loop. Each time around the loop the data passes through the coupler. The coupler directs a portion of the data to the receiver part. The construction of recirulating loop can increase the transmission distance from the PtP link configuration. In all loop experiments, the signal is propagated six times around the loop for 1,620 km total transmission distance. Table 4.1 summarizes some key parameters of SSMF and NZDSF we used.

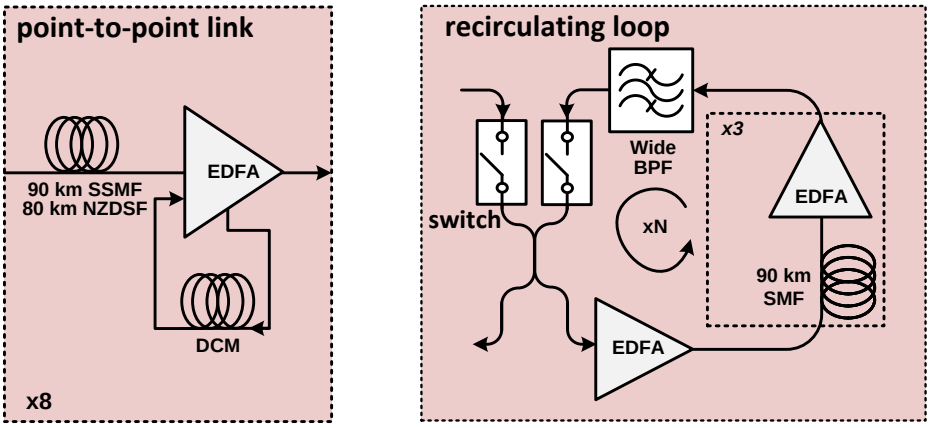

Figure 4.6. Transmission line design: (a) point-to-point link and (b) recirculating loop.

Table 4.1 Key parameters of SSMF and NZDSF.

	SSMF	NZDSF
Attenuation @ 1550nm [dB/km]	< 0.19	<0.20
Dispersion @ C band [ps/nm·km]	16*	2.6 - 6.0
Effective area [μm^2]	80	52

* for 1550 nm signal

4.2 Dispersion Management

Deployments of 100G (D)QPSK systems may occur on the already-deployed network infrastructure with existing 10G OOK channels, or in banks adjacent to other

(D)QPSK channels at the same line rate. It is therefore important to quantify and understand the (D)QPSK performance for different dispersion maps in a hybrid network configuration to build up a systematic understanding of nonlinear impairments in single-pol and PDM cases. Recent reports have shown that dispersion management, including pre-compensation (pre-comp), inline compensation, and post-compensation (post-comp), can effectively limit the transmission impairments induced by of these nonlinear interactions [32-33, 98-100] for the 43-Gb/s systems. Here we experimentally examined the dispersion management for a system with one 28-Gbaud RZ-DQPSK channel and adjacent two 12-Gb/s OOK channels as shown in Figure 4.7.

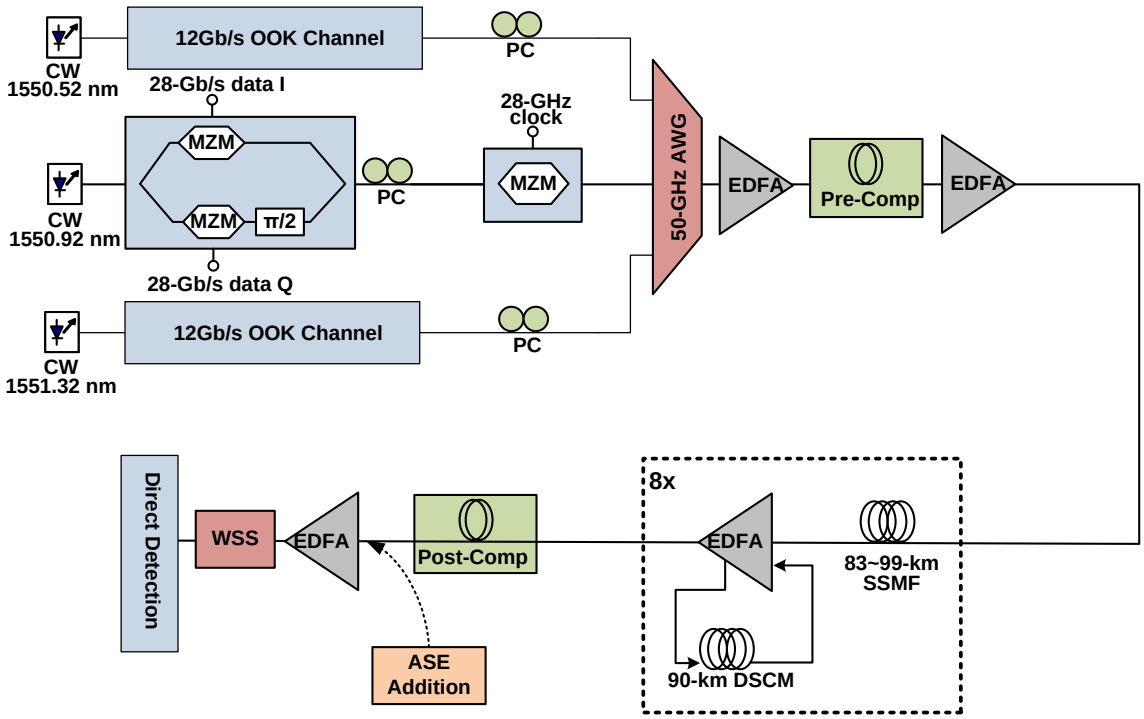

Figure 4.7. Experimental setup of the hybrid system through a PtP link and direct detection.

One experimental setup consists of a 56-Gb/s single-pol RZ-DQPSK and two 12-Gb/s OOKs as a hybrid system, using wavelengths of 1550.52 nm, 1550.92 nm and 1551.32 nm (50-GHz spacing). All of the channels are co-polarized for the worst-case

analysis. After combining in a 50-GHz AWG, pre-comp is done in 10-km increments by use of a reconfigurable dispersion compensation module, and then transmitted through a PtP link. The PtP link here includes eight 90-km spans of SSMF. The inline compensation, represented by residual dispersion per span (RDSP), is varied by changing the length of each span using of a set of tuning spools while keeping the dispersion compensation modules (DSCMs) fixed. Each DSCM provides the compensation of -1530 ps/nm, which is corresponding 90-km SSMF. Before the receiver, two tunable fiber Bragg gratings (TFBGs) are used to post-compensate for the net residual dispersion of the link. Finally, the RZ-DQPSK channel is demodulated by a commercial 28GHz DQPSK demodulator, and the two outputs of I or Q component are differentially detected by a balanced receiver. Using this setup we independently control several variables of interest: received OSNR, RDPS, launch power, and pre-comp.

For all experiments we conducted with this setup, the launch power of two 12-Gb/s channels is fixed at 0 dBm (typical of deployed systems) while the launch power of QPSK signal is varied from -2 to 4 dBm. By varying the length of each span, RDPS is controlled between -119 and +153 ps/nm. Current regional and long haul deployments typically range from +50 to +150 ps/nm for RDPS (under compensation), and we span the negative dispersion regime to examine a wide range of possibilities. Three different pre-compensation values are choose: -170, -680, and -1020 ps/nm, corresponding to 10-, 40-, and 60-km SSMF of pre-comp, respectively, where 30 to 40 km might be common for 10G installed systems. Table 4.2 summarizes the experimental parameters. Each span length corresponds (same order) to each RDPS listed in the table.

Table 4.2 Experimental parameters for dispersion map analysis.

Parameter	**Tested Values**
Span Length [km]	83, 86, 90, 93, 96, 99
RDPS [ps/nm]	-119, -68, 0, +51, +102, +153
Pre-Compensation [ps/nm]	-170, -680, -1020
Launch Power [dBm]	-2, 0, +2, +4

As shown in Figure 4.8, the variation of dispersion map by adjusting the pre-compensation and RDPS (inline-compensation) shows significant BER performance differences in the DQPSK channel. Among all of them, the configuration with a -170 ps/nm of pre-comp (Figure 4.8(a)) has good and robust performance over the range of RDPS studied. Indeed, all results in Figure 4.8(a) yield BER < 10^{-3} for OSNR > 16 dB. On the other hand, for the pre-comp set to 680 ps/nm or -1020 ps/nm, the optimum RDPS is +153 ps/nm, the highest value studied. The BER improvement at a larger-magnitude RDPS can be understood from the fact that larger RDPS provides a more significant walk-off in group delay between the DQPSK and OOK channels, increasing the DQPSK channel's tolerance to the XPM effects. In other words, the configurations with RDPS of +153 ps/nm is insensitive to the pre-comp value. Furthermore, because the time jitter induced by intra-channel FWM and XPM can be suppressed using a symmetric dispersion map [101], the optimum RDPS is also determined by the pre-comp value. For the configurations with pre-comp = -680 and -1020 ps/nm, for example, the RDPS of 0 ps/nm achieves better performance compared with the RDPS of -119 ps/nm. This is because the one with RDPS = 0 ps/nm has more symmetric dispersion map as shown in Figure 4.9. Finally, for +2-dBm launch power case, we find that a near-optimum map includes a pre-comp of -170 ps/nm and an RDPS of -68 ps/nm. This is similar to previously-reported results [33] determined through a global numerical optimization for a 28-Gbaud DQPSK, which found a pre-comp of -150 ps/nm and an RDPS of -10 ps/nm is optimum.

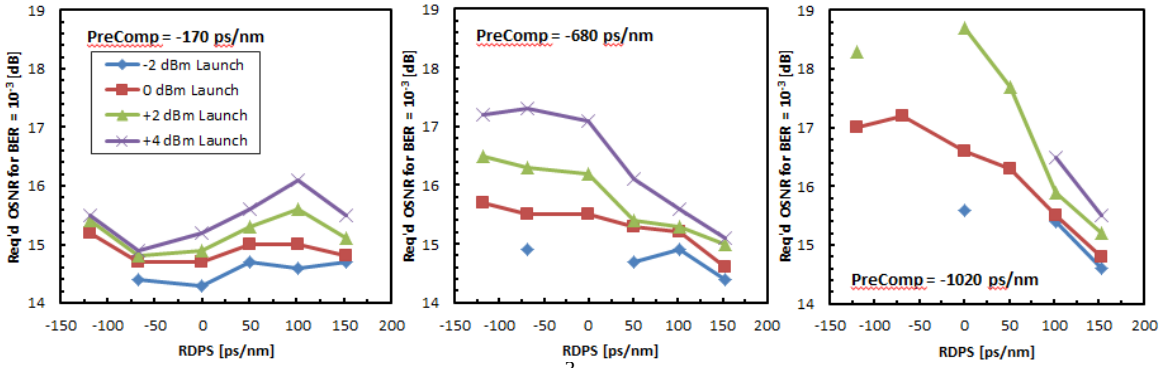

Figure 4.8. Required OSNR for BER = 10^{-3} versus RDPS with a pre-comp of (a) -170 ps/nm, (b) -680 ps/nm, and (c) -1020 ps/nm.

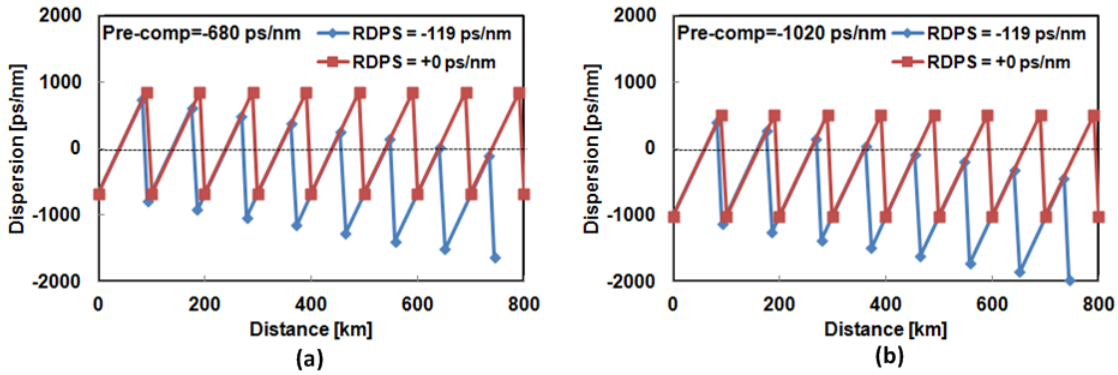

Figure 4.9. Accumulated dispersion for the configurations with RDPS = -119 or +0 ps/nm and with pre-comp of (a) -680 ps/nm, and (b) -1020 ps/nm.

4.3 Transmission Impairments in ROADM-Enabled 100G DWDM Networks

Commercial DWDM networks are not only towards increasing transmission capacity by adding high spectral density transponders but also towards expanded network transparency and system flexibility which are driven by the deployment of add/drop nodes with wavelength reconfigurability. In recent years, reconfigurable optical add/drop multiplexers (ROADMs), which are capable of selective and automatic addition and removal of individual wavelengths from an optical fiber, are broadly applied in DWDM systems as shown in Figure 4.10. They can make the system plan and installation easy and simplify the process of adding a new wavelength into DWDM networks without

manual fiber connections [102]. The key element of a ROADM node is the WSS, which is used to multiplex, demultiplex, and switch DWDM wavelengths between one or several input and output fiber ports.

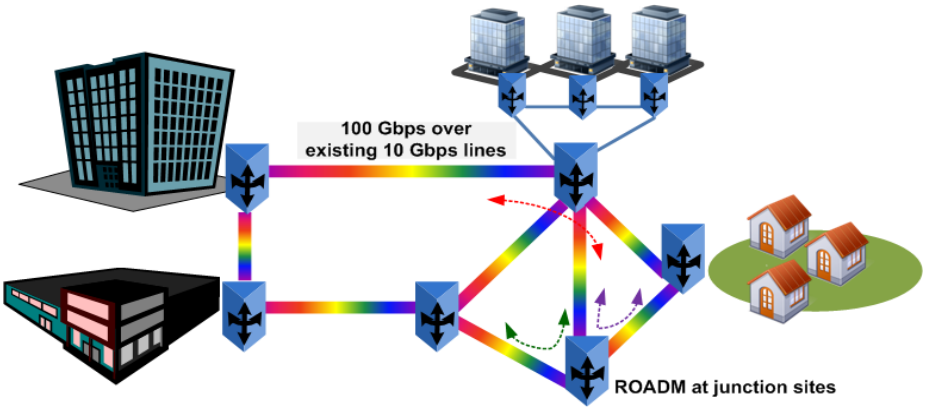

Figure 4.10. 100G DWDM metro network with ROADM nodes.

Deploying ROADMs in long-haul DWDM network also introduces challenges including insertion loss, polarization-dependent loss, transient power effects, passband effects, and in-band crosstalk [36, 103, 104]. In this chapter, passband narrowing and crosstalk effects are investigated. They both are exacerbated by cascaded ROADMs and the very tightly spaced channels needed to support high capacity systems. Passband narrowing is a significant contributor to transmission penalties and is pulse format dependent [105, 106]. A related passband impairment is caused by the relative wavelength detuning between the transmitting signal and the passband center. Here we experimentally investigate the OSNR penalty induced by passband effects for a single 112-Gb/s channel with NRZ/RZ PDM-QPSK format through 1,600 km of SSMF.

In-band crosstalk arises from the finite isolation and non-ideal filter shape of the WSS [107]. In other words, added channels are corrupted by the residual signal energy of a dropped channel within the same band. This system impairment is additive; each successive add/drop increases the crosstalk penalty. Importantly, the non-uniform

spectral content (of both the crosstalk and desired signal) prevents the use of the conventional crosstalk-to-signal power ratio as the sole determining factor of the penalty [106]. Thus, several efforts have been made to quantify WSS-induced crosstalk penalties. A spectrally weighted crosstalk [36, 108] and an integrated crosstalk approach [109, 110] have been proposed to analyze transmission penalties for 10G and 40G systems. Here the weighted crosstalk parameter proposed in [36] can be experimentally extended to successfully predict the transmission penalties for 112-Gb/s PDM-QPSK optical systems comprised of either SSMF, or NZDSF.

In an optical transport network, additional effects may create or enhance crosstalk penalties. In addition to non-ideal ROADMs, potential sources of crosstalk include back-reflections from imperfect connectors, Rayleigh backscattering, and four-wave mixing components in low-dispersion fiber. Furthermore, the crosstalk can have a varying degree of coherence depending on the mechanism and in some cases the location [111] of the crosstalk source. Transmission effects including dispersion and nonlinearities also influence crosstalk penalties. Enhanced crosstalk-induced penalties due to SPM have been reported in 10-Gb/s [112] and 2.5-Gb/s systems [113]. Here the impact of fiber nonlinearities on crosstalk penalties for 100G systems is further studied . Both SPM and XPM are produced and enhanced by increasing launch power and adding adjacent 10-Gb/s OOK channels.

4.3.1 Passband Effects

A 1xN ROADM, Figure 4.11, includes WSS_1 to drop and WSS_2 to add channels. The propagation through a sequence of ROADM nodes spectrally shapes the transmitted signal, limiting its bandwidth and creating signal amplitude, and phase variations. Although ROADMs with higher-order super-Gaussian(SG) filter shapes are available [114], the effective 3-dB filter BW of cascaded 50-GHz ROADMs becomes a limiting

factor as Figure 4.12 shows. For example, the 3-dB BW resulting from more than 9 cascaded 50-GHz ROADMs is less than 40GHz.

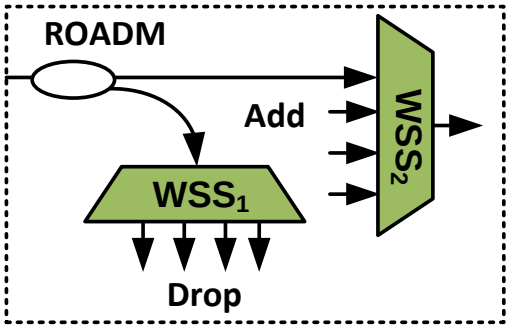

Figure 4.11. 1xN WSS-based RODAM.

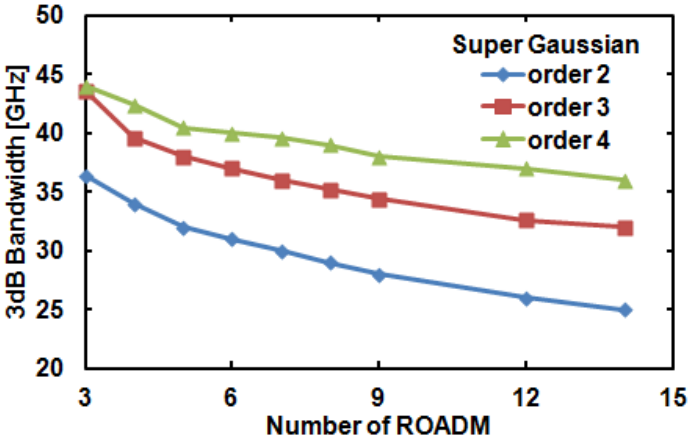

Figure 4.12. Bandwidth narrowing with the increasing number of 50-GHz ROADMs having different super Gaussian orders.

In our experiments, a single WSS with 3rd-order SG is added after the PBS in the transmitter (Figure 4.2), and its bandwidth is varied between 50 GHz to 20 GHz as Figure 4.13(a). In Figure 4.13(b), the required OSNR for BER = 10^{-3} is determined for NRZ- and RZ-QPSK in a BTB configuration with the coherent detection. Generally, narrow filter BWs may cause intersymbol interference (ISI) and wide filter BW may result in inter-channel interference (ICI). Here the NRZ format, having a narrower spectral

content, has a small advantage over RZ for larger filter BW (> 35 GHz). These results are from the electrical filter in the receiver, 16-GHz BW, that removes more energy from the RZ signal than the NRZ. However, when the filter BW becomes narrower, severe ISI is introduced to NRZ signals [115]. On the other hand, for RZ signals, because the signal level between symbols goes to zero, optical ISI is not critical issue; the decrease of signal power due to the narrow optical filter limits performance before ISI sets in [115, 116]. As shown in Figure 4.13(b), RZ shows higher tolerance to filtering/shaping effect and exhibits a negative penalty for BW near 30 GHz. It is a compromise between noise rejection and signal amplitude reduction due to too narrow-band filtering. For a narrow BW of 21.25 GHz, NRZ format requires 2 dB higher OSNR to achieve BER =10^{-3}.

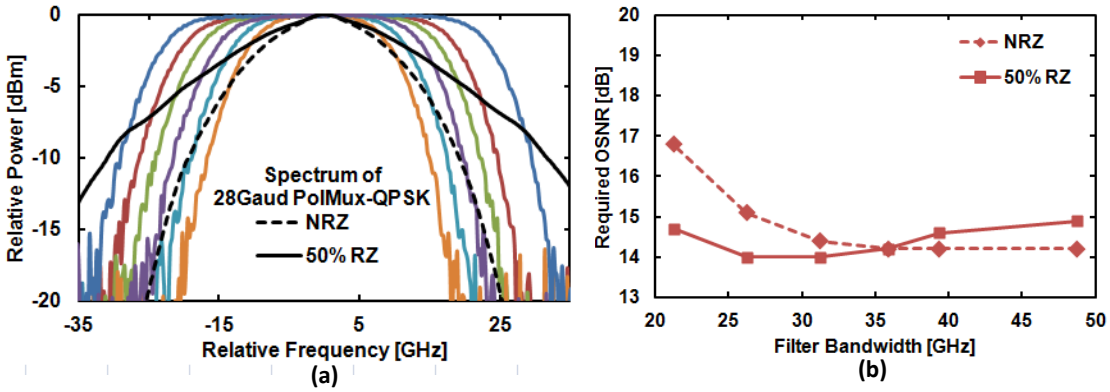

Figure 4.13. (a) Passband spectrum of WSS with different bandwidth. (b) Measured required OSNR for BER = 10^{-3} vs. filter bandwidth for 28-Gbaud NRZ and 50% RZ PDM-QPSK with BTB transmission.

The analysis of filtering effects is extended to the long-haul transmission with recirculating loop. Figure 4.14(a) and 4.14(b) show two configurations we investigated: a WSS is added in the beginning or in the middle of loop transmission, respectively. In Figure 4.14(a), the passband bandwidth of WSS is varied from 48.75 GHz to 21.25 GHz. The WSS bandwidth in Figure 4.14(b) is set 48.75 GHz, 40.5GHz, or 38 GHz; after 6-loops transmission, the three effective 3 dB bandwidths of cascaded WSSs are 37 GHz,

30 GHz and 27 GHz, respectively. The experimental results for these two configurations are shown in Figure 4.15. In Figure 4.15(a), the signal with RZ pulse shape also shows better filtering tolerance in linear transport regimes (launch power = -4 dBm). The relative advantage of the RZ format compared to NRZ format is enhanced when the transmission enters the nonlinear regime (launch power = +3 dBm). For example, with the filter bandwidth of 27 GHz (the dashed line shown in Figure 4.15(a)), the RZ format requires 2.4 dB and 1.7 dB less OSNRs to get BER = 10^{-3} than the NRZ format for +3 dBm and -4 dBm launch power cases, respectively. It shows that the RZ format has better tolerance not only to filtering effect, but also to fiber nonlinearity.

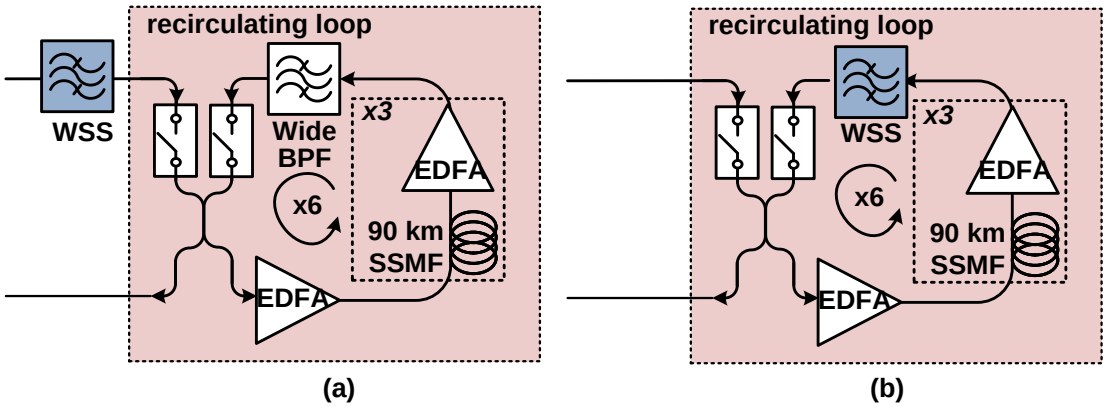

Figure 4.14. WSS in the (a) beginning of loop and (b) middle of loop.

Compared with Figure 4.15(a), Figure 4.15(b) shows the results for the setup having WSS in the middle of loop (Figure 4.14(b)). It is evident that the advantages for RZ format are decreased in both linear and nonlinear transport regimes. For the filter bandwidth of 27 GHz, the required OSNR benefit for RZ format is lessen by 0.9 dB. This is because the transmitted RZ signal loses its original pulse shape because of chromatic dispersion during propagation. Additionally, the investigation of the impact of fiber nonlinearity on passband narrowing is shown in Figure 4.15(c). Through a 21.25-GHz WSS put in the beginning of loop (Figure 4.14(a)), the OSNR penalty for NRZ PDM-

QPSK signal increases with launch power. Each OSNR penalty is relative to the required OSNR for BER =10^{-3} of each launch power with 50-GHz WSS. It can be seen that the passband narrowing effect is enhanced by fiber nonlinearity. The nonlinearity-enhanced passband effect is not obvious for RZ format because it has better tolerance to filtering effect and fiber nonlinearity.

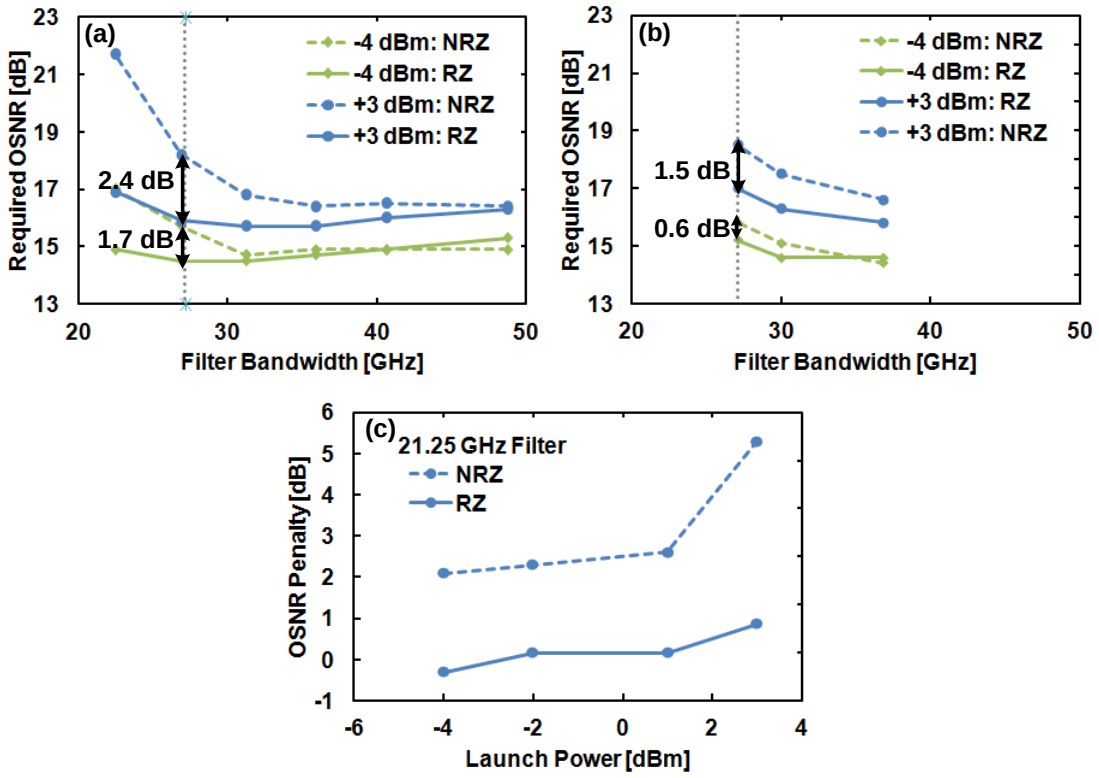

Figure 4.15. Required OSNR for BER = 10^{-3} vs. filter bandwidth for NRZ/RZ PDM-QPSK signal over 1,620km SSMF with -4 dBm and +3 dBm launch power: (a) WSS in the beginning of loop and (b) WSS in the middle of loop. (c) OSNR penalty vs. launch power for NRZ/RZ PDM-QPSK through 21.25-GHz WSS in the beginning of the loop.

Except for filtering narrowing, the frequency detuning is the other issue for the passband effects. Figure 4.16 summarizes the OSNR penalty for BER = 10^{-3} across different detuning values. Each OSNR penalty is relative to the setup without frequency detuning. For the filter bandwidth of 35.88 GHz, the OSNR penalties are below 1 dB for the frequency drift of ± 8 GHz and NRZ and RZ formats have the similar performances.

When the filter bandwidth is narrowed into 31.25 GHz, the NRZ format can tolerate 1.5 GHz less frequency drift at an required OSNR penalty of 1 dB than RZ format.

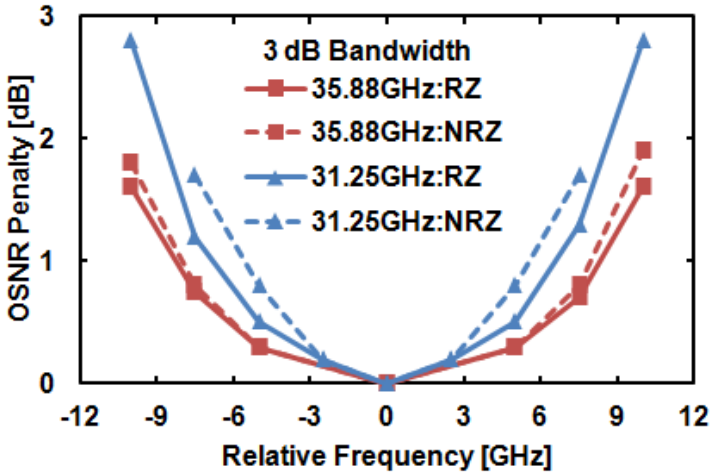

Figure 4.16. OSNR penalty for BER = 10^{-3} vs. relative frequency between passband and transmitting signal: 35.88-GHz and 31.25-GHz passband.

4.3.2 In-Band Crosstalk

Weighted Crosstalk

In-band crosstalk appears when the dropped channels are not perfectly blocked by the transmit port of WSS_2 in Figure 4.14. The power flow of in-band crosstalk addition is depicted in Figure 4.17. $S_i(f)$ is the primary channel of interest (add channel) with carrier frequency f_i and signal bandwidth f_1 (baud rate), $S_b(f)$ is the blocked (or dropped) channel, $H(f)$ is the response of blocking WSS filter that attenuates and shapes the dropping channel resulting in $X(f) = H(f) \cdot S_b(f)$. $X(f)$ is net crosstalk spectrum with carrier frequency f_x and signal bandwidth f_2.

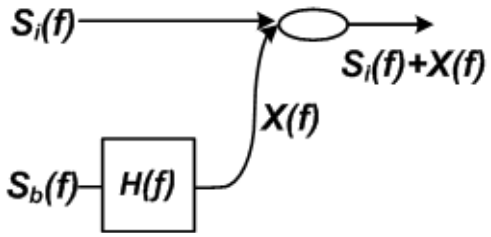

Figure 4.17. Signal power flow of in-band crosstalk.

Conventionally, crosstalk is the unweighted ratio of the total power in the interfering crosstalk signal to the total power in the primary signal

$$\frac{P_X}{P_i} = \frac{\int_{f_x-f_2}^{f_x+f_2} X(f)df}{\int_{f_i-f_1}^{f_i+f_1} S_i(f)df}. \tag{4.6}$$

It is assumed that the primary channel and crosstalk are both with phase modulation to match our 100G system (PDM-QPSK). We can write the total electric fields $E_{total}(t)$ as the sum of the primary channel $E_i(t)$ and crosstalk signal $E_x(t)$

$$E_{total}(t) = \overrightarrow{\rho_i}\sqrt{P_i}e^{j\left(2\pi f_i t+\theta_i(t)+\varphi_i(t)\right)} + \overrightarrow{\rho_x}\sqrt{P_x}e^{j\left(2\pi f_x t+\theta_x(t)+\varphi_x(t)\right)}, \tag{4.7}$$

where $\vec{\rho}$ expresses the polarization state, $\theta(t)$ is the phase information, and $\varphi(t)$ is the phase noise of source laser. The subscript *i* and *x* denote primary and crosstalk signal, respectively. The photocurrent of the output signal can be written as [111]

$$i(t) \propto P_i + P_x + 2\overrightarrow{\rho_i} \times \overrightarrow{\rho_x}\sqrt{P_i}\sqrt{P_x}cos(\varphi_t(t)), \tag{4.8}$$

$$\varphi_t(t) = \left\{2\pi(f_i - f_x)t + \left(\theta_i(t) - \theta_x(t)\right) + (\varphi_i(t) - \varphi_x(t))\right\}. \tag{4.9}$$

In Equation (4.8), the first two terms are primary and crosstalk signals, respectively. The third term is a beat noise that depends on the relative carrier frequency and phase

difference between primary channel and crosstalk. The beat term is the dominant noise, which contributes far larger than the crosstalk signal [111]. It can be seen that if the primary and the crosstalk signal have similar carrier frequency, the beat noise falls totally in-band. Conversely, with increasing carrier frequency disparity between primary and crosstalk signals, the beat signal falls further out of band. In other words, crosstalk signal power near the center of the channel of interest induces larger transmission penalties than equal power near the edges [39, 108].

A "weighting parameter" can account for the relative spectral content of the crosstalk and primary signal. The weighting function $W(f)$is proportional to the normalized spectral shape of the primary signal

$$W(f) = k \cdot \frac{S_i(f)}{\frac{1}{2f_1}\int_{f_i-f_1}^{f_i+f_1} S_i(f)df}, \tag{4.10}$$

where *k* represents the scaling factor. Thus, $X_w(f) = X(f) \cdot W(f)$ is the weighted crosstalk spectrum. After integration to determine the total power of the weighted crosstalk (P_{X_w}) and primary signal (P_i), we obtain the weighted crosstalk

$$\frac{P_{X_w}}{P_i} = \frac{\int_{f_i-f_1}^{f_i+f_1} X(f) \cdot W(f)df}{\int_{f_i-f_1}^{f_i+f_1} S_i(f)df}. \tag{4.11}$$

In order to make the weighted crosstalk yields the same result as the standard crosstalk when the primary signal has the same spectrum with the crosstalk signal, $S_i(f) = X(f)$, the scaling factor *k* should be defined as

$$k = av[\dot{S}_i(f)] \cdot \frac{\int_{f_i-f_1}^{f_i+f_1} S_i(f)df}{\int_{f_i-f_1}^{f_i+f_1} S_i(f)^2 df}. \quad (4.12)$$

Experimentally, the crosstalk signal is created by splitting off a fraction of the primary PDM-QPSK signal as shown in Figure 4.18(a). Following polarization scrambling and propagation through 3 km of SSMF are to reduce carrier coherence with the primary signal and eliminate bit-alignment penalties, and then the crosstalk signal is added back to the primary signal. A VOA enables control of the crosstalk signal level while the WSS employs Digital Micromirror Device (DMD) to control isolation level, and passband shape of the crosstalk channel. This method replicates the behavior of WSS_2, Figure 4.11, and is a completely general method of crosstalk generation.

A wide variety of filter shapes were explored in Figure 4.18(b). Filter 1 is the control case of no blocking, i.e. the interfering channel is an exact copy of the primary channel. Filter 2 is the blocked channel of a 50 GHz WSS with the max isolation level limited to 10 dB. Filter 3 is a 0.17 nm shift to longer wavelength of a standard block channel. Filter 4 is a "pinched" blocked channel, with approximately 0.2 nm of bandwidth and reduced isolation by 15 dB. Filter 5 shifts 0.17 nm to shorter wavelength and reduces the isolation level to 18 dB.

The combined signal is transmitted through an 8-span PtP link; three link configurations with different fiber types and dispersion maps are analyzed:

1. 90km SSMF spans with a matching -1530 ps/nm DSCM and -170 ps/nm of pre-compensation (100% inline compensation);
2. 80 km NZDSF spans with a matching -360 ps/nm DSCM and -170 ps/nm of pre-compensation (100% inline compensation);
3. 80 km NZDSF spans without DSCM or pre-compensation (0% inline compensation).

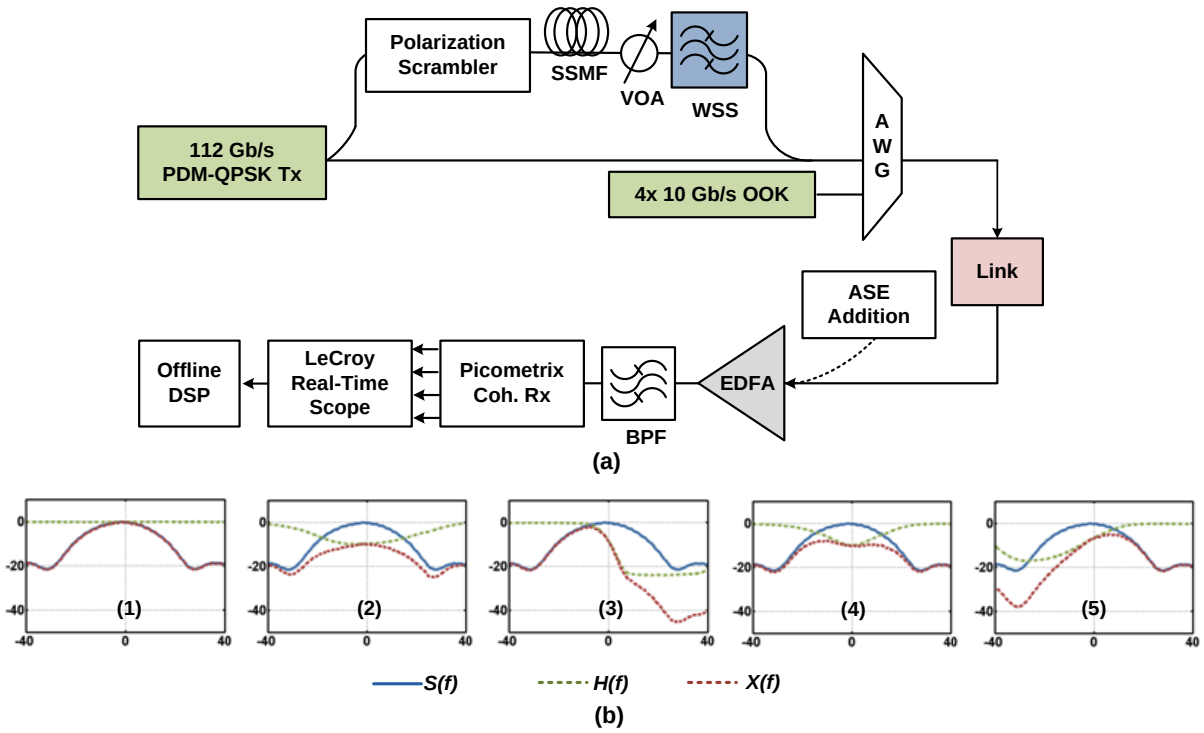

Figure 4.18. (a) Experimental network configuration of crosstalk addition. (b) Five chosen WSS filters: 112Gb/s PDM-QPSK spectrum *S(f)*, the measured filter shape *H(f)*, and the crosstalk spectrum after filtering *X(f)*.

For each filter shape, crosstalk power, and link configuration, we determined the OSNR penalty at BER = 10^{-3} with respect to the same link configuration without crosstalk in Figure 4.19. The PDM-QPSK channel launch power for all cases of Figure 4.19 is +2 dBm [117]. This penalty versus the unweighted crosstalk is shown in Figure 4.19(a)-(c). It is evident that the same OSNR penalty occurs for a wide range of unweighted crosstalk power depending strongly on spectral content. For example, 1dB penalty occurs for crosstalk powers that vary by at least 9dB.

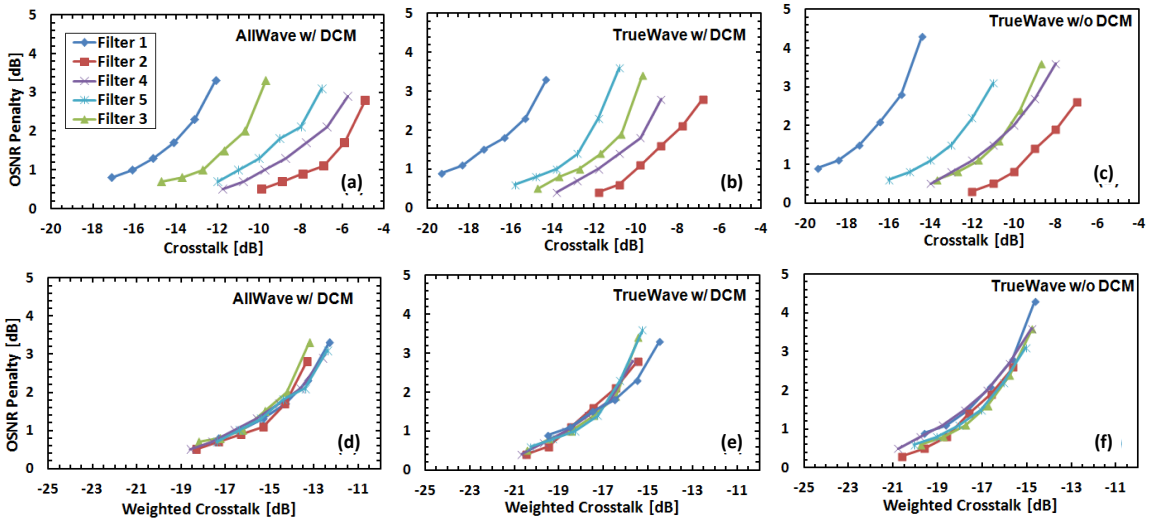

Figure 4.19. OSNR penalty for BER =10^{-3} vs. unweighted and weighted crosstalk in an 8-span PtP link of (a), (c) SSMF with matching DSCMs, (b), (d) NZDSF with matching DSCMs, and (c), (f) NZDSF without DSCMs. PDM-QPSK launch power in all cases was +2 dBm. The legend in (a) applies to all cases (a)-(f).

Particularly, in Figure 4.19(a)-(c), the crosstalk shaped by filter 1 induces the largest penalty per crosstalk power because the spectral power distribution of the crosstalk signal is identical to the primary channel. By contrast, filter 2 removes most crosstalk power at the center of the channel, where the majority of the channel power lies. The differences in relative penalties between the filter types 3, 4 and 5 occur due to slight variations in the filter shape between measurements.

However, with application of the weighting function, the weighted crosstalk yields very good OSNR penalty agreement for all five filter shapes as shown in Figure 4.19(d)-(f). It proves that the weighted crosstalk metric, accounting for the effect of the crosstalk spectral shape, can readily predict the OSNR penalty for any filter profile. These results also demonstrate excellent correlation between the weighted crosstalk and the OSNR penalty for diverse crosstalk scenarios in each optical network configurations [118].

Nonlinearity-Enhanced Crosstalk Effects

Next, we investigate the impact of fiber nonlinearities on crosstalk effects for a 100G system through a 8-span PtP link with two types of fiber; the results are shown in Figure 4.20(a). The setup of crosstalk addition is the same with Figure 4.18(a), and the generated crosstalk signal in this section is unshaped as the case with filter 1 shown in Figure 4.18(b). Each OSNR penalty shown in Figure 4.20(a) is also computed with respect to the required OSNR for BER = 10^{-3} of each configuration without crosstalk. The results shows the system with the SSMF link has ~2 dB more crosstalk tolerance than the one with the NZDSF link. It is likely due to the larger nonlinearity of NZDSF, which has smaller effective area as Table 4.1 shows. Furthermore, the system with the NZDSF link at +2 dBm launch power exhibits an 1.4-dB OSNR penalty at a crosstalk of -17 dB. However increasing launch power by 2 dB (+4 dBm) creates total 4 dB penalty. It can be seen that crosstalk-induced penalty depends nonlinearly on launch power. Since each penalty is relative to the same link configuration, we demonstrate an enhanced crosstalk penalty which is in addition to the nonlinear penalty observed in the absence of crosstalk.

The nonlinearity in the single-channel system, mainly from SPM, can also be enhanced by increasing the transmission length. As shown in Figure 4.20(b), the +2-dBm PDM-QPSK channel with 1620-km SSMF transmission can tolerate 0.5 dB less crosstalk at an OSNR penalty of 2 dB than the one with 720-km transmission, and when moving from +2 dBm to +3 dBm launch power, the tolerance decreases by 1.5 dB. Next, XPM effect is included by adding 10-Gb/s OOK channels to propagate with the 112-Gb/s PDM-QPSK signal. In Figure 4.20(c), the results demonstrate that XPM-induced crosstalk effects caused by -2-dBm side channels produce 3 dB less crosstalk tolerance at an OSNR penalty of 2 dB compared to the case with only SPM effect [119].

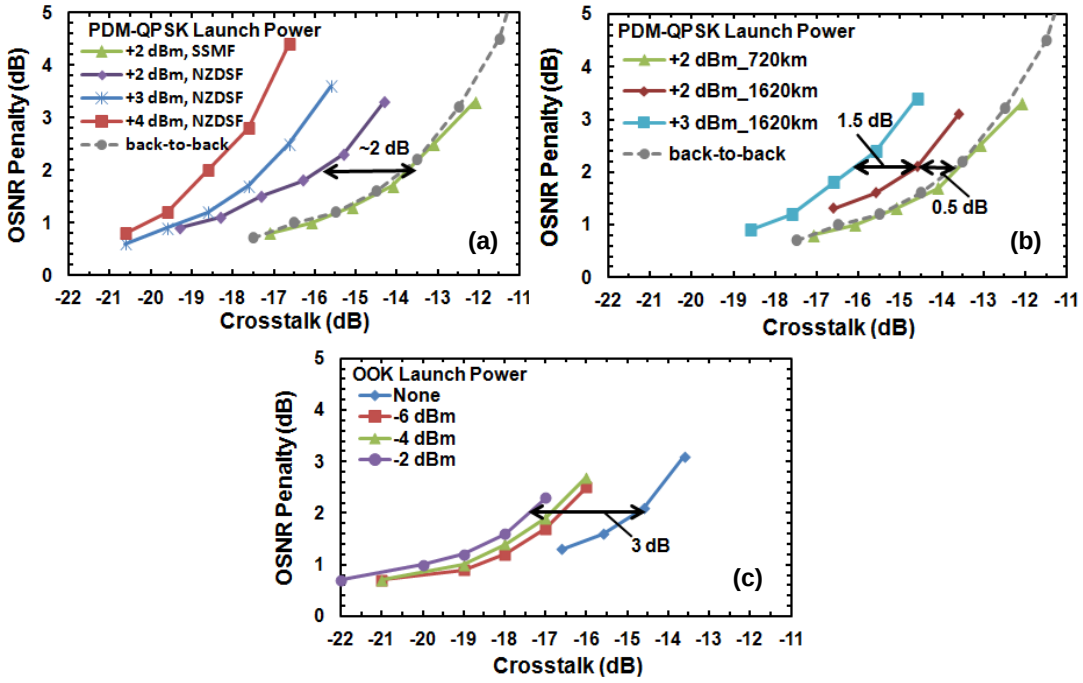

Figure 4.20. OSNR penalty for BER = 10^{-3} due to crosstalk for different fiber types, launch power and reaches: (a) single channel system with a 720-km SSMF or 640-km NZDSF link, (b) single channel system with a 720-km or 1,620-km SSMF link, and (c) hybrid system with a 1,620-km SSMF link and +2 dBm launch power for PDM-QPSK channel.

It is well known that if there is a strong signal propagates along a fiber, the small signal would experience gain due to the nonlinear interaction with strong signal. This phenomenon is called as parametric gain (PG) [120]. For example, there is a nonlinear parametric interaction of reference signal with in-band ASE noise, producing nonlinear phase and amplitude noise (NLPN, NLAN) [121]. Here, we consider the crosstalk generated by non-ideal ROADMs as the small signal.. The input to the fiber is assumed to be $A(0,t) = \sqrt{P_i} + N_i(t-\tau)$, where P_i is the power of CW primary signal, and $N_i(t) = \sqrt{P_x}\, exp(j(2\pi f_d t + \varphi_d(t))$) is the crosstalk signal with phase modulation format. The P_x, $\varphi_d(t)$, f_d, and τ are power, and relative phase, frequency, and delay with the primary channel. The generalized nonlinear Schrödinger equation is used to describe the slowly varying complex envelop of the optical field $A(z,t)$

$$\frac{\partial A}{\partial Z} = -\frac{\alpha}{2}A + \frac{j}{2}\beta_2 \frac{\partial^2 A}{\partial t^2} - j\gamma|A|^2 A, \tag{4.13}$$

where α is the fiber attenuation, β_2 the 2nd-order dispersion, and γ is a nonlinear coefficient of the fiber. The crosstalk signal after the first fiber span (length L) transmission is written in the frequency domain as [122]

$$\begin{aligned} N_1(\omega) = \Bigg\{ & N_i(\omega)\left[1 - j\frac{2\gamma P_i}{\alpha} + \frac{\gamma^2 {P_i}^2}{2\alpha(\alpha - j\beta_2\omega^2)}\right] \\ & - {N_i}^*(-\omega)\left[j\frac{\gamma P_i}{\alpha - j\beta_2\omega^2} + \frac{2\gamma^2 {P_i}^2}{\alpha(2\alpha - j\beta_2\omega^2)}\right]\Bigg\} \\ & \times exp(\frac{-\alpha}{2}L)exp(-\frac{j}{2}\beta_2 L\omega^2)exp(\frac{j}{2}D\omega^2)G, \end{aligned} \tag{4.14}$$

where G is the gain of an optical amplifier used to compensate for fiber loss and $exp(jD\omega^2/2)$ is for the fiber dispersion compensation. It is obvious that the crosstalk is amplified with fiber nonlinearity and signal power. If in a multi-channel system, P_i can be replaced by the power of neighboring channels, producing the interactions between crosstalk and adjacent channels through XPM and then generating cross-NLPN (X-NLPN). After *k*-span transmission and photodetection, the power distortion due to crosstalk is corresponding to $i(t,k)$

$$i(t,k) \propto \left|\sqrt{P_i}e^{-jk\frac{\gamma P_i}{\alpha}} + N_k(t-\tau)\right|^2 - P_i, \tag{4.15}$$

where $-k\gamma P_i/\alpha$ is the phase rotation due to SPM. The larger fiber nonlinearity induced by larger pump power P_i, more spans k, or larger nonlinear coefficient γ would increase the variance of $i(t,k)$ and then degrade the transmission performance. It explains why we observe the enhanced crosstalk-induced impairment in nonlinear transport regimes.

Importantly, crosstalk creates a larger penalty than ASE noise with an equivalent power. The simulated back-to-back BER vs. OSNR for the no-crosstalk cases are shown together with the BER vs. OSXR (optical signal-to-crosstalk ratio) for 20-dB and 9-dB $OSNR_{0.4nm}$ in Figure 4.21. For both OSNR and OSXR we use a resolution of 0.4 nm (~signal bandwidth) to achieve a fair comparison. In this case where the crosstalk has the same format and baud rate as the signal, the crosstalk with 20 dB $OSNR_{0.4nm}$ must be ~1.5 dB lower than white ASE noise to achieve the same performance. If we make the white ASE noise with the same spectral shape with the signal, which is called colored noise in Figure 4.21, the penalty is similar with the one induced by crosstalk. This result reveals that the noise penalty is spectrum dependent, and the crosstalk can be viewed as colored noise. In the nonlinear regime crosstalk penalties will also be larger than those created by equivalent power white noise.

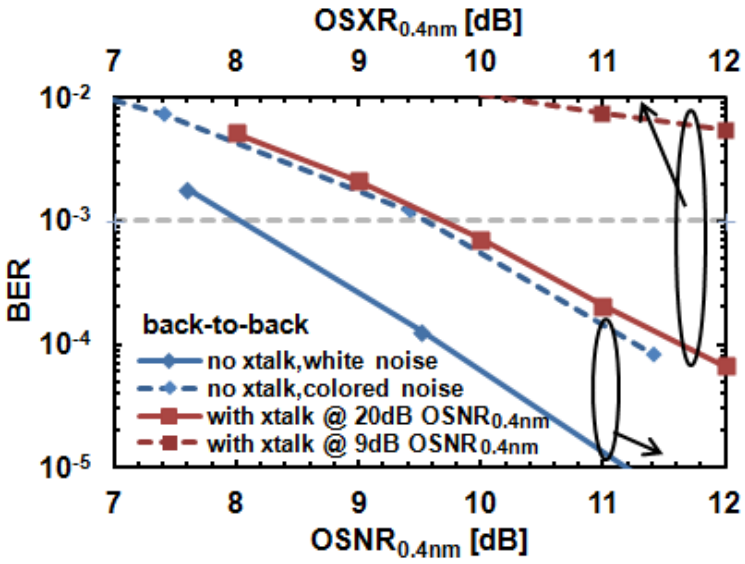

Figure 4.21. Simulated BER vs. OSNR for the no-crosstalk cases: white and colored noise from ASE, and BER vs. OSXR for the crosstalk-addition cases with 20-dB and 9-dB $OSNR_{0.4nm}$, all with back-to-back transmission (resolution = 0.4 nm).

The nonlinear crosstalk penalties are also evident in the observed dependence on total crosstalk-signal propagation distance. In simulation (R-Soft) we vary the crosstalk

addition position from from the beginning of link to after 540 km (6 spans), 1,080km (12 spans), or 1,620 km (18 spans) SSMF. Figure 4.22 plots the OSNR penalties at 12 dB crosstalk for different crosstalk addition positions, relative to those with crosstalk addition after 1,620 km. Specifically, Figure 4.22(a) shows the system with one PDM-QPSK channel, whereas Figure 4.22(b) shows the hybrid system with one PDM-QPSK and four 10G OOK channels. The results show that adding the crosstalk signal after longer transmission can mitigate crosstalk-induced OSNR penalties especially for the system operating in a high nonlinear regime (launch power = +4 dBm). In other words, the system with less nonlinear interaction between crosstalk and signals can achieve larger tolerance to crosstalk effects. If the crosstalk is distributed and then added into primary signal as Figure 4.23, the relative OSNR penalty, shown as the dashed lines in Figure 4.22(b), is less than the one with crosstalk added in the beginning of transmission but larger than other crosstalk addition positions. The total power of distributed crosstalk is equal to the one of crosstalk added in the one position.

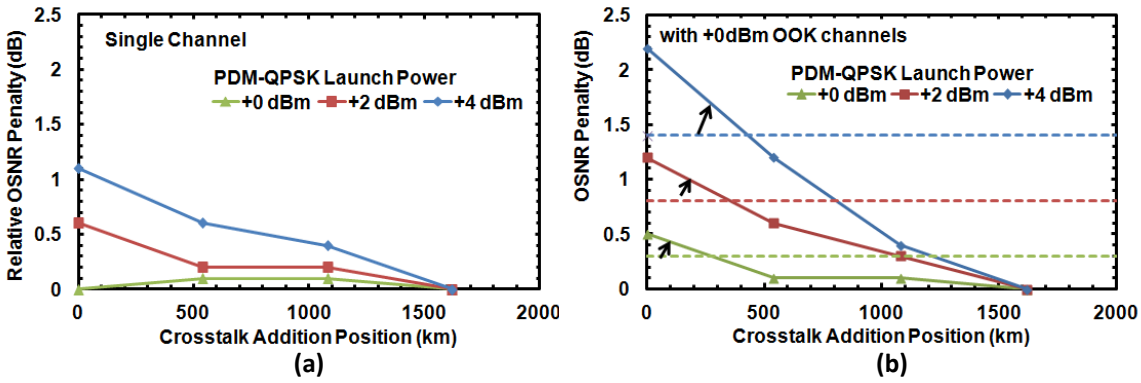

Figure 4.22. Relative OSNR penalty for BER = 10^{-3} vs. crosstalk addition position for (a) the system with a single PDM-QPSK channel and (b) the hybrid system.

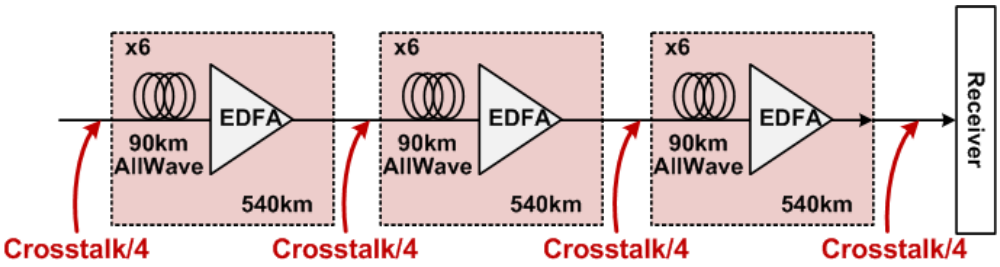

Figure 4.23. Distributed crosstalk addition setup.

4.4 Chapter Summary

This chapter presents the designs of transmitter, receiver and transmission link of our 112-Gb/s PDM-QPSK testbed. Based on this system, optimum and robust dispersion maps are experimentally determined from a range of pre- and inline-dispersion compensation in a system with one 56-Gb/s single-pol RZ-DQPSK channel and two 12-Gb/s OOK aggressor channels through the 8-span PtP link. The results show that the scheme with RDPS of +153 ps/nm is insensitive to pre-comp, and with less than 1 dB required OSNR difference at BER = 10^{-3} between -2 and +4 dBm launch power. Moreover, the most robust dispersion map uses the smaller pre-comp of -170 ps/nm. While the absolute OSNR requirements would not be the same, it seems likely that 112-Gb/s PDM RZ-DQPSK would follow a similar trend since the baud rate is the same.

Some significant impairments for ROADM-enabled 100G networks are also reviewed in this chapter. Passband effects include passband narrowing and frequency detuning. Performance degradation generated by passband effects will limit the number of ROADM deployed in DWDM systems. Experimental results demonstrate that RZ format is preferred over NRZ for due to lower impact from filtering and fiber nonlinear effects. For a single 112-Gb/s PDM-QPSK channel through a 27-GHz passband set before the 1620-km SSMF transmission, RZ format outperforms NRZ by ~2.4 dB in required OSNR for BER = 10^{-3} in nonlinear transport regime. However, the advantages of RZ format would be reduced by fiber dispersion, which distorts the RZ pulse shape.

Accurate estimation of in-band crosstalk-induced penalties, generated by non-ideal ROADMs, is required. We experimentally investigated the efficacy of using a weighted crosstalk parameter to predict OSNR transmission penalties in 112-Gb/s PDM-QPSK systems. Experimental results reveal that the weighted crosstalk technique with a 2×1 WSS yields excellent correlation with OSNR penalties regardless of spectral shape, bandwidth, and wavelength offset of crosstalk signals in both linear and nonlinear transport regimes. This technique should be applicable with multiple crosstalk sources such as multi-degree ROADMs as well. In addition, having a reliable method to estimate crosstalk-induced penalties is more important for the system with higher-order modulation format. Reference [123] shows that the impact of in-band crosstalk for higher-level QAM formats is more severe: 16-QAM and 64-QAM format have 8 dB and 16 dB less crosstalk tolerance at an OSNR penalty of 1 dB compared to QPSK format, respectively.

Furthermore, we investigated the impact of fiber nonlinearities on the crosstalk-induced penalty. Experimental results demonstrate enhanced-crosstalk penalties through parametric gain analogous to those observed with ASE noise. Simulation results demonstrate that the crosstalk penalty increases with increasing interaction distance and is generally larger than that caused by ASE of equivalent power.

Each of the penalties investigated become more problematic as WDM systems move to tighter channel spacing and higher order modulation formats. The results here demonstrate that these impairments can be readily predicted with proper experimental and simulation efforts.

CHAPTER 5

CONCLUSIONS

Rapid movement to the information age makes the bandwidth demands on wireless and wired line keep increasing. Facing more and more high-bandwidth applications, optical fiber is a better transmission medium over coaxial cables owing to its broad bandwidth, low loss, light weight, and low electromagnetic interference. The main contribution of this dissertation is the comprehensive consideration of both wired and wireless communications over optical systems, enabling transports of high-speed metro core network and last mile, last meter access network. In this chapter, the summaries of RoF technology at mmW band for high-capacity wireless applications are shown in Section 4.1. Section 4.2 concludes the research we have done in the 100G optical transport system for the next-generation backbone network. The recommendations of further research for the two works are also presented in this chapter.

5.1 Radio-Over-Fiber Technology for High-Capacity Wireless Applications

With the growing bandwidth demand for the last mile and last meter, RoF technology at mmW band been viewed as the most promising solution to provide ubiquitous multi-gigabit wireless services with simplified and cost-effective BSs and low-loss, bandwidth-abundant fiber optic networks. In such a system, the technical challenges on optical mmW generation, transmission impairments compensation, multi-band generation, and full-duplex transmission are vital for the successful deployment in the future. Chapter 2 first concludes the general methods of optical mmW generation, and summarizes their advantages and disadvantages. Then the theoretical characterization of optical mmW generation based on a single MZM under different configurations are discussed; the results show the OCS format has benefits of the lowest occupied

bandwidth and the most relaxed RF frequency. Moreover, two optical frequency-doubled mmW generation methods based on external phase modulation are proposed and experimentally demonstrated their simplicity, reliability, and cost-efficiency compared with existing schemes. For the transmission impairments compensation, the numerical analysis suggests that a RoF system with the OSSB+C format is more resistant to the effects with regard to propagation through fiber with chromatic dispersion and then achieve longer transmission distance. Another method based on the remote OCS also experimentally realized a 125-km SSMF transmission for a 60-GHz RoF system. To achieving successful full-duplex transmission, the structures of numerous BSs in mmW RoF systems can be simplified by lightwave centralization technique, which is categorized into DL wavelength reuse and remote carrier delivery for UL. The penalties induced by backscattering signals for the bi-directional transmission over a single fiber can also be mitigated by the appropriate wavelength assignments for both directions.

Owing to ultra-wide bandwidth and protocol transparent characteristics, a RoF system can be utilized to simultaneously deliver wired and multi-band wireless services for both fixed and mobile users. In Chapter 3, the proposed multi-band 60-GHz RoF systems are categorized in three types: mmW with baseband and MW, mmW with commercial wireless services in low RF regions, and 60-GHz sub-bands; they are designed for different applications. The advantages and disadvantages of these multi-band generation technologies are compared based on experimental results. The lightwave centralization, frequency doubling/tripling, long transmission distance, high-level modulation format are realized by our novel techniques. Furthermore, the efficient integration of the new 60-GHz optical-wireless system with the commercial wireless services in low RF regions are accomplished by our proposed converged all-band 60-GHz system, which is based on 60-GHz sub-bands distribution and band-mapping concept. As a result, this proposed scheme not only provides multi-gigabit data and video distributions but also has backward compatibility to legacy wireless services.

For the mmW RoF system, there are still many issues that need to be identified and studied in the future. The full-duplex demonstration to prove real-traffic capability is necessary for future research; it should focus on the design of the E/O conversion and down-conversion of uplink transmission at BSs. Except for physical layer, the MAC layer design is also very important for a successful, practical RoF system, which will be a multi-point network. Future work should also includes a 60-GHz band distribution plan for the converged all-band mmW RoF system proposed in section 3.4.2. This system finally can be applied to in-door, in-building networking, which only needs 60-GHz antennas for all-band signals broadcasting. Extending to E-band frequencies (71-86GHz) based on the developed technologies in this work is another promising research direction.

5.2 100G Long-Haul Optical Transport System

With the increasing of data over voice services, the transport of 100G optical Ethernet is deployed to handle the capacity requirements of next-generation core network. Different modulation formats have been developed and investigated. Among all of them, the most potential candidate for the 100G system is PDM-(D)QPSK, which can increase the spectral efficiency and tolerance to CD and PMD. In Chapter 4, each component of a long-haul 100G PDM-(D)QPSK system is comprehensively discussed. The experimental results indicate that careful dispersion management can effectively increase DQPSK channel tolerance to nonlinear transmission impairments. A larger RDPS offers a more significant difference in group delay between the DQPSK and adjacent 10G OOK channels, decreasing the magnitude of XPM effect on the DQPSK channel.

Furthermore, two key transmission impairments for long-haul ROADM-enabled 112-Gb/s PDM-QPSK networks are experimentally and numerically analyzed: passband and in-band crosstalk effects We consider passband narrowing and frequency detuning for NRZ/RZ formats, quantified in terms of the required OSNR for BER = 10^{-3}. The RZ

pulse shape is shown to offer better tolerance to filtering and fiber nonlinearity compared to NRZ. Experimental results also reveal that the distortion induced by fiber dispersion reduces the benefits of RZ. Furthermore, a weighted method was investigated to quantify the OSNR penalty of in-band crosstalk that accounts for the varying spectral content. Experimentally evaluated penalties for widely varying crosstalk spectral content are shown to be readily predetermined based on the crosstalk spectral content and power, which are dramatically diverse with the conventional crosstalk metric instead. Lastly, we demonstrate experimentally and in simulation a nonlinearity-enhanced crosstalk penalty that results from the nonlinear parametric interaction between primary signal and crosstalk over long-distance transmission. It is a more critical transmission limitation over the nonlinear interactions between signal and ASE noise. Therefore, the research results related to the dispersion map and ROADM-induced impairments can be applied to the design and performance estimation of future 100G optical transport networks.

In order to generate higher line rate (> 112 Gb/s), the higher baud rate (> 28 Gbaud), multi-level modulation format (such as 16 QAM), and multi-subcarriers scheme [124] will be applied in the future core network; the structure design and performance evaluation of these new systems will need to be addressed. More DSP studies in digital domain to implement propagation impairment compensation are another promising research area.

REFERENCES

[1] "Internet usage and world population statistics", www.internetworldstats.com/stats.htm (Accessed June 30, 2010).

[2] Cisco Visual Networking Index: Forecast and Methodology, 2009–2014.

[3] P. J. Winzer, "Beyond 100G Ethernet," *IEEE Commun. Magazine,* vol. 48, no. 7, pp. 26-30, July 2010.

[4] Ericsson, "Annual Report 2010", www.ericsson.com/res/investors/docs/2010/ericsson_ar_2010_en.pdf (Accessed March 2011).

[5] S. Dhawan, "Analogy of promising wireless technologies on different frequencies Bluetooth, Wi-Fi and WiMAX," *IEEE 2nd International Conference on Wireless Broadband and Ultra Wideband Communications*, pp. 1-7, Aug. 2007.

[6] P. Smulders, "Exploiting the 60 GHz band for local wireless multimedia access: prospects and future directions," *IEEE Commun. Magazine*, vol. 40, no. 1, pp. 140-147, Jan. 2002.

[7] H.T. Friis, "A note on a simple transmission formula," *IRE*, vol.34, pp. 254, 1946.

[8] J. Laskar, S. Pinel, D. Dawn, S. Sarkar, B. Perumana and P. Sen, "The Next Wireless Wave is a Millimeter Wave," *Micro. J.*, vol. 50, no. 8, pp. 22-34, 2006.

[9] R. C. Daniels and R. W. Heath, "60-GHz wireless communications: emerging requirements and design recommendations," *Vehicular Technology Magazine, IEEE*, vol. 2, pp. 41-50, 2007.

[10] S.-K. Yong, "Introduction to 60 GHz," *Wiley & Sons, Ltd*., 2011.

[11] IEEE 802.15.3c Working Group, www.ieee802.org/15/pub/TG3c.html.

[12] "WirelessHD™ 1.0 Specification", www.wirelesshd.org/.

[13] Standard ECMA-387, "High rate 60 GHz PHY, MAC and HDMI PAL", Dec. 2008 - under ballot in JTC 1 as ISO/IEC DIS 13156.

[14] IEEE 802.11ad Task Group, www.ieee802.org/11/Reports/tgad_update.htm.

[15] "Wireless Gigabit Alliance (WiGig) White Paper 1.1 Specification", wirelessgigabitalliance.org/specifications/ (Accessed July 2010).

[16] G.-K. Chang, A. Chowdhury, Z. Jia, H.-C. Chien, M.-F. Huang, J. Yu, and G. Ellinas, "Key technologies of WDM-PON for future converged optical broadband access networks," *Journal of Optical Communication and Network*, vol. 1, no. 4, pp. C35-C50, 2009.

[17] A. Koonen and L. Garcia, "Radio-over-mmf techniques-part II: microwave to millimeter-wave systems," *J. Lightw. Technol*., vol. 26, no. 15, pp. 2396-2408, 2008.

[18] A. Chowdhury, H.-C. Chien, Y.-T. Hsueh, and G.-K. Chang, "Advanced system technologies and field demonstration for in-building optical-wireless network with integrated broadband services," *J. Lightw. Technol*., vol. 27, no. 22, pp. 1920-1927, 2009.

[19] Z. Jia, J. Yu, G. Ellinas, and G.-K. Chang, "Key enabling technologies for optical-wireless networks: optical millimeter-wave generation, wavelength reuse, and architecture," *J. Lightw. Technol*., vol. 25, pp. 3452-3471, 2007.

[20] J. Olmos, T. Kuri, and K. Kitayama, "Dynamic reconfigurable WDM 60-GHz millimeter-waveband radio-over-fiber access network: architectural considerations and experiment," *J. Lightw. Technol.*, vol. 25, no. 11, pp. 3374-3380, Nov. 2007.

[21] A. J. Seeds and K. J. Williams, "Microwave photonics," *J. Lightw. Technol*., vol. 24, no. 12, pp. 4628-4641, 2006.

[22] C. Lim, A. Nirmalathas, D. Novak, R. Waterhouse, and G. Yoffe, "Millimeter-wave broadband fiber-wireless system incorporating baseband data transmission over fiber and remote LO delivery", *J. Lightw. Technol*., vol.18, no. 10, pp. 1355-1363, Oct. 2000.

[23] A. Nirmalathas, C. Lim, D. Novak, and R.B. Waterhouse, "Progress in millimeter-wave fiber-radio access networks", *Annals of Telecommunications*, vol. 56, no.1-2, pp. 1-12, Jan. 2001.

[24] K. Kitayama, A. Stohr, T. Kuri, R. Heinzelmann, D. Jager, and Y. Takahashi, "An approach to single optical component antenna base stations for broad-band millimeter-wave fiber-radio access systems," *IEEE Trans. Microw. Theory Tech*., vol. 48, no. 12, pp. 2588–2595, Dec. 2000.

[25] P. Dolet and L. Duplessis, "100G Ethernet and OTU4 testing challenges, from the lab to the field," *IEEE Commun. Magazine*, vol. 48, no. 7, pp. 78-82, July 2010.

[26] X. Zhou et al., "Transmission of 32 Tb/s capacity over 580 km using RZ-shaped PDM-8QAM modulation format and cascaded multi-modulus blind equalization algorithm," *J. Lightw. Technol*., vol. 28, no. 4, 2010, pp. 456–65.

[27] J. Yu et al., "17 Tb/s (161 × 114 Gb/s) PolMux-RZ-8PSK transmission over 662 km of ultra-low loss fiber using C-band EDFA amplification and digital coherent detection," *ECOC 2008*, PDP19.

[28] A. H. Gnauck et al., "10 × 112 Gb/s PDM 16-QAM transmission over 630km of fiber with 6.2-b/s/Hz spectral efficiency," *OFC/NFOEC 2009*, PDPB8.

[29] A. Sano et al., "No-guard-Interval coherent optical OFDM for 100 Gb/s long-haul WDM transmission," *J. Lightw. Technol.*, vol. 27, no. 16, pp. 3705 – 3713, Jul. 2009.

[30] S. Chandrasekhar, X. Liu, B. Zhu, and D. W. Peckham, "Transmission of a 1.2 Tb/s 24-Carrier no-guard-interval coherent OFDM super-channel over 7200km of ultra-large-area fiber," *ECOC 2009,* PD 2.6.

[31] C. R. S. Fludger, et al., "Coherent equalization and POLMUX-RZ-DQPSK for robust 100-GE transmission," *J. Lightw. Technol.*, vol. 26, no. 1, pp. 64-72, Jan.1, 2008.

[32] S. Chandrasekhar and X. Liu, "Impact of channel plan and dispersion map on hybrid DWDM Transmission of 42.7-Gb/s DQPSK and 10.7-Gb/s OOK on 50-GHz grid," *IEEE Photon. Technol. Lett*., vol. 19, pp. 1801-1803, 2007.

[33] L. D. Coelho, O. Gaete, E.-D. Schmidt, B. Spinnler, and N. Hanik, "Global optimization of RZ-DPSK and RZ-DQPSK systems at various data rates," *OFC/NFOEC 2009*, JThA39.

[34] J.-X. Cai et al., "20 Tbit/s capacity transmission over 6,860 km," *OFC/NFOEC 2011*, PDPB4.

[35] M. Salsi et al., "155 × 100 Gb/s Coherent PDM-QPSK Transmission over 7,200km," *ECOC 2009*, PD2.5.

[36] S. Tibuleac and M. Filer, "Transmission impairments in DWDM networks with reconfigurable optical add-drop multiplexers," *J. Lightw. Technol*., vol. 28, no. 4, pp. 557-568, Feb., 2010.

[37] C. Qingjiang, F. Hongyan, and S. Yikai, "Simultaneous generation and transmission of downstream multiband signals and upstream data in a bidirectional radio-over-fiber system," *IEEE Photon. Technol. Lett*., vol. 20, no. 3, pp. 181-183, Feb. 2008.

[38] K. Ikeda, T. Kuri, and K. Kitayama, "Simultaneous three-band modulation and fiber-optic transmission of 2.5-Gb/s baseband, microwave-, and 60-GHz-band signals on a single wavelength," *J. Lightw. Technol*., vol. 21, no. 12, pp. 3194-3202, Dec. 2003.

[39] J. J. V. Olmos, T. Kuri, and K.-i. Kitayama, "Reconfigurable radio-over-fiber networks multiple-access functionality directly over the optical layer," *J. Lightw. Technol*., vol. 58, no. 11, pp. 3001-3010, Nov. 2010.

[40] Z. Jia, J. Yu, Y.-T. Hsueh, A. Chowdhury, H.-C. Chien, J. A. Buck, and G.-K. Chang, "Multiband signal generation and dispersion-tolerant transmission based on photonic frequency tripling technology for 60-GHz radio-over-fiber systems," *IEEE Photon. Technol. Lett*., vol. 20, pp. 1470-1472, 2008.

[41] S.-H. Fan, H.-C. Chien, Y-T Hsueh, A. Chowdhury, J. Yu, and G.-K. Chang, "Simultaneous transmission of wireless and wireline services using a single 60-GHz radio-over-fiber channel by coherent subcarrier modulation," *IEEE Photon. Technol. Lett.*, vol. 21, no. 16, pp. 1127-1129, Jul. 2009.

[42] G. Qi, J. Yao, J. Seregelyi, S. Paquet, and C. Bélisle, "Optical generation and distribution of continuously tunable millimeter-wave signals using an optical phase modulator," *J. Lightw. Technol*., vol. 23, no. 9, pp. 2687–2695, Sep. 2005.

[43] C.-T. Lin, S.-P. Dai, J. Chen, P. T. Shih, P.-C. Peng, and S. Chi, "A novel direct detection microwave photonic vector modulation scheme for radio-over-fiber system," *IEEE Photon. Technol. Lett*., vol. 20, no. 13, pp. 1106-1108, July 2008.

[44] P.-T. Shih, C.-T. Lin, H.-S. Huang, Wen.-J. Jiang, J. Chen, A. Ng'oma, M. Sauer, and S. Chi, "13.75-Gb/s OFDM signal generation for 60-GHz RoF system within 7-GHz license-free band via frequency sextupling," *ECOC 2009*, 4.5.4.

[45] Z. Cao, L. Zou, L. Chen, and J. Yu, "Impairment mitigation for a 60 GHz OFDM radio-over-fiber system through an adaptive modulation technique," *IEEE J. of Opt. Comm. and Netw*., vol. 3, no. 9, pp. 758-766, Sept. 2011.

[46] C. Liu et al., "Optimization of vector signal delivery over double-sideband carrier-suppressed optical millimeter-waves through dc coupling," *IEEE Photon. Technol. Lett*., vol. 23, no. 12, pp. 789-791, Apr. 2011.

[47] C. Lim and A. Nirmalathas, "Optical-Wireless Integration: Technologies for Physical Layer Networking," *WCNCW 2010*, pp. 1-5, 2010.

[48] Z. Jia, J. Yu, L. Zong, G.-K. Chang, "Transport of 8x2.5-Gb/s wireless signals over optical millimeter wave through 12 straight-line WSSs and 160-km fiber for DWDM metro networks," *OFC/NFOEC 2008*, OMO3.

[49] M. Jianxin, J. Yu, Y. Chongxiu, X. Xiangjun, Z. Junying, and L. Chen, "Fiber dispersion influence on transmission of the optical millimeter-waves generated using LN-MZM intensity modulation," *J. Lightw. Technol*, vol. 25, pp. 3244-3256, 2007.

[50] G. H. Smith, D. Novak, Z. Ahemd, "Overcoming chromatic-dispersion effects in fiber-wireless systems incorporating external modulators," *IEEE Trans. on Microw. Theory and Tech*., vol. 45, no. 8, pp. 1410-1415, 1997.

[51] C. Lim, A. Nirmalathas, K.-L. Lee, D. Novak, and R. Waterhouse, "Intermodulation distortion improvement for fiber-radio applications incorporating OSSB+C modulation in an optical integrated-access environment," *J. Lightw. Technol*., vol. 25, no.6, pp.1602-1612, June 2007.

[52] A. Wiberg, B. E. Olsson, P. O. Hedekvist, and P. A. Andrekson, "Dispersion-tolerant millimeter-wave photonic link using polarization-dependent modulation," *J. Lightw. Technol*., vol. 25, no.10, pp. 2984-2991, Oct. 2007.

[53] U. Gliese, S. Nørskov, and T. N. Nielsen, "Chromatic dispersion in Fiber-Optic Microwave and millimeter-wave links," *IEEE Trans. on Microw. Theory and Tech*., vol. 44, no. 10, pp. 1716-1724, Oct. 1996.

[54] Z. Jia, J. Yu, G. Ellinas, G.-K. Chang, "A novel full-duplex wavelength-reuse optical-wireless architecture with directly modulated SOA as upstream colorless amplified modulator," *OFC/NFOEC 2007*, OThM2.

[55] T. Ismail et al., "Transmission of 37.6-GHz QPSK wireless data over 12.8-km fiber with remote millimeter-wave local oscillator delivery using a bi-directional SOA in a full-duplex system with 2.2-km CWDM fiber ring architecture," *IEEE Photon. Technol. Lett.*, vol. 17, no. 9, pp. 1989-1991, Sep. 2005.

[56] J. Yu, Z. Jia, T. Wang, G.-K. Chang, "A novel radio-over-fiber configuration using optical phase modulator to generate an optical mmW and centralized lightwave for uplink connection," *IEEE Photon. Technol. Lett.*, vol.19, no.3, pp. 140-142, Feb. 2007.

[57] L. Chen, H. Wen and S. Wen, "A radio-over-fiber system with a novel scheme for millimeter-wave generation and wavelength reuse for up-link connection", *IEEE Photon. Technol. Lett.*, vol. 18, no.19, pp. 2056-2058, 2006.

[58] D. Wake, C. R. Lima, and P. A. Davies, "Transmission of 60-GHz signals over 100 km of optical fiber using a dual-mode semiconductor laser source," *IEEE Photon. Technol. Lett.*, vol. 8, no. 4, pp. 578-580, 1996.

[59] J. Yu, Z. Dong, W. Jian, M.-F. Huang, Z. Jia, X. Xin, G.-K. Chang and T. Wang, "All-optical up-conversion 10-Gb/s signal in 60-GHz ROF system using 2-m Bismuth Oxide-based fiber," *OFC/NFOEC 2010*, OTu06.

[60] I. González Insua, D. Plettemeier, and C. G. Schäffer, "Simple remote heterodyne radio-over-fiber system for gigabit per second wireless access," *J. Lightw. Technol.*, vol. 28, no.16, pp. 2289-2295, Oct. 2010.

[61] J. Liu et. Al, "Efficient optical millimeter-wave generation using a frequency-tripling Fabry–Pérot laser with sideband injection and synchronization" *IEEE Photon. Technol. Lett.*, vol. 23, no. 18, pp. 1325-1328, June 2011.

[62] L. A. Johansson, and A. J. Seeds, "Millimeter-wave modulated optical signal generation with high spectral purity and wide-locking using a fiber-integrated optical injection phase-lock loop," *IEEE Photon. Technol. Lett.*, vol. 12, no. 6, pp. 690-692, June 2000.

[63] H.-C. Chien, Y.-T. Hsueh, A. Chowdhury, J. Yu, and G.-K. Chang, "Optical millimeter-wave generation and transmission without carrier suppression for single- and multi-band wireless over fiber applications," *J. Lightware Technol.*, vol. 28, no. 16, pp. 2230-2237, Aug. 2010.

[64] Y.-T. Hsueh, H.-C. Chien, A. Chowdhury, J. Yu, and G.-K. Chang, "Performance assessment of radio links using millimeter-wave over fiber technology with carrier suppression through modulation index enhancement," *IEEE/OSA J. of Opt. Comm. and Netw.*, vol. 3, no. 3, pp. 254-258, Mar. 2011.

[65] Y.-T. Hsueh, H.-C. Chien, Z. Jia, A. Chowdhury, J. Yu, and G.-K. Chang, "8×2.5-Gb/s, 60-GHz radio-over-fiber access network with 125-km extended reach using remote optical carrier suppression," *IEEE/LEOS 2008*, ThN3.

[66] M. O. v. Deventer, *Fundamentals of Bidirectional Transmission Over a Single Optical Fiber*. Boston, MA: Kluwer, 1996.

[67] C. W. Chow, G. Talli, and P. D. Townsend, "Rayleigh noise reduction in 10-Gb/s DWDM-PONs by wavelength detuning and phase-modulation-induced spectral broadening," *IEEE Photon. Technol. Lett.*, vol. 19, no. 6, pp. 423-425, Mar. 2007.

[68] T. Yoshida, S. Kimura, H. Kimura, K. Kumozaki, and T. Imai, "A new single-fiber 10-Gb/s optical loopback method using phase modulation for WDM optical access network," *J. Lightw. Technol.* , vol. 24, no. 2, pp. 786–796, 2006.

[69] C. W. Chow, G. Talli, and P. D. Townsend, "Rayleigh noise reduction in 10-Gb/s DWDM-PONs by wavelength detuning and phase-modulation-induced spectral broading," *IEEE Photon. Technol. Lett.*, vol. 19, no. 6, pp. 423–425, Mar. 2007.

[70] J. A. Lazaro, C. Arellano, V. Polo, and J. Prat, "Rayleigh scattering reduction by means of optical frequency dithering in passive optical networks with remotely seeded ONUs," *IEEE Photon. Technol. Lett.*, vol. 19, no. 2, pp. 64–66, Jan. 2007.

[71] H. H. Lin, C. Y. Lee, S. C. Lin, S. L. Lee, and G. Keuser, "WDM-PON systems using cross-remodulation to double network capacity with reduced Rayleigh scattering effects," *OFC/NFOEC 2008*, OTuH6.

[72] A. Chowdhury, H.-C Chien, M.-F Huang, J. Yu, and G.-K. Chang, "Rayleigh backscattering noise-eliminated 115-km long-reach bidirectional centralized WDM-PON with 10-Gb/s DPSK downstream and remodulated 2.5-Gb/s OCS-SCM upstream signal," *IEEE Photon. Technol. Lett.*, vol. 20, no. 24, pp. 2081–2083, Dec. 2008.

[73] A. Yeniau, J.-M. Delavaux, and J. Toulouse, "Spontaneous and stimulated Brillouin scattering gain spectra in optical fibers," *J. Lightw. Technol.* , vol. 20, no. 8, pp. 1425–1432, 2002.

[74] M. Sauer, A. Kobyakov, and A. B. Ruffin, "Radio-over-fiber transmission with mitigated stimulated Brillouin scattering," *IEEE Photon. Technol. Lett.*, vol. 19, no. 19, pp. 1487–1489, Oct. 2007.

[75] R. Ramaswami, and K. N. Sivarajan, *Optical Networks: A Practical Perspectiv*e. San Mateo, CA: Morgan Kaufmann, 2002.

[76] C. Qingjiang, F. Hongyan, and S. Yikai, "Simultaneous generation and transmission of downstream multiband signals and upstream data in a bidirectional radio-over-fiber system, " *IEEE Photon. Technol. Lett.*, vol. 20, no. 3, pp. 181-183, Feb. 2008.

[77] K. Ikeda, T. Kuri, and K. Kitayama, "Simultaneous three-band modulation and fiber-optic transmission of 2.5-Gb/s baseband, microwave-, and 60-GHz-band signals on a single wavelength," *J. Lightw. Technol.*, vol. 21, no. 12, pp. 3194-3202, Dec. 2003.

[78] J. J. V. Olmos, T. Kuri, and K.-i. Kitayama, "Reconfigurable radio-over-fiber networks multiple-access functionality directly over the optical layer," *J. Lightw. Technol*., vol. 58, no. 11, pp. 3001-3010, Nov. 2010.

[79] Y.-T. Hsueh, Z. Jia, H.-C. Chien, A. Chowdhury, J. Yu, and G.-K. Chang, "A novel bidirectional 60-GHz radio-over-fiber scheme with multiband wignal generation *using* a single intensity modulator," *IEEE Photon. Technol. Lett.*, vol. 21, no. 18, pp. 1338-1340, Sept. 2009.

[80] R. Llorente, S. Walker, and I. T. Monroy, "Triple-play and 60-GHz radio-over-fiber techniques for next-generation optical access networks," *NOC 2011*, IT-5.

[81] M. Morant, T. Quinlan, S. Walker, and R. Llorente, "Real world FTTH optical-to-radio interface performance for bi-directional multi-format OFDM wireless signal transmission," *OFC/NFOEC 2011*, NTuB6.

[82] M. Sauer, A. Kobyakov, and J. George, "Radio Over Fiber for Picocellular Network Architectures, " *J. Lightw. Technol*., vol. 25, no. 11, pp. 3301-3320, Nov. 2007.

[83] Y.-T. Hsueh, Z. Jia, H.-C. Chien, A. Chowdhury, J. Yu, and G.-K. Chang, "Generation and transport of independent 2.4 GHz (Wi-Fi), 5.8 GHz (WiMAX), and 60-GHz optical millimeter-wave signals on a single wavelength for converged wireless over fiber access networks," *OFC/NFOEC 2009*, OTuJ1.

[84] Y.-T. Hsueh, M.-F. Huang, S.-H. Fan and G.-K. Chang, "A novel lightwave centralized bidirectional hybrid access network: seamless integration of RoF with WDM-OFDM-PON," *IEEE Photon. Technol. Lett*., vol. 23, no. 15, pp. 1085-1087, Aug 2011.

[85] D. Qian, N. Cvijetic, J. Hu, and T. Wang, "108 Gb/s OFDMA-PON with polarization multiplexing and direct detection," *J. Lightw. Technol.*, vol. 28, no. 4, pp. 484-493, Feb. 2010.

[86] IEEE Standard 802.16e-2005, "IEEE standard for local and metropolitan area networks; part 16: air interface for fixed broadband wireless access systems, amendment 2: physical and MAC layers for combined fixed and mobile operation in licensed bands and corrigendum 1," Feb. 2006.

[87] A. Chowdhury, H.-C. Chien, S.-H. Fan, J. Yu, and G.-K. Chang, "Multi-band transport technologies for in-building host-neutral wireless over fiber access systems," *J. Lightw. Technol*., vol. 28, no. 16, pp. 2406-2415, Aug. 2010.

[88] G. Raybon and P. Winzer, "Optical transport of 100G Ethernet serial formats," *LEOS 2007*, TuEE3.

[89] P. J. Winzer, R.-J. Essiambre, "Advanced optical modulation formats," *in Proceedings of the IEEE*, vol. 94, no. 5, pp. 952-985, May 2006.

[90] P. Yue, A. Wen, T. Shang, and C. Wang, "Implementation of differential precoder for high-speed optical DQPSK modulation," *WOCN 2008*, pp. 1-3.

[91] SHF, "Application note DQPSK: bit error test solution," 2008.

[92] B. Koch et al., "Record 59-krad/s polarization tracking in 112-Gb/s 640-km PDM-RZ-DQPSK transmission," *IEEE Photon. Technol. Lett*., vol. 22, no. 19, pp. 1470-1472, Oct. 2010.

[93] C. R. S. Fludger et al., "Coherent equalization and POLMUX-RZ-DQPSK for robust 100-GE transmission," *J. Lightw. Technol.*, vol. 26, no. 1, pp. 64-72, Jan. 2008.

[94] M. G. Taylor, "Coherent detection method using DSP for demodulation of signal and subsequent equalization of propagation impairments," *IEEE Photon. Technol. Lett*., vol. 16, no. 2, pp. 674 –676, Feb. 2004.

[95] K. Kikuchi, "Polarization-demultiplexing algorithm in the digital coherent receiver," *IEEE/LEOS 2008*, MC2.2.

[96] A. J. Viterbi and A. M. Viterbi, "Nonlinear estimation of PSK-Modulated carrier phase with application to burst digital transmission," *IEEE Trans. Inf. Theory*, vol. IT-29, no. 4, Jul. 1983.

[97] J. M. Kahn and K.-P. Ho, "Spectral Efficiency Limits and Modulation/Detection Techniques for DWDM Systems," *IEEE J. Sel. Topics Quantum Electron*, vol. 10, no. 2, pp. 259-272, Mar. 2004.

[98] X. Xian et al., "XPM penalty mitigation for a 42.7-Gb/s DQPSK channel co-propagating with 10.7-Gb/s OOK channels using SSMF and dispersion map," *LEOS 2008*, WH4.

[99] P. J. Reyes, I. M.-Fernández, and J. Jiménez, "Performance of cost effective 100G transmission in transparent wide-area optical network," *ECOC* 2010, paper P5.03.

[100] K.-P. Ho, "Error probability of DPSK signals with cross-phase modulation induced nonlinear phase noise," *IEEE J. Sel. Topics Quantum Electron*, vol. 10, no. 2, pp. 259-272, Mar. 2004.

[101] A. G. Striegler and B. Schmauss, "Compensation of intrachannel effects in symmetric dispersion-managed transmission systems," *J. Lightw. Technol.*, vol. 22, no. 8, pp. 1877-1882, Aug. 2004.

[102] N. Kataoka et al., "Field trial of 640-Gbit/s-throughput, granularity-flexible optical network using packet-selective ROADM prototype," *J. Lightw. Technol*., vol. 27, no. 7, pp. 825-831, Apr., 2009.

[103] S. Gringeri, R. Egorov, B. Basch, and G. Wellbrock, "Real-Time 127-Gb/s Coherent PM-QPSK Transmission over 1000km NDSF with >10 Cascaded 50GHz ROADMs" *ECOC 2010,* P4.09.

[104] J. H. Chang, K. Y. Cho, H. Y. Choi, Y. Takushima, and Y. C. Chung, "Filtering tolerance of 108-Gb/s PolMux quadrature duobinary signal on 250GHz grid," *OFC/NFOEC 2011,* OMR4.

[105] Y.-H. Wang and I. Lyubomirsky, "Impact of DP-QPSK pulse shape in nonlinear 100G Transmission," *J. Lightw. Technol.,* vol. 28, no. 18, pp. 2750-2756, 2010.

[106] C. Xie, G. Raybon and S. Chandrasekhar, "Comparison of RZ and NRZ formats in 112-Gb/s PDM-QPSK long haul coherent transmission systems," *OFC/NFOEC, 2011,* JThA39.

[107] Y. Pointurier and M. Brandt-Pearce, "Analytical study of crosstalk propagation in all-optical networks using perturbation theory," *J. Lightw. Technol.,* vol. 23, no. 12, pp. 4074-4083, 2005.

[108] T. Zami et al., "Crosstalk analysis applied to wavelength selective switches," *OFC/NFOEC 2006,* OFP4.

[109] S. Yamamoto et al., "Influence of intrachannel crosstalk with frequency dependence on signal degradation in optical switch network," *J. Lightw. Technol.,* vol. 27, no. 24, pp. 5716-5722, Dec., 2009.

[110] H. Bissessur and C. Bastide, "Experimental assessment of frequency-dependent crosstalk penalty with different 43 Gb/s modulation formats," *ECOC 2007,* P083.

[111] J. C. Attard, J. Mitchell, and C. Rasmussen, "Performance analysis of interferometric noise due to unequally powered interferers in optical networks," *J. Lightw. Technol.,* vol. 23, no. 4, pp. 1692–1703, 2005.

[112] R. Meleiro, et al., "Impact of self-phase modulation on in-band crosstalk penalties," *IEEE Photon. Technol. Lett.,* vol. 20, no. 8, 2008.

[113] E. Ciaramella and F. Curti, "Experimental assessment of node crosstalk limitations enhanced by nonlinear effects in all optical transport networks," *IEEE Photon. Techno*l. *Lett.,* vol. 11, no. 6, pp. 751-753, 1999.

[114] F. Heismann, "System requirements for WSS filter shape in cascaded ROADM networks," *OFC/NFOEC 2010,* OThR1.

[115] P. J. Winzer, M. Pfennigbauer, M. M. Strasser, and W. R. Leeb, "Optimum filter bandwidths for optically preamplified NRZ receivers," *J. Lightw. Technol.,* vol. 19, no. 9, pp.1263-1273, Sept. 2001.

[116] P. J. Winzer and A. Kalmar, "Sensitivity enhancement of optical receivers by impulsive coding," *J. Lightw. Technol.,* vol. 17, no. 2, pp.171–177, Feb. 1999.

[117] A. Stark et al., “Scaling 100G QPSK links for reliable network development,” *SPIE 2011,* 7959-11.

[118] Y.-T. Hsueh et al., “Analysis of in-band crosstalk transmission penalties on 112 Gb/s PDM-QPSK in linear optical links,” *IEEE Photon. Technol. Lett.,* vol. 23, no. 11, pp. 745-747, June 2011.

[119] Y.-T. Hsueh et al., “Nonlinearity impact on crosstalk effects for a 112 Gb/s PDM-QPSK system,” *OFC/NFOEC 2012*, NTu1F.4.

[120] B. Xu and M. Brandt-Pearce, “Analysis of noise amplification by a CW pump signal due to fiber nonlinearity,” *IEEE Photon. Technol.* Lett., vol. 16, no. 4, pp. 1062–1064, Apr. 2004.

[121] A. Bononi, N. Rossi, and P. Serena, "Transmission limitations due to fiber nonlinearity," *OFC/NFOEC 2011*, OWO7.

[122] A. Carena, V. Curri, R. Gaudino, P. Poggiolini, and S. Benedetto, “New analytical results on fiber parametric gain and its effects on ASE noise,” *IEEE Photon. Technol. Lett*., vol. 9, pp. 535–537, Apr. 1997.

[123] P. J. Winzer, A.H. Gnauck, A. Konczykowska, F. Jorge, and J.-Y. Dupuy, “Penalties from in-band crosstalk for advanced optical modulation formats” *ECOC 2011,* Tu.5.B.7.

[124] Z. Wang, Y.-K. Huang, E. Ip, P. R. Prucnal, and T. Wang, “Performance investigation of polarization-multiplexed 16-QAM using all-optical OFDM transmission and digital coherent detection,” *OFC/NFOEC 2011*, OMS5.

VITA

YU-TING HSUEH

Hsueh was born in Taichung City, Taiwan, in 1981. She received the B.S. degree in Electrical Engineering from National Tsing Hua University, Hsinchu, Taiwan, in 2003 and the M.S. degree in Electro-Optical Engineering from National Chiao Tung University, Hsinchu, Taiwan, in 2005. In August 2007, Hsueh joined the Optical Networking Research Group in the School of Electrical and Computer Engineering, Georgia Institute of Technology, where she has conducted research toward Ph.D. degree in the field of long-haul wired and last mile, last meter wireless access communications over optical systems for high-data-rate applications.

She has authored and co-authored more than 40 peer-reviewed journal papers and international conference proceedings, and regularly serves as a reviewer for several journals, including the *Journal of Optical Communications and Networking*, *Optics Express*, and *IEEE/OSA Journal of Lightwave Technology*. She is one of the recipients of the 2010 PSC Bor-Uei Chen Memorial Scholarship and IEEE Photonics Society 2011 Graduate Student Fellowship.